WARWICK
THE UNIVERSITY OF WARWICK

A Thesis Submitted for the Degree of PhD at the University of Warwick

Permanent WRAP URL:
http://wrap.warwick.ac.uk/128731

Copyright and reuse:
This thesis is made available online and is protected by original copyright.
Please scroll down to view the document itself.
Please refer to the repository record for this item for information to help you to cite it.
Our policy information is available from the repository home page.

For more information, please contact the WRAP Team at: wrap@warwick.ac.uk

warwick.ac.uk/lib-publications

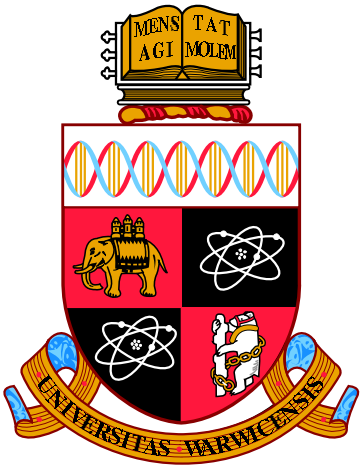

Eddy Current Array Optimisation

by

Abbas Akinola Akanni Egbeyemi

Thesis

Submitted to the University of Warwick

for the degree of

Doctor of Engineering

Department of Physics

September 2018

THE UNIVERSITY OF WARWICK

Contents

Acknowledgments

This thesis is dedicated to my family; Muyibat, Saheed, and Toyyibat Egbeyemi. Without their unwavering support, none of this would have been possible. I would also like to thank Steve Dixon, who has not only been an amazing supervisor, but a partner, and a friend.

From EtherNDE: I am grateful to John Hansen, for the funding, his contributions to the work in this thesis, and for providing the EtherNDE technology used in the experiments. Ian Drew, for replying my late night google messages when I was trying to figure out C# programming, and Alan Daly, for his help with understanding the electronics in the EtherNDE machines.

From the University of Warwick: Rachel Edwards, for the thorough, and brutally honest feedback on reports. Mareike Herrmann, for laser micro-machining the defects on all my samples. The electronics guys - Bob day, Tung "Nixon" Yu, and David Greenshields, for dealing with me, and my burned multiplexers. Jonathan Harrington for all the 'elbow grease' put into grinding the very hard titanium aluminide sample, and very special thanks to Yichao "Charley" Fan, for his tremendous help at the start of this project.

It takes a community to raise a child, and I am grateful to everyone in the ultrasonics group for being an amazing community. I am a better person than when I started.

Declarations

I, Abbas Egbeyemi, do declare that the work presented in this thesis is my original research. Every effort is made to clearly indicate where contributions from others were involved, with due reference to literature, and acknowledgement of collaborative research and discussions. This work was performed under the guidance of Prof. Steve Dixon from the Department of Physics, at the University of Warwick, and John Hansen from EtherNDE, during the period between October 2014, and September 2018.

No part of this work has been previously submitted to the University of Warwick, or any other academic institution for the admission to a higher degree.

Some of the work has been presented at various conferences as listed below, and may appear in the form of a publication, and that is also listed below,

Conferences presented

Review of Progress in Quantitative Nondestructive Evaluation (QNDE 2017)
Annual British Conference of Non-Destructive Testing (NDT 2017)

Submitted Paper

A. Egbeyemi, J. Hansen, and S.Dixon, *Improving the SNR of Eddy Current C-scans*, NDT & E International.

Abstract

There is a drive in industry to reliably detect surface breaking sub-millimetre defects in low electrical conductivity materials, such as stainless steel, titanium, and titanium aluminide using eddy-current testing. The sensitivity of the eddy current method to these materials is hindered in part by their low conductivities, and complex grain structures, which makes the high sensitivity standards required by industry more difficult to achieve.

Eddy current measurements for sub-millimetre defects in low conductivity materials are routinely performed using a high excitation frequency, to decrease the skin depth of induced eddy currents into the material, which would otherwise be higher due to the reciprocal relationship between depth of penetration, and material conductivity.

The fundamental components of an eddy current array is a pair of coils, and thus finite element models are presented in this thesis, and are used to investigate the interaction between low conductivity materials, and a pair of eddy current coils operating in absolute, and transmit-receive modes. The model results give insight to the eddy current coil voltage response to defects, and the relationship between absolute mode, and transmit-receive mode data when taken concurrently.

Experiments are performed, which show how the combination of a voltage amplitude C-scan image with its corresponding voltage phase C-scan image, results in an image with a significantly improved signal to noise ratio. In the same experiments, absolute mode data is also combined with transmit-receive mode data to generate a single image with signal to noise ratio values significantly higher than anything achievable using individual images. Varying levels of noise are added to the data to investigate the limits at which this data processing method can be utilised.

Low conductivity materials such as titanium aluminide, containing defects as small as 0.25 mm were scanned, and promising results were achieved showing that defects this small can be reliably detected using the inspection method, and data processing techniques presented in this thesis.

List of Figures

List of Tables

Abbreviations

NDT - Non-destructive Testing

EC - Eddy-Current

ECA - Eddy-Current Array

PEC - Pulsed Eddy-Current

UT - Ultrasonic Testing

PoD - Probability of Detection

FE - Finite Element

AC - Alternating Current

DC - Direct Current

Nomenclature

$\mathbf{A}$	Magnetic vector potential	Vsm^{-1}
$\mathbf{B} = \nabla \times \mathbf{A} = \mu\mathbf{H}$	Magnetic flux density	T
$\mathbf{D} = \varepsilon\mathbf{E}$	Electric displacement field	Cm^{-1}
$\mathbf{E}$	Electric field	Vm^{-1}
$\mathbf{H}$	Magnetic field	Am^{-1}
$\mathbf{J} = \sigma\mathbf{E}$	Current density	Am^{-2}
$\mu = \mu_0\mu_r$	Permeability	Hm^{-1}
μ_0	Permeability of free space	Hm^{-1}
μ_r	Relative permeability	
$\omega = 2\pi f$	Angular frequency	$\mathrm{rad} \cdot \mathrm{s}^{-1}$
$\rho = 1/\sigma$	Resistivity	$\Omega\mathrm{m}$
σ	Conductivity	Sm^{-1}
$\varepsilon = \varepsilon_0\varepsilon_r$	Permittivity	Fm^{-1}
ε_0	Permittivity of free space	Fm^{-1}
ε_r	Relative permittivity	
C	Capacitance	F
f	Frequency	Hz
$i = \sqrt{-1}$	Complex number	
L	Inductance	H

R	Resistance	Ω
t	Time	s
$X = \Im\{Z\}$	Reactance	Ω
$Z = R + jX$	Impedance	Ω

Chapter 1

Introduction

1.1 Motivation

Critical jet engine components made from high strength metals are routinely subjected to intense forces, and extreme temperatures. These components, while designed with strict tolerances to have long service life cycles[1], have to be monitored, as even small discontinuities could result in disastrous consequences[2, 3, 4, 5]. It is therefore imperative that flaws in these components are detected before they propagate. Engineers, and researchers are charged with the task of developing reliable, and understandable methods of testing for discontinuities in these components without compromising their utilities, or function. These methods are the science of non-destructive testing (NDT).

There are various NDT techniques, which have benefits, and drawbacks depending on the inspection requirements. Some methods are more suitable to the inspection of surface defects (visual inspection, magnetic particle inspection and, eddy current testing), while some analyse the entire bulk of the component (ultrasonic testing and radiography). Material properties, the size, location, and geometry of the defect to be tested, are just some of the factors which determine the most applicable technique for a given inspection. Limiting factors in selecting a technique include cost, accessibility to the required tools, and component geometry limitations such as complex shapes, and sizes[6].

Eddy current testing (ECT) is most applicable to the detection of surface and near surface defects in electrically conductive materials. The inspection of safety critical components is of paramount importance, meaning that techniques determining the presence, or absence of a defect have to meet certain sensitivity thresholds for the results to be deemed valid. The advancement of industrial manu-

facturing processes, which enable the manufacturing of single part components with complex shapes, defect growth prevention measures (coatings and shot-peening), and complex micro-structures of new materials, are some of the factors, which make it more difficult to reach these sensitivity thresholds with conventional ECT measurements[7, 8, 9, 10]. Therefore, more advanced inspection, and data processing techniques have to be devised to meet the sensitivity thresholds required by industry. Furthermore, the increased inclusion of NDT inspection as part of mass manufacturing means that high sensitivity thresholds have to be used when the process is automated. Eddy current array probes, which consist of multiple ECT sensors working concurrently have become increasingly popular, as they provide more surface coverage, thereby decreasing inspection time.

The aims of this EngD research are as follows:

- Understand the design, and modes of operation of typical ECT probes in order to design a multiplexed eddy current array system.
- Investigate the interaction between eddy current coils and electrically conductive materials, and the behaviour of eddy currents induced in a sample using finite element modelling.
- Investigate data processing techniques for the improvement of defect signal to noise ratio, using magnitude and phase data, from coils driven in both absolute, and transmit-receive modes.
- Design a system for the inspection of low conductivity materials at sub MHz excitation frequencies.
- Investigate the utility of using sub MHz excitation frequencies to test for sub mm defects in stainless steel, titatium, and titanium aluminide.

1.2 Review of NDT Techniques

There are various types of NDT techniques, each with their advantages and disadvantages, depending on the kind of measurement desired. Many of these techniques have strengths that complement one another, thus in most cases, multiple techniques are applied to the inspection of a component to get a comprehensive evaluation. This section provides a brief overview of some NDT techniques, their advantages, and disadvantages.

1.2.1 Visual Inspection

Visual inspection is the oldest form of non-destructive evaluation, and is simply using the unaided eye to inspect components for visual signs of defect symptoms or abnormalities[11]. As the least expensive technique, it is commonly used everyday in a myriad of applications ranging from the inspection of textile before sale, to the examination of nuclear reactors (using live video feeds). The inherently subjective nature of visual inspection makes it difficult to define numerical sensitivity thresholds, however NDT technicians qualified to perform visual inspection have to undergo extensive training, and testing to ensure that the inspection is performed to a reliable standard[11, 12]. Therefore, visual inspection is often used as a starting point to identify areas where degradation or discontinuities have occurred, after which other NDT methods can be used to confirm, and characterise the flaw.

One of the drawbacks of visual inspection is the ease of access to the component surface. Many other techniques to aid in the use of the visual inspection method include lenses, mirrors, microscopes, and (like for nuclear reactors) live video cameras[1]. More resent research has led to the development of shearography (or shearing interferometry). This technique involves the use of a point source of coherent light (such as a laser) incident on the surface to be inspected. The surface is photographed with a camera, which has a wedge shaped prism fitted onto its lens, enabling it to produce a pair of laterally sheared images of the surface. These images interfere with each other, producing a random interference pattern referred to as the speckle pattern, which changes with the presence of defects[13, 14].

The main disadvantages of visual inspection however, are that it is only applicable to the inspection for surface damage, and in many cases the surface has to be prepared beforehand (by cleaning or stripping coatings). It is also only reliable for the detection of large area damage, and not small hairline cracks.

Penetrant Testing

Penetrant testing is an extension of visual inspection, which involves the use of a brightly coloured (sometimes fluorescent) liquid dye with low surface tension, applied to aid in the visibility of surface breaking defects. The liquid is allowed to penetrate into the crack via capillary action, and excess liquid is wiped off, after which, a developer is applied to draw out the penetrated liquid to form the shape of the defect (see fig. 1.1(a)). The sample surface is then inspected under appropriate lighting such as UV light for fluorescent dye, to evaluate the size, and location of the defect[11].

Penetrant testing is effective for the detection of small surface defects, and is independent of material properties or geometry. However, its main limitation is that it requires extensive preparation of the surface to be inspected. This involves stripping off any paint or coatings, and thoroughly cleaning the surface before inspection, which will prolong the amount of time the component is out of service. It is also inefficient at the detection of very small cracks, and tightly closed or partially closed cracks, which might make the sizing of defects inaccurate. The storage, preservation, and careful application of the penetrant also highly influences the reliability of the method[1].

Magnetic Particle Inspection of Ferromagnetic Samples

A tangential magnetic field applied to the surface region of a ferromagnetic component will normally lie within the material. If the sample has a crack, a portion of the field leaves the surface through the crack, and magnetic particles will be attracted to the area of the surface where the field is 'leaking'. Magnetic particle inspection involves the use of 'magnetic ink', which consists of a liquid carrier containing many minute magnetic particles, applied onto a surface on which, the tangential field is incident (see fig. 1.1(b)). The particles within this ink will be preferentially attracted to any areas on the surface where a crack is present[1]. Similar to magnetic particle inspection is the magnetic flux leakage method. The same principle of a leaking magnetic field applies, however the leaking flux is detected using a magnetic field sensor such as an inductive coil, or hall effect sensor.

An advantage of this technique is that the magnetic field is also affected by sub surface defects, although the magnitude of the leaking field decreases rapidly if the defect does not break the surface. This technique is limited by its application to only ferromagnetic, or magnetically permeable materials, and is only sensitive to defects oriented perpendicular to the direction of the incident tangential field[11, 15]

1.2.2 Radiography

Radiography is one of the most widely used NDT techniques. It is an effective method, involving the generation of an image, which is a two dimensional intensity distribution of radiation (X-ray or gamma-ray), that has penetrated the component being tested. Defects present in the component will partially pass more or less of the incident radiation through. A crack for instance, will attenuate less of the radiation than the rest of the component, and thus will appear as a relatively darker region in the radiation pattern, which can be made visible using media such as photographic

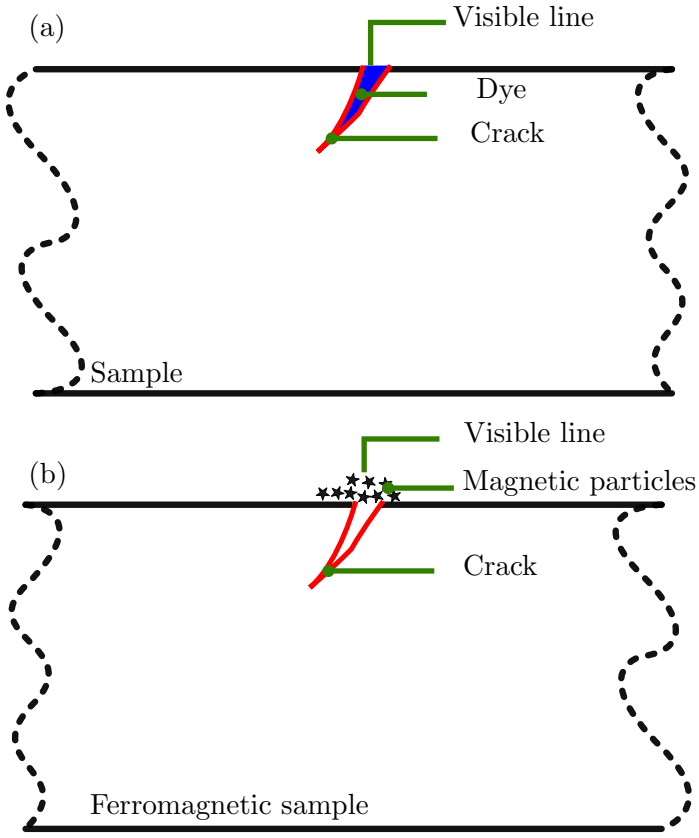

Figure 1.1: Techniques that aid with visual inspection. (a) Penetrant testing; a liquid dye penetrant is applied to the sample, which penetrates surface breaking defects and enables visualisation, and sizing of the defect. (b) Magnetic particle inspection; a magnetic field is applied tangential to the surface of a ferromagnetic sample, and will 'leak' through any cracks on the surface. A 'magnetic ink', consisting of a liquid carrier, containing magnetic particles is applied, and the magnetic particles are attracted to the part of the surface where the magnetic field is leaking. After [1].

film, fluorescent screens, or electronic detectors. Radiographic images are often produced in multiple orientations to get a complete profile of the sample, and the contrast in the images enable the operator to accurately locate, and characterise any defects present[1, 16].

Radiography provides a visual image of flaws in the component, and due to its sheer penetration power, materials of varying thickness levels can be tested. Complex shaped components, which would otherwise be difficult to test using other methods are more easily tested using radiography. It is also applicable to components made from various types of metallic, and non-metallic materials[11].

For all its merits, there are also some limitations to radiography. While it is effective at detecting discontinuities at any part of the component, the discontinuity must be oriented parallel to the beam direction. The radiation is also a considerable health risk, and is most often performed in controlled environments, where the safety of the operator or technician is assured. Thus, the performance of *in situ* inspections are limited by safety regulations, hence radiographic inspections can be carried out *in-situ*, however significant precautions have to be taken.

1.2.3 Ultrasonic Testing (UT)

The UT method is a very flexible, and robust technique that is applicable in a wide range of industries. It can be performed *in situ*, and is capable of detecting discontinuities either on the surface, or deep within the bulk of the component[17]. Fundamentally, UT inspections are conducted by introducing electrically controlled pulses into a material using a transducer. The ultrasonic waves generated will propagate through the material, and reflect off discontinuities, and the outer boundaries of the component. These echoes provide information on the presence of defects and their size (with complex data processing)[18]. UT is one of the few methods which can reveal substantial internal flaws in materials. The most common methods of generating and detecting ultrasound in materials include piezoelectric transducers, Electomagnetic Acoustic Transducers(EMAT), and laser-based ultrasonics[19, 20, 21, 22].

The most common type of transducer is the piezoelectric transducer which utilises piezoelectric plates that deform when electric fields are applied to them, producing elastic waves[21]. These waves are transferred to the specimen with the aid of a coupling fluid, which may be a an immersion bath, or a thin film between the transducer, and the specimen. Piezoelectric plates also produce electric fields when they vibrate, and thus they can be used for both transmission, and reception of ultrasound[1]. This technique is often limited in utility by its need for direct contact between the transducer and test specimen, and thus is unsuitable in hostile

environments (such as elevated temperatures), or where the specimen has coatings which are attenuative to ultrasound[21, 22]. UT inspections can however be conducted without direct contact between the probe and test specimen, an example of which, is when the specimen is immersed in a fluid, that is less attenuative to the ultrasonic waves than air. The immersion fluid serves as a good coupling mechanism between the test specimen and transducer, thus contact between the transducer and test specimen is unnecessary.

EMATs are non contact ultrasonic transducers that generate ultrasounds in electrically conducting materials using electromagnetic induction, and the Lorentz force mechanism. The non-essentiality of contact between the transducer and specimen make EMATs suitable for high speed, and repeatable inspections in hostile environments, and through coatings[22]. Their application is however limited by their low signal to noise levels, which is due to the decreased electromagnetic coupling between the transducer and specimen as lift-off increases. Thus while considered non-contact transducers, EMATs have to be within a few millimetres of the test specimen to be useful[11].

Laser-based UT generates ultrasound using high energy pulsed optical beams ($\lambda \approx 1\mu$m) focused onto the surface of the test component[23]. The ultrasound is generated in one of two distinct processes, with unique acoustic wave patterns within the material; ablative, and thermoelastic. These processes are primarily dependent on the energy density of the pulsed optical beam, and the energy absorption ability of the material. In the ablative process, a higher energy pulse is focused on a highly absorptive material, ablating the surface as a local explosion, which generates the ultrasonic pulse. The thermoeleastic process results from a lower energy pulse, focused on a low-absorbing material which rapidly heats the surface causing thermal expansion, and is followed by rapid cooling as the energy disperses. This cyclic thermal expansion, and relaxation generates the ultrasonic wave. Laser generated waves can be detected using EMATs or piezoelectric transducers, but more often, optical methods are used such as laser interferometry[23]. Scruby and Drain[24], and Monchalin [25] have publications with more details on the generation, and detection mechanisms of laser-based UT, and a review of industrial applications.

Laser-based UT is a high resolution technique, which is able to operate at large lift-off distances ($>$ 1m). This makes it sometimes the only UT solution applicable in certain circumstances. However, it is limited by low sensitivity, and the potential to damage the material surface. It also carries certain safety considerations due to the high energy optical beams, and is very costly[11].

1.2.4 Eddy Current Testing (ECT)

ECT is a non-contact inspection technique, characterised by its repeatability, and high sensitivity to surface defects in electrically conductive materials. It is also able to detect near surface defects, and is unimpeded by thin material coatings. ECT is not subject to the various surface contact considerations applicable to piezoelectric UT. It is however limited by high sensitivity to lift-off, probe tilt, and can be insensitive to tightly closed, or conductive cracks; a common issue with UT, radiography, penetrant inspections, and most other NDT methods.

The basic operation of ECT involves the use of an inductive coil carrying an alternating current. The current through the coil will generate a time varying magnetic field, which can induce eddy currents in the surface of an electrically conductive material within proximity. The mutual interaction between the coil magnetic field, and induced eddy currents can be measured by measuring the change in electrical impedance of the coil. The eddy currents are induced directly below the coil, and flow in a trajectory determined by the coil shape and lift-off. The presence of a discontinuity will impede the flow of eddy currents, and will be reflected in the impedance of the generating coil, and any other detection coils or magnetic field sensors[26, 27].

ECT only detects surface or near surface discontinuities, so that locating a defect is a matter of considering the location of the sensor with respect to the defect signal, unlike UT, which requires extensive analysis of complex time traces in order to locate the defects detected[18]. ECT can be used for the inspection of ferromagnetic materials, however the large magnetic permeability of these materials make them difficult to inspect. This is due to a large magnetic flux present in the specimen, resulting from the large magnetic permeability. Thus an excitation coil brought close to the ferromagnetic test piece will experience a large increase in coil inductance, which may overshadow the expected decrease in coil inductance caused by the induced eddy currents. To inspect ferromagnetic materials, the sample is either demagnetized before inspection, or immersed in a constant saturating magnetic field, superimposed onto the magnetic field from the excitation coil. Under such conditions, the material behaves like it is non ferromagnetic[23].

Although ECT is considered a non-contact inspection technique, the sensitivity of an EC sensor to a test sample is affected by the distance between the sensor, and the surface of the test sample. This is referred to as the lift-off effect, where the inductive coupling between the sensor and test sample varies with the distance between them. These variations can be caused by varying thickness of the sample coating, tilting of the probe, an irregular sample surface, or even the movement of

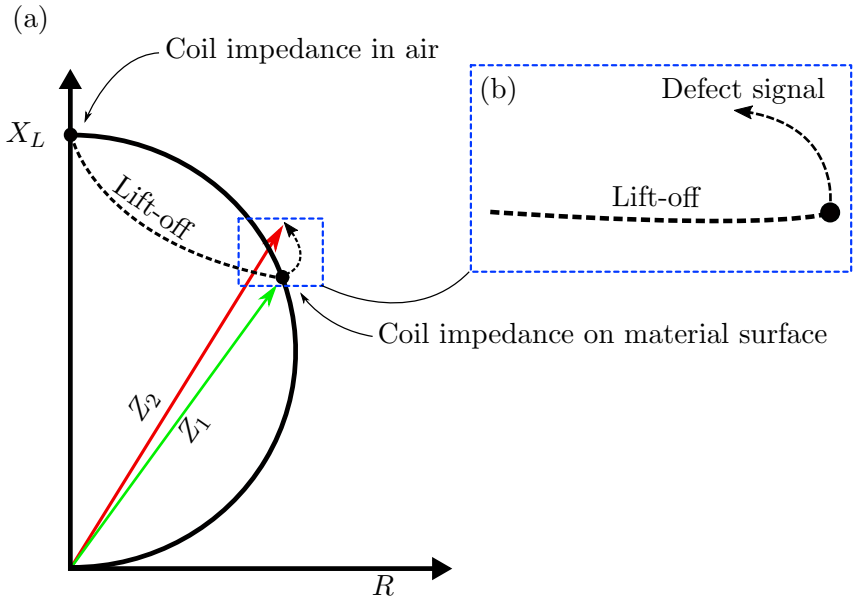

Figure 1.2: (a) Simplified impedance plane diagram showing the impedance of an EC probe when in air, in close proximity to a material, and in the presence of a defect. (b) Inset shows the difference in trajectory between the lift-off signal, and a defect signal as presented in typical EC instruments. After [23].

the operator[28, 29, 30]. Probe lift-off and tilt noise affect the apparent impedance of the EC coil, and can sometimes mask the defect indications as shown in chapter 4. Care is often taken to minimise these effects during inspection, by ensuring the sensor is encased in a structure, which closely matches the shape of the part being inspected, or by using a weighted or spring loaded probe holder to minimise lift-off variations as the probe scans along the sample surface.

In typical EC inspections, the data is presented in the form of an impedance plane diagram. An ideal coil away from an electrically conductive sample, will have an entirely reactive impedance. As the coil is brought closer to the test sample, the inductive coupling between coil, and sample increases, causing the reactive component of the coil impedance to decrease, and the resistive component to increase in the trajectory indicated by the lift-off curve in fig. 1.2. An undamaged sample will ideally cause the coil to have a constant impedance of Z_1, however, the presence of a defect will change the coil impedance to Z_2 in a trajectory such as that represented by the defect signal curve in fig. 1.2(b). EC instruments enable the representation of the data with the lift-off curve rotated to be horizontal, so that any defect indication is easily distinguished, however prove tilt, or lift-off variations will impact the lift-off curve, sometimes making a defect indication indistinguishable from lift-off.

Experiments presented in this thesis present the EC data in the form of

images generated using multiple coil inductance measurements from a probe scan of the test piece surface. The effects of lift-off noise in the experiments, which are due to an uneven test piece surface, are shown in chapter 6, where in some cases defect indications are almost entirely masked by the lift-off variations.

Single element probe scans can be very time consuming due to the localised nature of eddy currents, and thus will require a scan of the specimen surface to get full coverage. With eddy current arrays, this inspection time is significantly reduced, as they contain multiple sensors, which provide wider coverage[31].

Eddy currents are limited to electrically conductive materials, and are highly sensitive to surface, and near surface small defects. The depth of detectable defects is related to the skin depth, which is dependent on material properties such as conductivity, permeability, and on the frequency of current excitation.

1.3 Summary

This chapter presents a brief introduction to NDT, and the aims and motivations of the research conducted in this EngD. The most common methods of NDT were discussed, as are some of their advantages, and disadvantages. ECT methods are often relied upon for the surface inspection of critical components made from electrically conductive materials in industry, however the adoption of more advanced ECT methods has been slow in the past decade. The high sensitivity requirements of industry are slowly becoming unattainable for conventional ECT methods, and therefore the time for the adoption of demonstrably more sensitive advanced techniques is now. The following chapter presents a more comprehensive discussion of the fundamental principles behind eddy current testing.

Chapter 3 presents a review of common ECT techniques. Considerations such as probe design, excitation, and instrumentation are discussed. In chapter 4, experiments conducted using an eddy current probe containing a pair of coils to inspect stainless steel, and titanium samples containing surface breaking defects as small as 0.25 mm long are presented, and discussed. A novel data processing method for improving the signal to noise ratio of these very small defect indications is demonstrated. Finite element models, which help explain the electromagnetic interaction between EC coils, and electrically conductive materials are presented, and discussed in chapter 5. The models produce results, similar to the experiments, and serve to guide the refinement of the EC probe designs, and to validate the experimental data. Chapter 6 presents experiments conducted using a relatively low frequency (300 kHz) to detect sub-millimetre defects in low conductivity materi-

als, a substantial improvement on the conventional eddy current testing method. Conclusions, and suggestions for future work are presented in chapter 7.

Chapter 2

Eddy Current Theory

This chapter presents some of the fundamental theories and equations governing the operation of eddy current (EC) test probes. EC probes are generally coils of wire, which are driven by alternating currents, that generate changing magnetic fields, which induce currents in electrically conducting materials. These induced currents referred to as eddy currents will influence the characteristic electrical properties of the coil, in relation to the material in which they are induced[32]. Measuring the change in the coil electrical properties provides insight to the material properties, such as its conductivity, and the presence of discontinuities[23].

2.1 Electromagnetic Induction

Eddy current measurements are fundamentally based on the principles of electromagnetic induction. Maxwell's equations describe the laws governing these principles.

$$\nabla \cdot \mathbf{E} = \frac{\rho}{\varepsilon_0}, \tag{2.1}$$

$$\nabla \cdot \mathbf{H} = 0, \tag{2.2}$$

$$\nabla \times \mathbf{E} = -\mu \frac{\partial \mathbf{H}}{\partial t}, \tag{2.3}$$

$$\nabla \times \mathbf{H} = \mathbf{J} + \varepsilon_\mathbf{0} \frac{\partial \mathbf{E}}{\partial \mathbf{t}}, \tag{2.4}$$

where, $\mathbf{H}$, and $\mathbf{E}$ are the magnetic and electric fields respectively. ρ is the charge density, ε_0 the permittivity of free space, and μ, the permeability of free space. Equation (2.1) is Gauss's law for electric fields, and it states that the divergence of

an electric field is proportional to the density of charges at the location at which the divergent field is present. This means that in space, a divergent electric field only occurs where a positive charge is present, and a convergent electric field, where a negative charge is present. Equation (2.2) is Gauss's law for magnetic fields, and it states that the divergence of a magnetic field is always zero at any point.

Faraday's experiments showed that a changing magnetic flux, induced a voltage in a loop of wire. This voltage, referred to as electromotive force (emf) is defined as[33]:

$$V_{emf} = -\frac{d\phi}{dt}, \tag{2.5}$$

where ϕ is the magnetic flux through the loop. In the case where there are multiple loops, the induced voltage becomes:

$$V_{emf} = -N\frac{d\phi}{dt}, \tag{2.6}$$

N is the number of loops. The emf is a closed contour integral of the non-conservative electric field intensity in the wire, given by:

$$V_{emf} = \oint_C \mathbf{E} \cdot d\mathbf{l}. \tag{2.7}$$

The magnetic flux, ϕ from eq. (2.5) can be calculated from the magnetic flux density by:

$$\phi = \int_s \mathbf{B} \cdot d\mathbf{s}, \tag{2.8}$$

Substituting the expressions for V_{emf}, and ϕ from eqs. (2.7) and (2.8) into eq. (2.5) gives:

$$\oint_C \mathbf{E} \cdot d\mathbf{l} = -\frac{d}{dt}\int_s \mathbf{B} \cdot d\mathbf{s}. \tag{2.9}$$

This is the integral statement of Faraday's law, which relates a time varying magnetic flux with the resultant induced electric field.

Stokes theorem relates a line integral around a closed path of a vector field, $\mathbf{F}$, to the surface integral of $\nabla \times \mathbf{F}$, over the surface defined by that path. Mathematically[34],

$$\int_s \nabla \times \mathbf{F} \cdot d\mathbf{s} = \oint_C \mathbf{F} \cdot d\mathbf{l}. \tag{2.10}$$

Applying stokes theorem to eq. (2.9),

$$\int_s (\nabla \times \mathbf{E}) \cdot d\mathbf{s} = -\frac{d}{dt} \int_s \mathbf{B} \cdot d\mathbf{s}, \tag{2.11}$$

the time independence of the integral on the right hand side means the differentiation can be performed within the integral, and made partial as the flux density might also be a function of space.

$$\int_s (\nabla \times \mathbf{E}) \cdot d\mathbf{s} = -\int_s \frac{\partial \mathbf{B}}{\partial t} \cdot d\mathbf{s}, \tag{2.12}$$

hence, for a loop of wire with a constant surface, the integrands must be equal:

$$\nabla \times \mathbf{E} = -\frac{\partial \mathbf{B}}{\partial t}. \tag{2.13}$$

This is the differential statement of Faraday's law, and Maxwell's third equation, eq. (2.3) and it shows the relation between a time varying magnetic flux and the resultant electric field. The negative sign on the right side of eq. (2.13) indicates that the changing magnetic flux results in an induced emf, which has a current that flows in a direction generating a flux opposing the original magnetic flux. This phenomenon is referred to as Lenz's law. The constitutive relationship between magnetic flux density and magnetic field is defined as:

$$\mathbf{B} = \mu H \tag{2.14}$$

where μ is the permeability.

2.1.1 Self-Inductance

In a situation where the magnetic flux through a coil is as a result of the current in the coil, any change in that current will induce an emf in the coil. Ampeère's Law states that the circulation of a magnetic field around a closed path is equal to the current enclosed by the path. Expressed mathematically as,

$$\oint_C \mathbf{H} \cdot d\mathbf{l} = I_{enc}, \tag{2.15}$$

where, **H** is the magnetic field, and I_{enc} is the enclosed current. The magnetic flux density, **B** is a product of the magnetic field, **B**, and the permeability of free space, μ, as stated in eq. (2.14).
A solenoid coil with a length, l, N number of turns per unit length, and a current, I flowing through it has a magnetic flux at all points within it approximated using Ampeère's law as,

$$B = \mu N I. \tag{2.16}$$

The magnetic field through each turn of the coil is $\mu N I \cdot \pi r^2$, where r is the radius of the coil, so that the total flux through the solenoid is,

$$\phi = \mu N I \cdot \pi r^2 \cdot N l. \tag{2.17}$$

Any change in the current within the solenoid will lead to an induced emf, V_{emf} which will oppose the current as defined by eq. (2.5).

$$\begin{aligned} V_{emf} &= -\frac{d\phi}{dt}, & (2.18)\\ &= -\mu N^2 \pi r^2 l \frac{dI}{dt}, & (2.19)\\ &= -L\frac{dI}{dt}, & (2.20) \end{aligned}$$

where,

$$L = \mu N^2 \pi r^2 l. \tag{2.21}$$

L is referred to the self inductance of the coil in air, and is only dependent on the geometric properties of the coil.

2.1.2 Mutual Inductance

A pair of solenoid coils wound on top of each other are illustrated in fig. 2.1. The coils have N number of turns, lengths, l, and a shared radius, r. The primary coil carrying a current I_1 will generate a field, B_1 and a magnetic flux, ϕ_2 through the secondary coil. Any change in I_1 will result in a change in the flux ϕ_2 according to eq. (2.17), inducing an emf, V_2 according to eq. (2.5).

$$V_2 = -\frac{d\phi_2}{dt}. \tag{2.22}$$

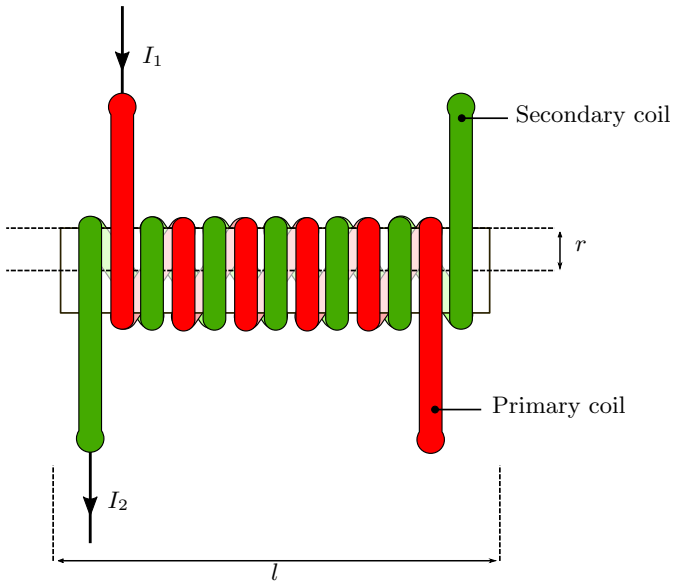

Figure 2.1: Illustration of a pair of coils wound on top of each other to demonstrate mutual inductance. A current of I_1 is flowing through the primary coil, and I_2 through the secondary coil. The coils have N number of turns, a shared radius, r, and lengths l. After [34].

.

If the inductance on the secondary coil as a result of the changing current in the primary coil is referred to as M_{12}, then the induced emf can be defined as,

$$V_2 = -M_{12}\frac{dI_1}{dt}, \tag{2.23}$$

where,

$$M_{12} = \mu N_1 N_2 \pi r^2 l. \tag{2.24}$$

With the roles reversed, the induced emf on the primary coil as a result of the secondary coil is defined as,

$$V_1 = -M_{21}\frac{dI_2}{dt}, \tag{2.25}$$

where,

$$M_{21} = \mu N_1 N_2 \pi r^2 l. \tag{2.26}$$

The terms M_{12}, and M_{21} have the same value and are referred to as, M, the mutual inductance of the coils, and is dependent on the coil construction and geometry. From eq. (2.21), the self inductance in each coil is,

$$L_1 = \mu N_1^2 \pi r^2 l, \tag{2.27}$$

$$L_2 = \mu N_2^2 \pi r^2 l, \tag{2.28}$$

hence, mutual inductance, M is defined as,

$$M = \sqrt{L_1 L_2}. \tag{2.29}$$

This definition makes the assumption that the entire magnetic flux from one coil passes through the other coil. In the real world, this is hardly the case and the mutual inductance is always a fraction of the ideal value. Hence, a term, k, called the coupling constant is introduced to eq. (2.29).

$$M = k\sqrt{L_1 L_2}, \tag{2.30}$$

where, k is a value that ranges from 0, representing no inductive coupling to 1, for full inductive coupling.

2.1.3 Eddy-Current Induction

A coil carrying a time-varying current, located close to any electrically conducting material will generate a magnetic field defined by the Ampeère-Maxwell law, Maxwell's fourth equation.

$$\nabla \times \mathbf{H} = \mathbf{J} + \varepsilon \frac{\partial \mathbf{E}}{\partial \mathbf{t}} \tag{2.31}$$

where $\mathbf{H}$ is the magnetic field, and $\mathbf{J}$, the current density. The term $\varepsilon \frac{\partial \mathbf{E}}{\partial t}$ is Maxwell's correction to Ampeère's law and is referred to as the displacement current density. It means that the changing magnetic field is not entirely dependent on free electrons, but also on bound charges such as ionic or polar molecules[23, 35]. A consequence of this is that a magnetic field can also be generated by a time-varying electric field, even in the absence of flowing current. When an electrically conductive material is brought in proximity to the coil, eddy currents are induced in the material according to Faraday's law of induction (eq. (2.13)), as illustrated in fig. 2.2.
The induced eddy currents will flow perpendicularly to the orientation of the mag-

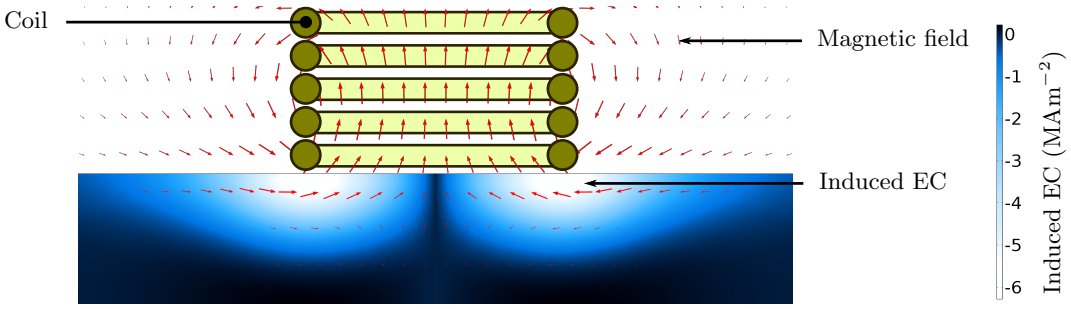

Figure 2.2: Eddy currents induced in a 1 mm thick aluminium block by a solenoid coil with 5 turns. The coil is carrying a time varying current at a frequency of 100 kHz. This 2-D axi-symmetric model was created using COMSOL multi-physics.

.

netic field, in a circular path as denoted by the curl ($\nabla \times \mathbf{E}$) in eq. (2.13).
The relationship between current density, $\mathbf{J}$ and electric field, $\mathbf{E}$ is defined by Ohm's law as,

$$\mathbf{J} = \sigma \mathbf{E}, \tag{2.32}$$

where, σ is the material conductivity. Substituting $\mathbf{J}$ for $\mathbf{E}\sigma$ in equation 2.31 will give:

$$\nabla \times \mathbf{H} = \sigma \mathbf{E} + \varepsilon \frac{\partial \mathbf{E}}{\partial t}, \tag{2.33}$$

Taking the curl on both sides,

$$\nabla \times (\nabla \times \mathbf{H}) = \nabla \times \left(\sigma + \varepsilon_0 \frac{\partial}{\partial t} \right) \mathbf{E}. \tag{2.34}$$

Applying the Laplacian relationship[i] , and then Maxwell's second equation, $\nabla \cdot \mathbf{H} = 0$, to the left hand side,

$$\nabla \times (\nabla \times \mathbf{H}) = \nabla(\nabla \cdot \mathbf{H}) - \nabla^2 \mathbf{H}, \tag{2.35}$$

eq. (2.34) becomes:

$$-\nabla^2 \mathbf{H} = \left(\sigma + \varepsilon \frac{\partial}{\partial t} \right) \nabla \times \mathbf{E}, \tag{2.36}$$

substituting for $\nabla \times \mathbf{E}$ from eq. (2.3), the equation becomes:

$$-\nabla^2 \mathbf{H} = \left(\sigma + \varepsilon \frac{\partial}{\partial t}\right) \mu \frac{\partial \mathbf{H}}{\partial t}. \tag{2.37}$$

Assuming the magnetic field incident on the sample to be a plane wave, the plane wave equation can be applied, $\mathbf{H} = \mathbf{H}_0 \exp(j(\omega t - \mathbf{kr}))$. Hence the first, and second derivatives of $\mathbf{H}$ with respect to time are:

$$\frac{\partial \mathbf{H}}{\partial t} = \frac{\partial(\mathbf{H}_0 \exp(j\omega t - j\mathbf{kr}))}{\partial t} = j\omega \mathbf{H}, \tag{2.38}$$

$$\frac{\partial^2 \mathbf{H}}{\partial t^2} = j\omega \frac{\partial(\mathbf{H}_0 \exp(j\omega t - j\mathbf{kr}))}{\partial t} = j^2 \omega^2 \mathbf{H} = \omega^2 \mathbf{H}. \tag{2.39}$$

Substituting the derivatives into eq. (2.37), it becomes:

$$\nabla^2 \mathbf{H} = (j\omega\sigma - \omega^2 \varepsilon)\mu \mathbf{H}. \tag{2.40}$$

Letting $k^2 = (j\mu\omega\sigma - \mu\varepsilon\omega^2) = j\mu\omega(\sigma + j\varepsilon_0\omega)$, the Helmholtz plane wave equation can be formed[36].

$$\nabla^2 \mathbf{H} - k^2 \mathbf{H} = 0. \tag{2.41}$$

where, k is the propagation constant, which determines the rate at which the magnetic field decays as it penetrates into the material, and is entirely dependent on the frequency, and material properties.

If the electrically conducting sample is assumed to be an infinite half-space whose surface is in the xy plane at $z = 0$, the magnetic field, $\mathbf{H}$, points in the z direction like a transverse wave. The energy transferred perpendicularly to its direction results in the induced electric field, E_0, in the xy plane. The wave equation for this geometry is:

$$\frac{d^2 H_x}{dz^2} - k^2 H_x = 0. \tag{2.42}$$

Using the plane wave approximation, let,

$$H_x = H_{0x} \exp(j\omega t - kz), \tag{2.43}$$

[i] $\nabla^2 V = \nabla(\nabla \cdot \mathbf{V}) - \nabla \times (\nabla \times \mathbf{V})$

where $k = \sqrt{j\mu\omega(\sigma + j\varepsilon_0\omega)}$, and H_{0x} is the magnetic field amplitude at the surface of the conductor. For a good conductor, $\sigma \gg \omega\varepsilon$ at typical operating frequencies[37], hence,

$$k \approx \sqrt{j\mu\omega\sigma}. \tag{2.44}$$

$\sqrt{j}$ can be written as $\sqrt{j} = (1+j)/\sqrt{2}$, hence k becomes:

$$k \approx \frac{1+j}{\sqrt{2}}\sqrt{\mu\omega\sigma}. \tag{2.45}$$

Defining k this way enables the separation of the propagation constant into real, and imaginary components, therefore

$$k = k' + jk'' \approx \frac{1}{\sqrt{2}}\sqrt{\mu\omega\sigma} + j\frac{1}{\sqrt{2}}\sqrt{\mu\omega\sigma}. \tag{2.46}$$

Applying this resolution to eq. (2.43), it becomes:

$$H_x = H_{0x}\exp(-\sqrt{\frac{\mu\omega\sigma}{2}}z)\ \exp(j(\omega t - \sqrt{\frac{\mu\omega\sigma}{2}}z)). \tag{2.47}$$

The real part of this equation $\exp -(k'z)$, describes the exponential rate at which the magnetic field changes with depth into the sample. The negative sign denotes that the field decays with depth into the sample. The imaginary term $\exp -(k''z)$ expresses the phase progression of the field with increasing depth.

Equation (2.47) shows that the magnetic field decays in amplitude, and lags in phase with increasing depth into the conductor. Hence, the electric field induced by the magnetic field should decay, and lag accordingly. The Ampeère - Maxwell law, when modified for a conductive medium ($\mathbf{J} \gg \varepsilon_0\frac{\partial \mathbf{E}}{\partial t}$) becomes:

$$\nabla \times \mathbf{H} = \mathbf{J}. \tag{2.48}$$

Considering the sample to be an infinite half-space whose surface is in the xy plane, at $z = 0$, the current can be expressed as a function of increasing depth, z, as:

$$-J_y = -\frac{dH_x}{dz}, \tag{2.49}$$

and substituting H_x from eq. (2.47),

$$-J_y = -\frac{d}{dz} H_{0x} \exp(-\sqrt{\frac{\mu\omega\sigma}{2}} z) \exp(-j\sqrt{\frac{\mu\omega\sigma}{2}} z) \exp(+j\omega t), \tag{2.50}$$

after applying the derivative,

$$J_y = (1+j)\sqrt{\frac{\mu\omega\sigma}{2}} H_{0x} \exp(-\sqrt{\frac{\mu\omega\sigma}{2}} z) \exp(-j\sqrt{\frac{\mu\omega\sigma}{2}} z) \exp(+j\omega t), \tag{2.51}$$

$$J_y = J_0 \exp(-\sqrt{\frac{\mu\omega\sigma}{2}} z) \exp(-j\sqrt{\frac{\mu\omega\sigma}{2}} z) \exp(+j\omega t). \tag{2.52}$$

where, J_0 is the current density at the surface of the conductor. The exponential terms in the equations for magnetic field, eq. (2.47), and current density, eq. (2.52) show identical rates of decay in amplitude, and phase lag.

2.1.4 The Skin Effect

The skin effect is a phenomenon, by which alternating current is concentrated towards the surface of a conductor, resulting in a considerable increase in resistance at high frequencies[36]. If eq. (2.52) is written as:

$$J_y = J_0 \exp(-\frac{z}{\delta}) \exp(-j\frac{z}{\delta}) \exp(+j\omega t), \tag{2.53}$$

the skin depth, δ, is defined as:

$$\delta = \sqrt{\frac{2}{\mu\omega\sigma}}. \tag{2.54}$$

This term, also referred to as the depth of penetration, is the depth into the conductor at which the current density has decayed to $1/e$ of the amplitude at the surface. It should be noted that current does flow below the skin depth, however, the density of current at this depth is about 37% of the surface current density. For small values of skin depth in a conductor, the AC resistance has approximately the same value it would have if all the current in the conductor were confined to a material depth equal the skin depth[38]. At this depth, the current will also be at a phase lag of 1 rad[39]. This quantity is an important consideration when selecting the frequency for eddy current tests as it determines the depth of defects, to which an eddy current measurement is most sensitive.

The electric field is in phase with the current density as shown in eq. (2.50), hence the lagging current below the conductor surface has an inductive reactance effect[36]. This means that, while assuming the current behaves as a plane wave,

the total current in the conductor, defined as an integral of the current density in the conductor will lag the induced surface electric field. For a conductor of infinite depth, the total current per unit width, I_w, is given by[36, 39]:

$$I_w = \int_0^\infty J_y dz, \tag{2.55}$$

$$= \int_0^\infty J_0 \exp -(\frac{z}{\delta})(1+j)dz \tag{2.56}$$

$$= J_0 \frac{\delta}{1+j} \tag{2.57}$$

The electric field, E_y at the surface is related to the current density by Ohm's law (eq. (2.32)):

$$E_y(z=0) = \frac{J_0}{\sigma}, \tag{2.58}$$

and in the case of a conductor with a unit surface area, the voltage, V_y has the same numeric value. Hence the internal impedance of the conductor, Z_s is given by[36]:

$$Z_s = \frac{V_y(z=0)}{I_w} = \frac{1}{\sigma\delta} + j\frac{1}{\sigma\delta}. \tag{2.59}$$

The complex impedance can be seen to have the form of a resistance, R, in series with an inductive reactance $j\omega L_i$:

$$Z_s = R_s + j\omega L_i, \tag{2.60}$$

where,

$$R_s = \omega L_i = \frac{1}{\sigma\delta}, \tag{2.61}$$

$$= \sqrt{\frac{\mu\omega}{2\sigma}} \tag{2.62}$$

Z_s is referred to as the internal impedance of the conductor, and assumes that all the current flows within the skin depth of the conductor. This demonstrates how both the resistive and reactive component of the material internal impedance are influenced by the skin effect.

From eq. (2.54) it can be seen that the depth of penetration in inversely

proportional to frequency, and this is an important consideration for eddy current measurements. For shallow surface defects, the frequency is typically increased to concentrate the density of induced eddy currents to shallower depths.

2.2 Eddy Current Measurement

Eddy current measurements are performed by measuring the changes in the secondary magnetic field as a result of eddy currents induced in a sample. This can be done using several types of magnetic sensors such as Hall-effect sensors, Giant magneto-resistive (GMR) sensors, and electromagnets. The work done in this thesis was carried out using electromagnetic solenoid coils to detect the magnetic field changes due to the presence of a material. The voltage, V across the coil is measured, which changes proportionally with respect to the coil impedance, Z, which will change depending on the properties of the material in proximity to it.

2.2.1 Electrical Impedance

Impedance is a component's total opposition to current flow, and is defined according to Ohm's law as:

$$Z = \frac{V}{I} = R + jX. \tag{2.63}$$

The impedance, Z, is a complex number that contains a real component of resistance, R, and an imaginary component of reactance, X. The reactance represents a dynamic opposition to change current flow, and is frequency dependent. It can be either inductive, X_L, or capacitive, X_C, and in most cases, it is a combination of both, and the components resistance. Inductive reactance is directly proportional to frequency, and given by:

$$X_L = \omega L \tag{2.64}$$

while, capacitive reactance is inversely proportional to frequency and given by:

$$X_C = \frac{1}{\omega C} \tag{2.65}$$

where, L, and C, is the inductance and capacitance of the system respectively, and $\omega = 2\pi f$, where f, is the frequency. The real, and imaginary components of

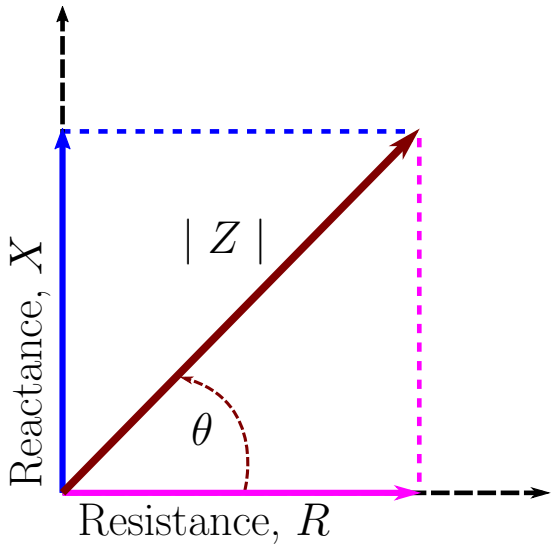

Figure 2.3: Complex plane diagram showing the relationship between the resistive, R, and reactive, X, components of the impedance, with the magnitude, $\mid Z \mid$ and phase, θ of the impedance.

impedance can be represented by a complex plane (Argand) diagram as shown in fig. 2.3, visually depicting the magnitude, $\mid Z \mid$, and phase, θ of the impedance. The magnitude, and phase of the impedance are calculated as:

$$\mid Z \mid = \sqrt{R^2 + X^2} = \sqrt{R^2 + (X_L - X_C)^2}, \tag{2.66}$$

$$\theta = \tan^{-1}\left(\frac{X}{R}\right). \tag{2.67}$$

The phase of the impedance represents the phase difference between the voltage, and current across the coil. For an ideal resistor, the impedance is entirely resistive, there is no reactive component ($X = 0$), and the phase is 0. Inductors and capacitors store energy, hence ideal versions of these will have entirely reactive components where, $R = 0$ (fig. 2.3). An ideal inductor will have a phase lead of $+\pi/2$, and an ideal capacitor, a phase lag of $-\pi/2$. Real circuit components such as wires will always have resistive impedance, and inductors such as coils will have parasitic capacitance, however at frequencies below resonance[ii], the effects are negligible[40].

[ii]Resonance is defined here as the frequency, where the coil voltage is in phase with the current, hence inductive and capacitive reactance are equal in magnitude, but cancel each other out in phase. When this occurs, the effects of parasitic capacitance cannot be ignored. The resonant frequency, f_0, is calculated as $f0 = \frac{1}{2\pi\sqrt{LC}}$[41].

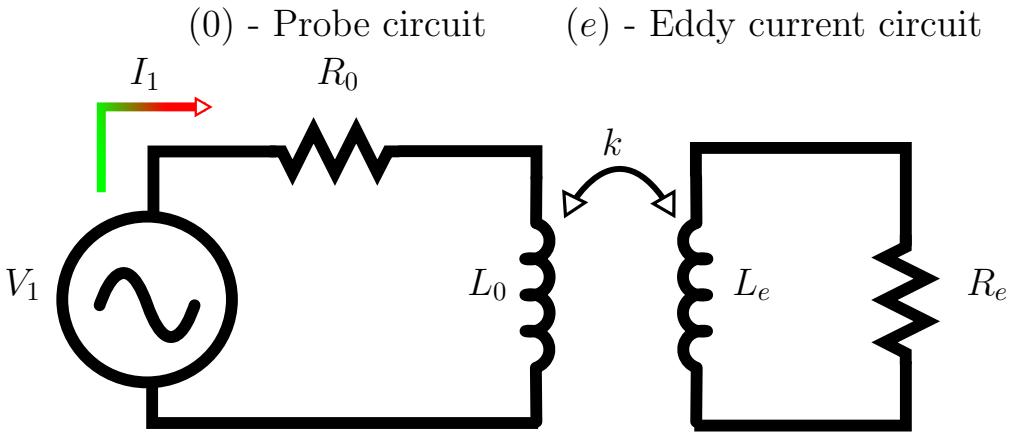

Figure 2.4: Equivalent transformer model representing the coupling interaction between an eddy current probe(0) and the eddy currents induced in surface of an electrically conducting test sample(e). The resistor in the eddy current circuit is not a real resistor, but a representation of the frequency dependent resistive properties of the conductive material, when eddy currents are induced. After [43].

2.2.2 Eddy Current Transformer Model

As shown in section 2.1, when a coil generating a changing magnetic field is brought in proximity to an electrically conductive material, there will be electromagnetic coupling between the coil and the induced eddy currents. This causes any changes in the eddy currents to be reflected in the electrical properties of the coil. This coupling interaction can be modelled as a transformer circuit[42], where the primary arm of the transformer is the probe circuit, and the secondary arm, the induced eddy current circuit, as shown in fig. 2.4, which assumes that the partitive capacitance is small enough to be ignored.

Kirchoff's laws can be used to determine the effective voltages in the primary, and secondary arms of the transformer[41].

$$V_1 = I_1(R_0 + j\omega Ł_0) + I_e(j\omega M), \tag{2.68}$$

$$0 = I_e(R_e + j\omega Ł_e) + I_1(j\omega M). \tag{2.69}$$

The mutual inductance, M, between the circuits as defined in section 2.1.2 is:

$$M = k\sqrt{L_0 L_e}, \tag{2.70}$$

where, k, is the coupling coefficient between the probe and conductive material, R_0, and L_0, are the resistance and impedance of the probe in air, and, R_e, and

L_e, the apparent internal resistance, and inductance of the conductive material. Rearranging eq. (2.69) to give I_e, it becomes:

$$I_e = -I_1 \frac{j\omega M}{R_e + j\omega L_e}, \tag{2.71}$$

Multiplying the numerator and denominator by the complex conjugate, $R_e - j\omega L_e$ gives,

$$I_e = -I_1 \frac{j\omega M R_e + \omega^2 M L_e}{{R_e}^2 + \omega^2 {L_e}^2}, \tag{2.72}$$

$$\frac{I_e}{I_1} = -\frac{\omega M}{{R_e}^2 + \omega^2 {L_e}^2}(\omega L_e + j R_e). \tag{2.73}$$

Substituting eq. (2.73) into eq. (2.68) gives,

$$\frac{V_1}{I_1} = Z_1 = R_0 + j\omega L_0 + \frac{\omega^2 M^2}{R_e + j\omega L_e}, \tag{2.74}$$

adding $+j\omega L_0 k$ to both sides of the equation [41], it can be written as,

$$Z_1 = R_0 + j\omega L_0 + \frac{\omega^2 M^2}{R_e + j\omega L_e} + j\omega L_0 k - j\omega L_0 k, \tag{2.75}$$

$M^2 = k^2 L_0 L_e$, hence the equation becomes,

$$Z_1 = R_0 + j\omega L_0 + \frac{\omega^2 k^2 L_0 L_e}{R_e + j\omega L_e} + j\omega L_0 k - j\omega L_0 k, \tag{2.76}$$

$$Z_1 = R_0 + j\omega L_0(1-k) + \frac{\omega^2 k^2 L_0 L_e + j\omega L_0 k(R_e + j\omega L_e)}{R_e + j\omega L_e}, \tag{2.77}$$

where Z_1 is the probe impedance. Equation (2.77) is the impedance of an an equivalent circuit representing a single probe inducing eddy currents in a conductive material. The term $L_0(1-k)$ is referred to as the leakage inductance due to the imperfect coupling between the probe and conductive material. Here the frequency dependent internal resistance of the material, R_e, is assumed to be the same order of magnitude as the internal reactance, $j\omega L_e$. In line with the equations derived in section 2.1.4, where it was shown that $R_e = j\omega L_e$ at all frequencies, the effective impedance of the coupled probe and conducive material can be written as,

$$Z_1 = R_0 + j\omega L_0 + \frac{\omega^2 k^2 L_0 L_e}{R_e + j\omega L_e}, \tag{2.78}$$

multiplying the numerator and denominator by the complex conjugate, $R_e - j\omega L_e$, gives,

$$Z_1 = R_0 + j\omega L_0 + \frac{\omega^2 k^2 L_0 L_e (R_e + j\omega L_e)}{{R_e}^2 + \omega^2 {L_e}^2}, \tag{2.79}$$

since, $R_e = \omega L_e$,

$$Z_1 = R_0 + j\omega L_0 + \frac{1}{2} k^2 \omega L_0 (1 - j), \tag{2.80}$$

$$Z_1 = Z_0 + \frac{1}{2} k^2 \omega L_0 (1 - j). \tag{2.81}$$

where, Z_0 is the probe impedance in air. This result enables the modelling of the circuit in fig. 2.4 as a single equivalent circuit with effective inductive, L_1, and resistive, R_1, components as shown in fig. 2.5[43, 44].

$$Z_1 = R_0 + j\omega L_0 + \frac{1}{2} k^2 \omega L_0 - j\frac{1}{2} k^2 \omega L_0, \tag{2.82}$$

separating the real, and imaginary terms of the impedance gives,

$$Z_1 = R_0 + \frac{1}{2} k^2 \omega L_0 + j\omega L_0 + -j\frac{1}{2} k^2 \omega L_0. \tag{2.83}$$

If the effective probe impedance is expressed as a series sum of the probe impedance in air, and the change in impedance as a result of the eddy currents, as shown fig. 2.5,

$$Z_1 = R_1 + j\omega L_1, \tag{2.84}$$

$$R_1 = R_0 + \Delta R = R_0 + \frac{1}{2} k^2 \omega L_0, \tag{2.85}$$

$$L_1 = L_0 + \Delta L = L_0 (1 - \frac{1}{2} k^2). \tag{2.86}$$

The equations expressed thus far have assumed that the effects of parasitic capacitance between the coil turns are negligible at frequencies well below resonance,

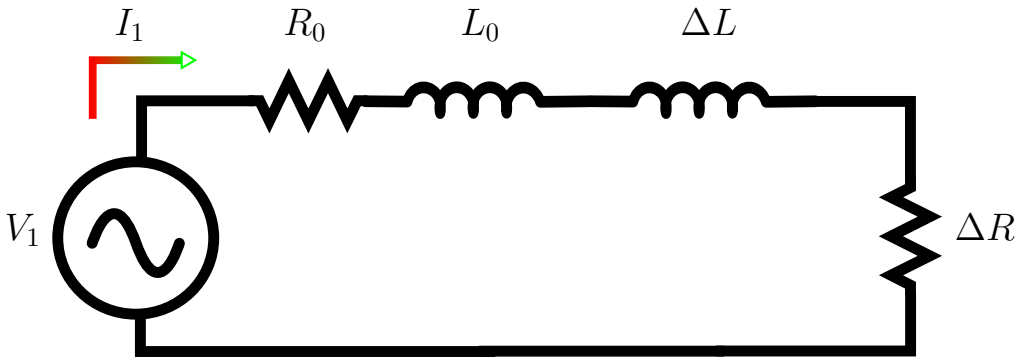

Figure 2.5: Equivalent inductive circuit for a coupled eddy current probe, and conductive material. The probe resistance, and inductance are represented by R_0, and L_0, while the changes in probe inductance, and resistance as a result of the induced eddy currents are represented as ΔR, and ΔL. After [43].

as stated in section 2.2.1. Figure 2.6(a) shows an impedance analysis of the coils used in this thesis. The black dashed line represents the maximum operating frequency of the probe, 2 MHz, and the plots are of the impedance magnitude, and phase of the coil over a frequency range of 40 Hz to 20 MHz. Resonance occurs at a frequency where the impedance magnitude is highest. At this point the coil reactance changes from inductive, with positive phase, to capacitive, with negative phase. For these coils, the resonance frequency is 14 MHz, when not connected to a coaxial cable. Connecting the coils to a 110 cm long, RG178 coaxial cable, the combined resonance frequency is reduced, as shown in fig. 2.6(b). The resonance frequency of the coil and cable combination is 2.8 MHz. This change in the resonance frequency is as a result of the reactance contributions of the coaxial cable.

Coaxial cables are frequently characterised by their capacitance per unit length, C_n, however, they have resistive, inductive, and capacitive components, and thus can be modelled as a transmission line. Figure 2.7 presents an illustration of the composition of a coaxial cable. They consist of two conductive mediums in the form of the core, and shielding, separated by a dielectric layer, which serves to restrict electric and magnetic field leakage, and interference.

A simplified transmission line model for a coaxial cable of length, h, consists of a lumped resistance, R, due to the finite resistivity of the core and shielding, connected in series to a lumped inductance, L, which is the sum of the self-inductances of the core and shielding. Shunted to these components are a lumped capacitance, which arises from the proximity of the core to the shielding layer, and a lumped conductance due to losses in the dielectric material [45, 46]. A circuit diagram for a coaxial cable of length, h, connected to a single coil is presented in fig. 2.8. This

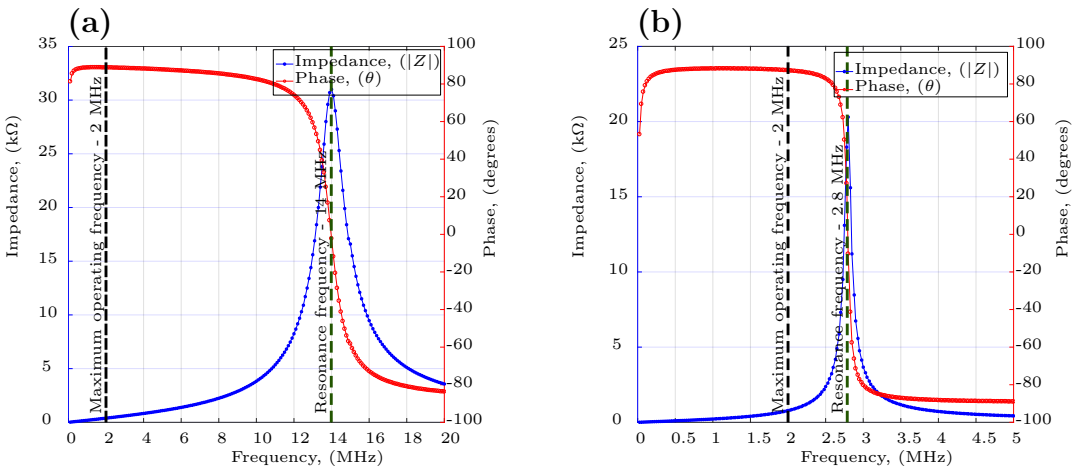

Figure 2.6: Impedance analysis of the coils used. The dashed line is at 2 MHz, the maximum probe operating frequency. Resonance occurs when the coil impedance is at its peak magnitude, and the coil reactance changes from inductive (positive phase) to capacitive(negative phase). (a) For these coils the resonance frequency is 14 MHz, when not connected to a coaxial cable, and (b) 2.8 MHz, when connected to a 110 cm long, RG178 coaxial cable.

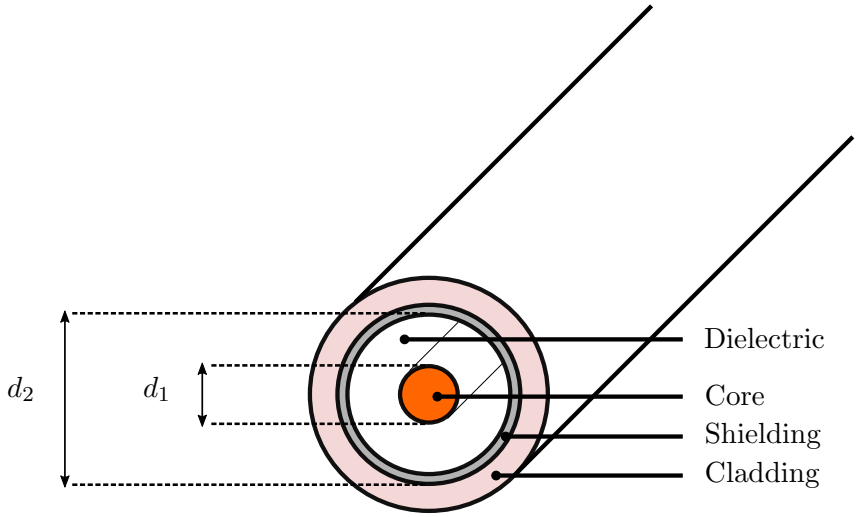

Figure 2.7: Illustration of the composition of a coaxial cable. It consists of a core for signal transmission, and shielding to ground the circuit. These are separated by a dielectric layer to restrict the leakage, and interference of electric and magnetic fields.

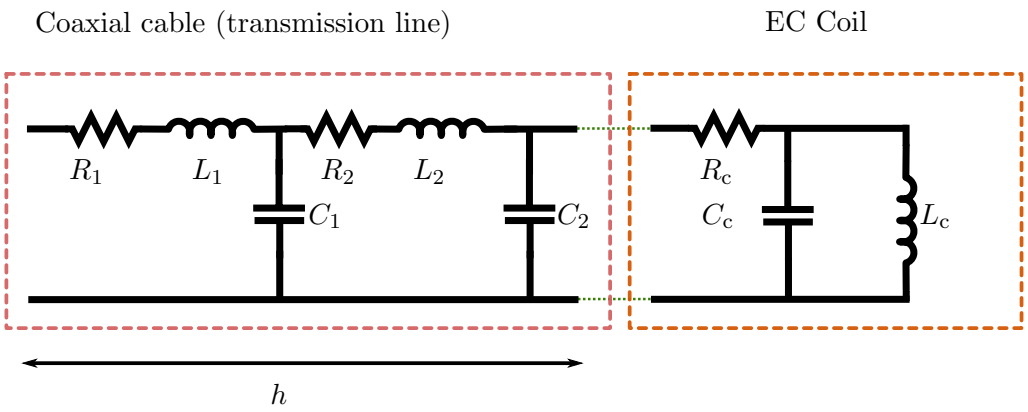

Figure 2.8: Circuit diagram for a single inductive coil connected to a coaxial cable transmission line with a length, h.

model assumes that the conductance contributed due to losses in the dielectric are negligible.

The values for the lumped components within each R-L-C circuit for the coaxial cable are for for a unit length of the cable, and equal to all other unit length components i.e. $R_1 = R_2 = R_n = R/h, L_1 = L_2 = L_n = L/h$, and $C_1 = C_2 = C_n = C/h$. The values for resistance, inductance, and capacitance per unit length can be calculated using the following equations[39, 45].

$$\frac{R}{h} = \frac{1}{\pi\sigma\delta}\left(\frac{1}{d_1} + \frac{1}{d_2}\right), \tag{2.87}$$

$$\frac{L}{h} = \frac{\mu}{2\pi}\log\frac{d_2}{d_1}, \tag{2.88}$$

$$\frac{C}{h} = \frac{2\pi\varepsilon}{\log\frac{d_2}{d_1}}, \tag{2.89}$$

where σ is the conductivity of the core, and μ and ε, are the magnetic permeability, and permittivity of the dielectric layer respectively. The term for skin depth, δ, in eq. (2.87) shows the dependence of the core resistance on frequency. Coaxial cable cores are often made up of interwoven strands of wire, however, this model is representative of a single wire core.

The transformer model equivalent eddy current circuit model presented assumed that for the frequencies of probe operation presented in this thesis, capacitance between the coil wire turns were negligible. These same assumptions apply to the coaxial cable. While the inherent inductive, and capacitive components of the of the coaxial cable caused a reduction in the resonance frequency of the system,

The operating frequency of the probe still remained well below resonance.

2.3 Summary

This chapter covers some of the fundamental principles applicable to eddy current testing. Equations describing the behaviour or eddy currents induced by a time varying magnetic field were discussed. It was noted that induced eddy currents are not plane waves, but assuming they behave as plane waves serves to show the frequency dependence of the density of eddy currents induced in an electrically conductive material. The skin depth was discussed, defined as the depth at which induced current density has decreased to 37% of the surface current density, which is at the maximum amplitude. The skin depth is an important parameter considered when performing eddy current measurements as it serves to determine the depth of defects for which an eddy current measurement is most sensitive at a given frequency.

The main parameters measured in EC tests were presented. For an eddy current sensor coil, the secondary magnetic field from induced eddy currents affect the coil inductance in ways, which when measured provide information on the material properties. The coil impedance is a complex value, comprised of the resistance, and reactance which is a function of inductance and capacitance.

Impedance analyses of the resonance behaviour of the sensor coils used in this thesis were presented. It was shown that the frequencies of probe operation were low enough that parasitic capacitance between the turns of the coil wires are negligible, and resonance had no effect on the tests. The connection of the coils to a 110 cm long RG178 coaxial cable decreases the resonance frequency of the coil probe due to the inductance and capacitance contributed by the coaxial cable, evaluated by the transmission line model of the coaxial cable. However, the reduced resonance frequency of the probe caused by the coaxial cable is higher than the probe operating frequencies.

There are other sophisticated models that consider the complexities of the system such as the effect of ferrite cores in the coil probe, mutual impedance between a pair of coils, and the skin effect in the coil windings. However, for the purposes of experiments conducted, the principles covered serve as useful approximations.

Chapter 3

Eddy Current Techniques

Eddy current testing (ECT) is based on measuring the magnetic field generated by eddy currents induced in an electrically conductive material. These measurements can be taken using a wide variety of sensor probe designs, and operational methods. This chapter presents a review of common ECT probe configurations and designs.

ECT inspection methods vary depending on the type of defects under consideration, material properties, and geometry. Hence, this chapter will concentrate on reviewing inspection techniques for surface breaking defects in flat, non-ferromagnetic materials.

3.1 Electromagnetic Coils

Electromagnetic coils are the most common elements used in the induction, and detection of eddy currents in materials. They offer good sensitivity at high frequencies, and are cheap to produce due to the simplicity of their construction. EC probe coils come in various shapes, and sizes, and discussed in the following sections are some of the approaches and considerations when designing EC sensor probe coils.

3.1.1 Coil Design

The coil geometry, and drive current frequency determine the density, and profile of eddy currents induced in the sample, and will influence the sensor's sensitivity to defects. When a coil is energized and brought in proximity to an electrically conducting material, eddy currents are induced in closed loops on the sample surface, directly beneath the coil wires. These eddy currents will flow in a path that is determined by the shape of coil shape, lift-off, and sample geometry. Larger coils will have a lager profile of eddy currents, covering more area, but at the expense

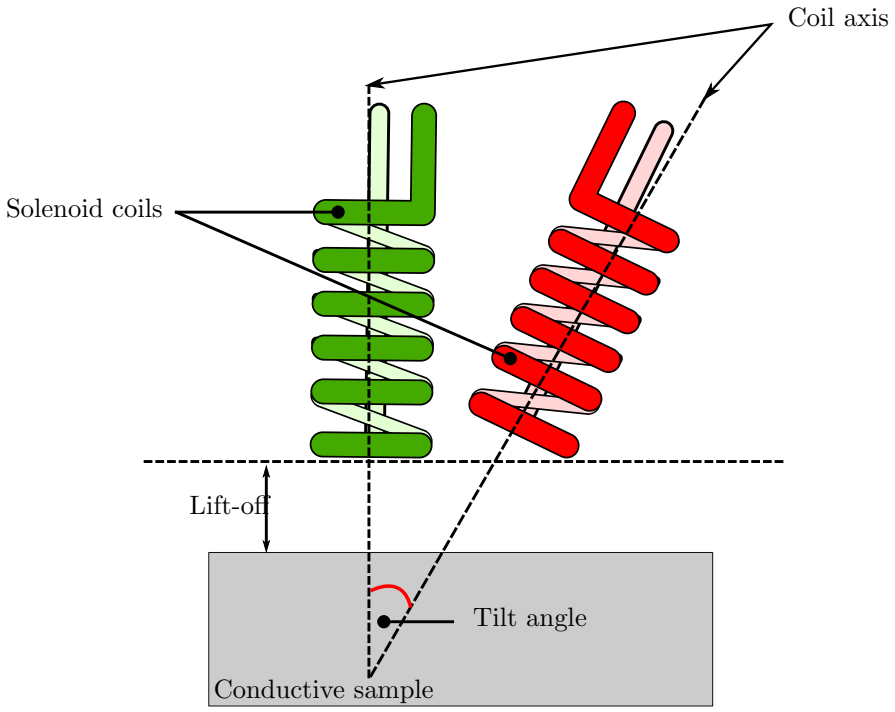

Figure 3.1: Illustration of solenoid coil positions relative to the conductive sample, showing probe tilt, and lift-off.

of defect sensitivity[47], as the potential for flaw detection is based on how much the flaw perturbs the flow of eddy currents(discussed in section 5.3). Commonly used in eddy current probes, are solenoid coils and planar coils such as pancake and rectangular coils.

Solenoid Coils

Solenoid coils have their windings primarily stacked parallel to the coil axis. They consist of cylindrical turns of wires often several layers high, and wide, hence they generate strong magnetic fields, which produce high eddy current densities in the test sample resulting in a high coupling factor, and good signal strength. They are however, very sensitive to lift-off, and probe tilt from the material surface (illustrated in fig. 3.1), which are major sources of noise in eddy current inspections[48, 49].

Solenoid coils are commonly used in encircling probes for testing bars or tubes, either internally, or externally. They induce eddy currents, which flow perpendicularly to the axis of the tube and coil, and as such they are sensitive to defects parallel to the coil axis, and less sensitive to defects oriented circumferentially on the test tube. Steam generator pipes are often tested internally using a solenoid coil, fitted with a bobbin, which keeps the probe horizontal as it is moved along the

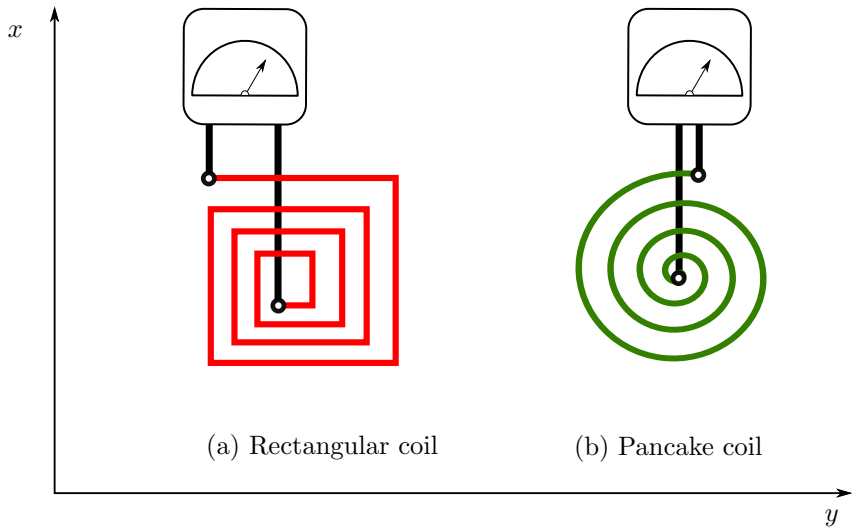

Figure 3.2: Top-down diagram of two kinds of planar coils. (a) Rectangular coil, and (b) pancake coil. If the coils axes are in the z direction (into the page), the coil windings are stacked perpendicular in the $x - y$, direction.

length of the tube[50]. The probes locate the defect by incorporating an encoder, which measures the distance of the defect from the edge of the tube[32]. A simple solenoid of N number of turns, with a cross sectional area. A, and length, l has an inductance, L which can be estimated as[51],

$$L = \mu \frac{N^2 A}{l}, \tag{3.1}$$

where μ, is the magnetic permeability of the coil core.

Planar Coils

Planar coils have windings stacked parallel to the coil axis as illustrated in fig. 3.2. Most commonly used forms of planar coils are the flat pancake spiral coil(fig. 3.2(b)), and in recent times, the rectangular coil (fig. 3.2(a))[52, 53, 31]. Pancake coils offer more coverage when compared to solenoid coils, at the expense of a lower eddy current density which leads to a reduced signal strength. They are also characterised by a comparatively low spatial resolution, as a result of the spread of induced eddy currents[47], hence if a defect smaller than the coil is picked up, it may be difficult to determine exactly where the crack is within the coil footprint.

For some applications, rectangular coils are considered superior to circular coils due to their ability to create directional and uniform eddy currents in certain regions of the coil footprint[53]. They are highly sensitive to shallow surface defects

and scratches at high frequencies[54], and are easily manufactured in printed circuit boards[55].

Ferrite Cores

The sensitivity of coils used in ECT is predominantly affected by inductance. The value of inductance calculated by eq. (3.1) can be increased by increasing the number of coil turns, or the coil area, or decreasing the coil length. The permeability of the core also greatly affects the coil inductance, and as such, increasing the coil permeability can significantly increase the coil inductance. This is done by introducing a ferrite core into the coil.

Ferrites are ceramic compounds of iron oxides (and other elements such as manganese of nickel and zinc), which are ferrimagnetic but non conductive. They are commonly utilised in EC probe coils for their ability to provide a high permeability even at high frequencies, unlike iron or steel cores. In addition, also unlike metal cores, their low conductivities suppress the induction of eddy currents within the cores[51]. The high magnetic permeability of the cores enable the focusing of the magnetic field generated by the coil, which increases the flux linkage between the probe and the test material, increasing the coil sensitivity to defects, as demonstrated in section 5.3. They have also been shown to be effective when used as a backing layer to pancake coils[56].

3.1.2 Probe Modes of Operation

Eddy current probes have various modes of operations, depending on the purpose, or limitations of the application. The coils within a probe can be operated in these modes either jointly, or separately. Summarised in this section are the most commonly used modes of probe operation.

Absolute Mode

Absolute mode (also known as reflection mode) is the oldest, and most common mode of probe operation[32]. It utilises a single coil for the generation of eddy currents, and the detection of the magnetic field in the test specimen (see fig. 3.3 (a)). The data measured from an absolute mode probe is the voltage across the coil, which is dependent on the coil inductance, and changes in the presence of a defect. This probe configuration is highly sensitive to temperature variations and is often used in conjunction with a reference inductor, located a way from the test sample. This reference inductor has the same impedance as the probe coil in air, and serves to

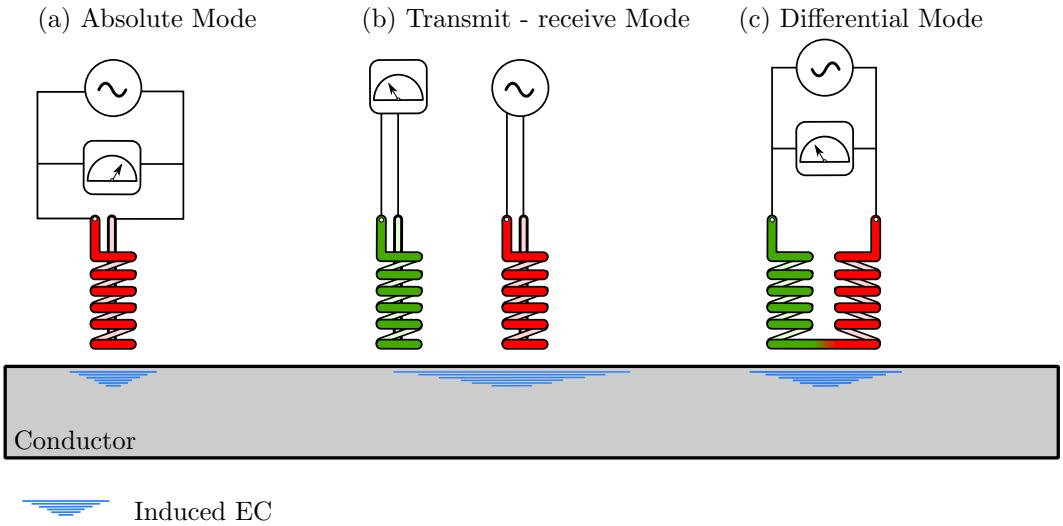

Figure 3.3: Circuit configuration for the most commonly used modes of operation of EC probes. (a) Absolute mode, which comprises of a single coil for the generation and detection of eddy currents. (b) Transmit-receive mode; one coil generates the eddy currents, while the other detects the magnetic field due to the eddy currents. (c) Differential mode; both coils are wound in opposition, and the difference in the coil voltages is measured. After [57].

compensate for the effects of temperature variations on the probe voltage. Perfectly matched inspection coils will return a a null voltage signal a defect is absent, which increases the dynamic range and the probe sensitivity to defects[32].

Transmit - Receive Mode

Transmit - receive probes (also known as separate-function probes), have one coil generating the eddy currents, and a separate coil detecting the magnetic field (see fig. 3.3(b)). A major advantage of this mode is that the respective coils can have designs, which are optimal for their function. The number of turns or permeability of the transmit coil can be increased, increasing the coil inductance, which increases the density of induced eddy currents, while the receive coil can have a design with minimised noise sources, and the optimal geometry for the detection of the defects under consideration.

Differential mode

In differential mode, the probe consists of two coils inspecting adjacent sections of the test piece as illustrated in fig. 3.3(c). They can be wound separately with their voltages subtracted after inspection, or wound as a single circuit of two coils with

turns wound in opposite directions. In either configuration, the output voltage for a differential probe is zero in the absence of a defect. The probes can be operated with both coils generating eddy currents, or as passive sensors for the detection of fields due to a separate excitation coil. Differential probe have high sensitivities to small defects and defect edges, but can be insensitive to gradual or long defects (i.e when both coils are on the defect the voltage cancels out). They are less susceptible to temperature variations, and lift-off, offering high signal to noise ratio, but can also be insensitive to defects with certain orientations[23].

3.1.3 Array Probes

One of the main disadvantages of single coil probes is the time it takes to perform 2-D surface scan. For small coils and defects, the spatial resolution is important, and when the scanning process is not automated, it can be a tedious exercise for the technician. Eddy current array (ECA) probes significantly reduce the time taken to perform an inspection[58]. They are comprised of identical sensing elements, which are activated in turn to perform an electronic scan, while the probe is physically scanned along the surface being inspected (illustrated in fig. 3.4), allowing larger areas to be scanned quickly. ECA coils can be operated in any of the modes discussed above, either individually or concurrently depending on test requirements. The electronic scan is performed by multiplexing through the coils in order to prevent cross talk between adjacent coils being simultaneously driven.

Hughes et al.[59], showed that high frequency eddy current systems perform better with electronics mounted as close to the coils as possible. They showed that cables between eddy current sensor coils, and the measurement electronics cause degradation in the measured inductance at high frequencies (> 1 MHz) due to parasitic capacitance in the cables having a more pronounced effect. They suggested that mitigating this drawback could be done by mounting the electronics just behind the coils. In a system with a single coil, or a pair of coils, this is feasible, however for an array system with multiple coils, and multiplexers, the electronics become a lot more complicated. ECA systems available currently do not perform well at frequencies higher than 1 MHz due to the factors mentioned, and are not routinely used for the inspection of low conductivity materials, which tend to require excitation frequencies higher than 1 MHz. One of the aims of this project is to investigate the utility of lower frequencies, for the inspection of low conductivity materials. At these low frequencies, an ECA system can be used for the inspection of the low conductivity materials with much less complicated electronics.

Many authors have shown the benefits, and drawbacks of ECAs. Mook et

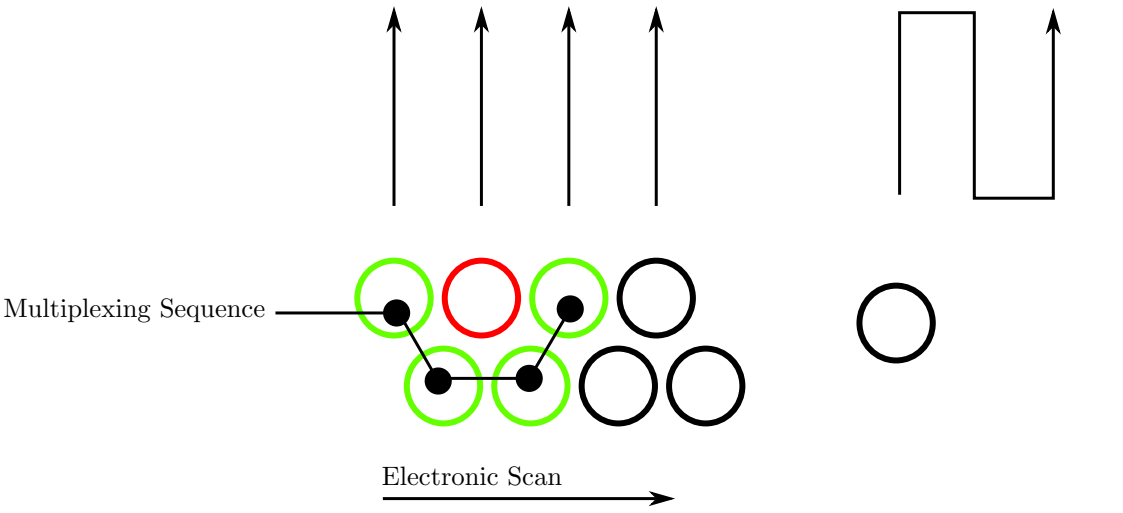

(a) EC Array (b) Single EC Probe

Figure 3.4: Comparison between the scanning process of (a) an ECA, and (b) A single coil EC probe. The array comprises multiple multiple identical sensing elements with are activated in turn for an electronic scan, while the probe is physically scanned along the surface of the test piece. To cover the same area, the single coil EC probe has to be raster scanned along the surface of the test piece. After [65].

al.[60], showed that in an array with identical coils, where each coil can be multiplexed through to serve the function of transmit, or receive, interference is reduced by driving and receiving from single elements within the array at any given time. However the presence of cores in the inactive array coils reduced the enhancement of coil-sample flux coupling provided by the cores in the active elements. They also showed that operating the array coils in transmit-receive mode provided two times the spatial resolution compared to absolute mode operation. Operating the elements in either mode have their benefits, and disadvantages, which are investigated in section 5.3. Zilberstein et al.[61], presented arrays made of meandering coils, which can be used to monitor the initial growth of fatigue cracks and small as 50 μm in high strength steel. More recently, flexible conformable arrays have been developed for the testing of complex shaped samples and harder to reach areas[62, 63, 64] by manufacturing printed circuit coils on flexible substrates.

Alternative Magnetic Field Sensors used in an ECA

Other methods for detecting eddy current magnetic fields have become increasingly popular due to their comparatively higher sensitivity over a broad range of frequencies, low noise and cost[66]. These sensors include, giant magneto-resistors (GMR),

hall probes, and superconducting quantum interference devices (SQUIDS).

Magneto-resistive Sensors

Magneto-resistance (MR) is a quantum-mechanical effect, which occurs in ferromagnetic materials, due to spin-orbit interactions of conduction electrons in the material[67]. Magneto-resistive sensors are transducers made from materials with great MR properties, enabling them to exhibit linear changes in resistance when influenced by an external magnetic field. They are highly sensitive, with high spatial resolution, with their drawback being high temperature coefficients[68].

Giant magneto-resistive (GMR) sensors are solid state devices with large MR properties. Much work has been done in demonstrating the effectiveness of GMR sensors. Chomsuwan et al.[69], demonstrated the use of a spin-valve type GMR in conjunction with a meander transmit coil to detect conductor disconnections ranging from 50 μm to 500 μm wide, in printed circuit boards. T. Dogaru and S. Smith[66] presented a highly sensitive probe comprising a flat pancake transmit coil, and a GMR sensor used to accurately detect, and size surface defects as small as 1 mm in length, and a subsurface defect 15 mm in length, with varying depths. They concluded that the spatial resolution of the probe is dependent on the dimension of the transmit coil, and the minimum detectable crack length is dependent on the mean radius of the coil. Along with C. Smith[70], they demonstrated the use of a EC based GMR sensor array to generate 2D images of cracks located at the edge of a test piece. GMRs measure the magnitude of the magnetic field unlike EC coil sensors, which measure the change in magnetic field. Hence, they have the advantage of being comparatively more sensitive at lower frequencies. They consume less power, and can be made with small dimensions, making them easily configurable into dense arrays[71].

Hall Probes

Hall-effect probes are also used to measure the magnetic field of eddy currents. Fundamentally, these transducers can measure the magnetic field by measuring its effect on the voltage across a current carrying conductor, or semiconductor[51]. The magnetic field deflects the electrons in the conductor, causing the current to fluctuate. Similarly to GMR probes, these sensors can be miniaturised, however, they suffer from high levels of $1/f$ (pink) noise[68], which makes them less effective at low frequencies[32].

Researchers such as He et al.[72], presented a probe comprising a single

cylindrical transmit coil excited by a broadband pulse current, and two differentially connected hall sensors, which they compared to a conventional differential eddy current probe. They performed tests on surface defects, 8 mm long, with varying widths and the same depth in riveted structures. They concluded that the hall sensor probe set-up provided no sensitivity improvements compared to the convectional EC probe. Passi et al.[73] compared a 3-axis hall-effect magnetometer to a classical hall-effect probe for testing superconductor homogeneity. They concluded that the measurement of the three components of the magnetic field by the 3-axis hall sensor provided higher sensitivity benefits compared to the single component of the magnetic field measured by the classical hall sensor. Fan et al.[74], presented sample thickness measurements of stacked aluminium, and copper layers using spectral phase data from a hall probe, and a pulsed eddy current transmit coil. They demonstrated that the coil voltage phase was less susceptible to noise attributed to variations in lift-off.

Superconducting Quantum Interference Devices (SQUIDS)

Superconducting Quantum Interference Devices (SQUIDS) are capable of detecting very weak magnetic fields, and are therefore effective at taking high resolution magnetic field measurements. They are made from superconducting semi circular loops of wire, connected via Josephson junctions[75]. While effective at measuring extremely weak magnetic fields, they have to be operated at cryogenic temperatures to maintain their super-conductive state, which limits their range of applications[68].

Various authors have researched non-destructive testing using EC based SQUID systems. Muck et al.[76] showed that in thick, highly conductive, or ferromagnetic materials, a SQUID based eddy current testing system showed a much higher sensitivity to defects, leading to a relatively higher probability of defect detection and sample testing speed when compared to a conventional EC system. They have also been shown to be effective at detecting eddy currents from excitation coils driven at frequencies as low as 22 Hz[77, 78], and demonstrated in field to successfully detect a 50 mm long slit-hole in a steel plate, at a lift-off of 50 mm - 100 mm[79].

3.1.4 Eddy Current Instrumentation

EC instruments are designed to be sensitive to the range of signals produced by different types of samples or test conditions. These conditions could be in the form of varying conductivities, or permeabilities of samples.

The most frequently used method for achieving relatively stable, and sensitive EC inspections is the electronic bridge circuit. There are many applicable kinds of bridges, the basic function of which is to balance the probe over an undamaged area of the test piece in order to get an accurate voltage indication when the probe is over a damaged section of the test piece. A basic bridge circuit (see fig. 3.5) comprises two fixed impedance elements(Z_1&Z_2), connected in series, and a variable impedance element, Z_{V}, connected in series to the load impedance, Z_{L}(the sensor). Both groups of series components are connected in parallel. The bridge is balanced by putting the sensor on an undamaged section of the test piece, and changing the variable impedance till the voltage across the voltmeter is null. The probe impedance can then be calculated using the voltage divider equation[23],

$$Z_{\mathrm{L}} = \frac{Z_2}{Z_1} \cdot Z_{\mathrm{V}}. \tag{3.2}$$

With the probe balanced, any change in the probe impedance during the test is indicated directly in the voltage across the voltmeter. This is an analogue difference measurement which can be highly sensitive, while being relatively unaffected by variations in the surrounding environment.

The variable impedance, Z_{V}, is often in the form of a reference coil. This coil can be mounted within the probe housing, oriented perpendicular to the receive coil sensor, and as far away from it as possible. When both coils are in air, this reference coil signal, and the receive coil signal are equal, and if they are wound in opposition, their signals cancel each other out. When the probe is placed on a test piece, the difference in the receive coil, and the reference coil signal is indicated in the voltmeter. A more sophisticated way of using the reference coil is to make it have properties as similar to the receive coil as possible (matched coils). This way during testing, the reference coil can be placed on a standard conductivity block with the same properties as the test piece. This enables more flexible, and sensitive measurements. More recently, *self reference* has been used in place of a reference coil[23]. The probe is placed on a reference block with the same properties as the test piece, or in some cases, an undamaged part of the test piece. The probe is *balanced*, by measuring the voltage across the receive coil, and storing it electronically. As the probe scans along a the section of the test piece of interest, the test signal is compared with the measured reference signal. Since finding two perfectly matched coils is very difficult, this method provides the advantage of having identical 'reference', and 'test' coils[23], and a bridge is not required.

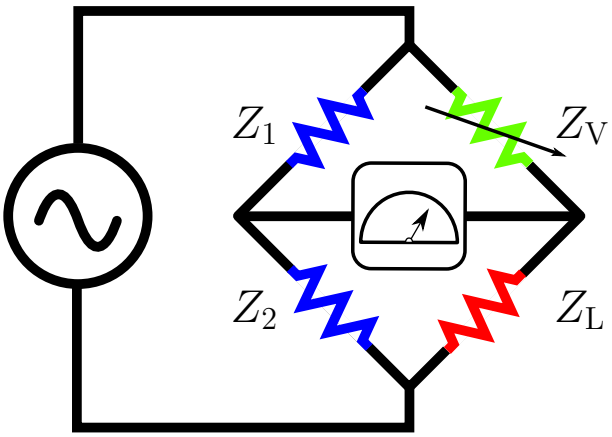

Figure 3.5: Schematic circuit diagram of a Wheatstone bridge showing the fixed impedance elements Z_1 and Z_2, a variable impedance element Z_V, and the load impedance Z_L. The bridge is balanced, and voltage across the voltmeter null, when the ratio between the fixed impedances is the same as the ratio between the variable impedance and the load impedance.

3.1.5 Eddy Current Excitation

The fundamental operation of EC probes is the detection of generated eddy currents induced by a changing magnetic field. This requires that the coil inducing eddy currents is carrying an alternating current. The simplest form of eddy current excitation is a constant amplitude sinusoidal wave current, however, there are other more sophisticated methods of creating the changing magnetic field for eddy current measurements.

Multi-Frequency Measurements

Standard EC measurements use a single sinusoidal wave alternating current. The sine wave frequency is selected based on the material properties of the test piece, and the depth of the defects of interest. The frequency of the excitation current field determines the depth of penetration into the material (see chapter 2), hence EC probes are often driven at high frequencies for the inspection of low conductivity materials, or to detect very small defects. In some cases however, a deeper penetration into the material is desired, and one solution could be to decrease the excitation frequency, which would increase the depth of penetration. However, this comes at a cost of sensitivity to shallower surface defects, as the eddy currents could flow below the defect. Furthermore, Faraday's law states that the induced voltage is proportional to the rate of change of magnetic field, hence a slower changing magnetic field will induce less dense eddy currents, which may be harder to detect by

the probe.

Measurements at multiple frequencies will generate eddy currents flowing at different depths. This data can be analysed to acquire more information about discontinuities in the test piece[80]. The multi-frequency measurement process involves acquiring EC signals at two or more test frequencies, combined in a manner at which noise from sources such as lift-off, material geometry variation, and temperature effects can be minimised, hence improving the signal to noise ratio[47, 6, 81].

Authors such as Bartels and Fisher[82] have shown a multi-frequency eddy current imaging technique, which combines 2-D surface images taken at multiple frequencies to isolate defects of different sizes and depths in a test piece. They showed that linearly combining the magnitude, and phase of the complex data measured from a four frequency inspection, significantly improved the signal to noise ratio by up to 1100%.

Pulsed Eddy Current Measurements

Pulsed eddy current testing (PEC) involves the use of an excitation current composed of a wide spectrum of frequencies, which enables a simultaneous inspection at different depths into the test piece[83]. In recent times, PEC has gained considerable research interest due to its effectiveness at the detection, and quantification of both surface and subsurface flaws in conductive materials, resulting from the ability to utilise multiple frequencies, which match depths of interest[84, 85]. Conventional ECT is highly susceptible to noise due to probe lift-off. Tian et al.[86] present a study of the lift-off invariance of different PEC configurations when performing sample conductivity measurements, and concluded that the accuracy of the measurements were unaffected by variations in lift-off between the probe and the sample.

The rate of change (rise time), and width of the excitation pulse determines its frequency composition. A steep rise results in the pulse being composed of high frequencies, which are more applicable to the detection of small surface defects. Conversely, a more gradual rise results in lower frequencies enabling more penetration into the test sample for the detection of deeper defects[87]. The pulse width determines the frequency bandwidth within the pulse[51].

The previously discussed detection sensors are also applicable to PEC. Hall, and GMR sensors perform much better than EC coils for PEC due to their sensitivity at low frequencies, required to detect sub surface defects[88].

3.1.6 Summary

This chapter discusses some of the most common techniques used in eddy current testing. Some types of conventional EC coils, considerations for the construction, and selection of the coils, and their applications were also covered. The common modes of operation of eddy current coil probes, which include absolute, transmit-receive, and differential modes were discussed, with their relative benefits and drawbacks summarised.

Other common sensors for the detection of eddy current magnetic fields in ECT measurements include the Hall sensor, the Giant Magneto-resistive sensor (GMR), and the Superconducting Quantum Interference Device (SQUID). These sensors have their benefits and drawbacks, with their main benefit over conventional EC soil sensors being their high sensitivity at low frequencies.

Conventional EC probes are excited by a single frequency sinusoidal wave current, which limits flexibility with regards to the depth of the sample at which defect measurements can be conducted. Other methods of excitation include the use of multiple sinusoidal wave currents with different frequencies, and the combination of the resulting data, which has been shown to increase the signal to noise ratio of 2-D surface images. Pulsed eddy current excitation was also discussed, which involves the use of a current pulse containing a band of frequencies for excitation.

Chapter 4

Improving the Signal to Noise Ratio of Eddy Current C-scan Data

4.1 Experimental Method

An experimental system was developed to generate C-scan images of surface breaking defects in stainless steel (AISI Type 316). Stainless steel, and other low conductivity materials such as titanium, and titanium aluminide have high strength, and low densities, and are widely used in industry due to their favourable properties[89]. The electrical properties for these materials are listed in table 4.1[90, 91, 92, 93] at room temperature, 20°C. The stainless steel samples are in the form of blocks and plates of varying shapes, widths, and thickness, with laser micro-machined defects on them. Table 4.2 lists the dimensions of the defects on text blocks. Industrial eddy current methods can reliably detect cracks as small as 0.75 mm long, and 0.38 mm deep [43], but there is a drive to improve detection limits, hence defects as small as 0.25 mm were tested in these experiments.

An array system consisting of a function generator, oscilloscope, multiplexers, a microcontroller, and four solenoid coils as presented in fig. 4.1 was used to conduct preliminary experiments. The multiplexers served as switches enabling the use of the coils within the probe as transmit coils, and receive coils. The multiplexers are controlled using an Arduino microcontroller. Tests using this system produced initial results, however, further analysis was required. A subset of this system was developed which used a probe consisting of two solenoid coils. With this new system, the microcontroller and multiplexers are not required. Figure 4.2

Material	Electrical resistivity ($\mu\Omega$m)	Conductivity (MSm^{-1})
Stainless steel (AISI Type 316)	0.77	1.30
Titanium (Ti)	0.78	1.27
Titanium aluminide (γ-TiAl)	2.29	0.44

Table 4.1: Electrical resistivity, and conductivity values for the materials tested. After[90, 91, 92, 93]

Length (mm)	Depth (mm)	Width (mm)
2	1	0.1
1	0.5	0.1
0.5	0.25	0.1
0.25	0.125	0.1

Table 4.2: Dimensions of the defects tested.

presents a schematic diagram of the new system used to perform the experiments presented in this chapter. The experimental set-up consists of a function generator generating a sinusoidal wave voltage, driving a Howland current source, which keeps the transmit coil current constant. An X-Y stage is used to take the 2D C-scans, and an oscilloscope for voltage measurements.

The Tektronix AFG3052C function generator was used to generate a $\pm$500 mV sinusoidal wave voltage, which is converted to a constant amplitude, $\pm$50 mA current by the Howland current source [94], which drives the transmit coil. The Howland current source has a 10 Ω resistor connected in parallel to the transmit coil, which enables the measurement of the change in voltage across the transmit coil. The current source also serves to enable easier data processing and comparison to FE models, as it keeps the amplitude of the sinusoidal wave current through the transmit coil constant. This means that the coil voltage will change linearly as the coil impedance changes. Thus, the change in coil impedance can be measured directly by measuring the change in coil voltage. This function negates the need for a bridge circuit commonly used in conventional eddy current systems. The sinusoidal wave current amplitude was observed to not be perfectly constant, but the variation, which was measured to have a standard deviation of 2 mA is small enough to not have a noticeable effect on the experimental measurements. The voltages are measured using a Tektronix DPO4104B-L oscilloscope. The X-Y stage used for taking the scans is a Zaber X-LSM linear stage, with a minimum step resolution of 0.099 μm per step. The probe is mounted onto the X-Y stage with a 0.2 mm clearance between the base of the probe and the surface of the sample

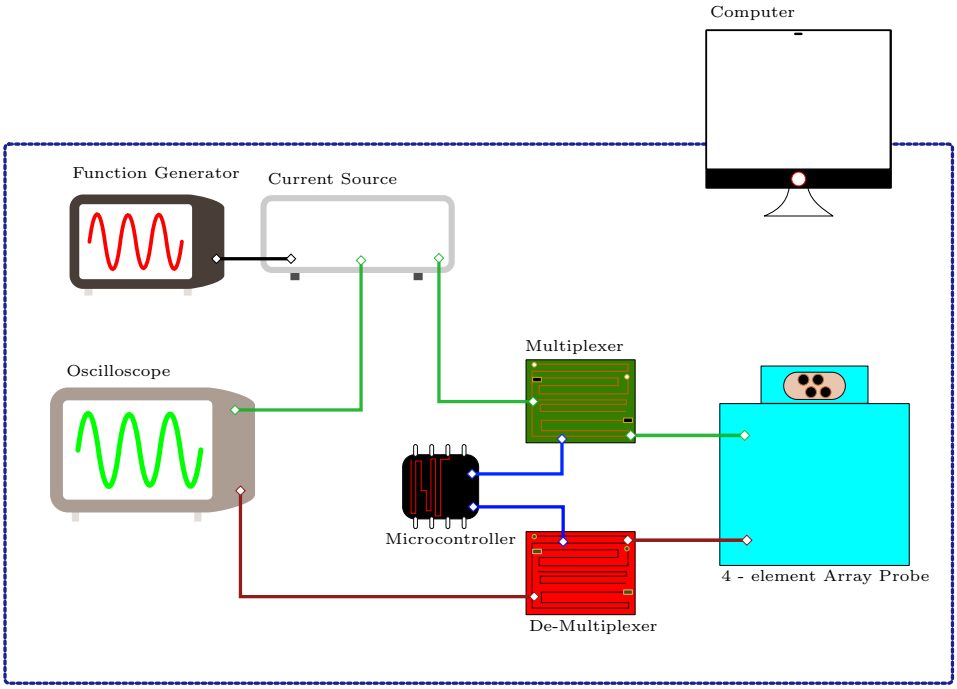

Figure 4.1: Schematic diagram of the experimental set-up for a 2D single frequency C-scan of a conductive test piece using an eddy current array probe consisting of four solenoid coils. The multiplexers switch between the coils enabling them to act as both transmit, and receive sensors in turn.

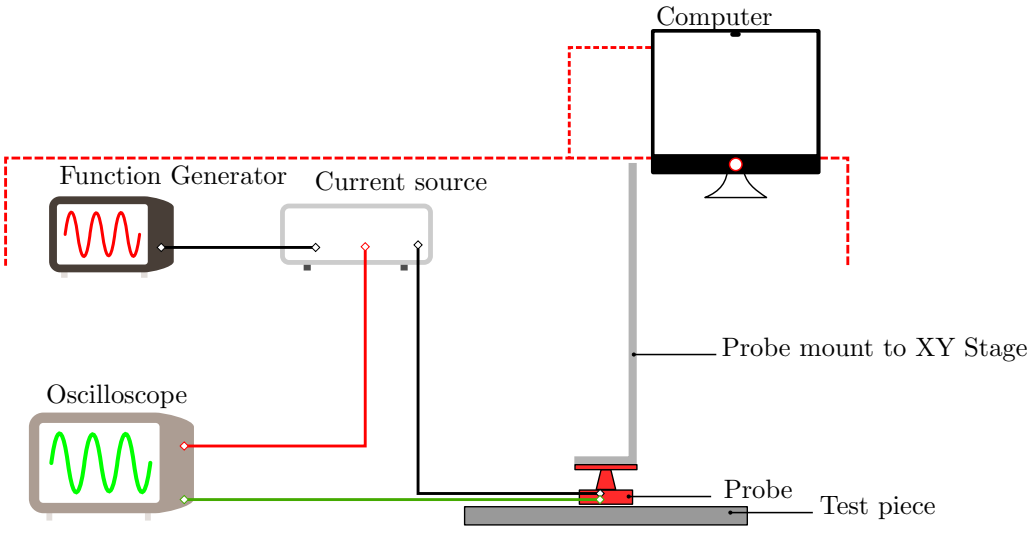

Figure 4.2: Schematic diagram of the set-up for a 2D single frequency C-scan of a conductive test piece. The function generator is used to generate a sinusoidal wave voltage, with which an constant amplitude alternating current is generated by the Howland current source. An automated C-scan is taken using the X-Y stage controlled by the computer, and the voltage across the coils is measured by the oscilloscope, and then transferred to the computer for post processing.

being tested. The probe holder would usually be spring loaded, or weighed down to decrease coil lift-off as much as possible, and to decrease the effect of variations in the flatness of the sample surface. The reason for the clearance between the probe and sample was to prevent the probe from scraping on the sample surface, which introduced errors into the measurements. The components are controlled with a computer running programs created using either Labview, Matlab, or Microsoft C#.

The scans are taken using a coil probe containing two coils, arranged side by side. The coils have identical specifications, comprising four layers with 25 turns per layer to make 100 turns in total. They are wound from thin copper wires (0.063 mm in diameter), have internal and external diameters of 0.90 mm, and 1.15 mm, respectively, and heights of 1.58 mm. The coils used were designed to detect 2 mm long defects in the materials considered. The coil diameter determines the spatial resolution to which the defects can be sized, thus a diameter of 1.15mm will serve to accurately detect, and size a 2 mm long defect. The number of coil turns, and the coil diameter also determine the coil inductance. The thin copper wires were used to reduce the coil footprint, while keeping a high number of turns to give a sensitive coil with a sufficiently high inductance. These coil parameters were ideal for the detection and sizing of the 2 mm long defect, but as shown in chapter 5 they are not ideal for the sizing of 0.25 mm and 0.5 mm long defects. This is because the coil diameter is wider than the length of these defects. Optimizing the coils for the sizing of the 0.25 mm and 0,5 mm long defects will involve making the coils even smaller, and the resources to do that were unavailable at the time. However, with the aid of the FE models, it was shown that the sub-millimetre defects could be accurately detected using these coil parameters. The coils contain low permeability ferrite cores, with $\mu_r = 40$[95], to increase coil sensitivity as shown by the models comparing scans with and without ferrite cores in section 5.3.1. The coils are not shielded from each other, and this is to maximise the inductive coupling between them.

Each coil is connected to a 110 mm long RG178 coaxial cables, and each coil and cable combination has a characteristic inductance of $L_0 = 21 \pm 3.5\mu$H at 300 kHz, when not in proximity to a conductive test piece. At this frequency, each coil and cable pair has a combined impedance of 49.4 Ω to match the 50 Ω output from the Howland current source, and 50 Ω input to the oscilloscope. Low conductivity materials such as those inspected in this thesis are more commonly inspected at frequencies much higher than 300 kHz ($>$ 2 MHz). However, for an EC measurement system to perform well at such high frequencies, the electronics have

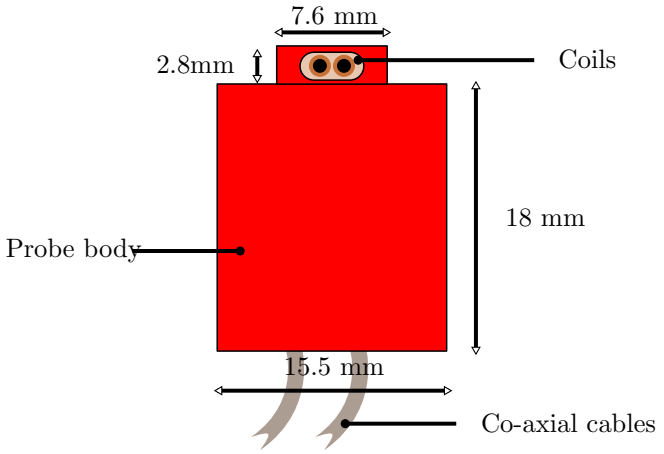

Figure 4.3: Illustration showing the arrangement of the probe coils, and the dimensions of the probe body. The coils are wound from copper wires, 0.063 mm in diameter. They have identical specifications including; 100 turns, internal and external diameters of 0.9 mm, and 1.15 mm respectively, and heights of 1.58 mm. The probe body was 3D printed from acrylonitrile butadiene styrene (ABS) plastic.

to be located close to the coils to avoid the use of coaxial cables between the coils and the electronics as demonstrated by Hughes et al in [59]. Thus, to circumvent these issues, the coils are driven at sub MHz frequencies, and 300 kHz was selected as it best matched the coil impedance to the impedance of the Howland current source, and the oscilloscope. The ability to detect such small defects in low conductivity materials at 300 kHz is a significant improvement over current systems available in the market. The probe body was 3D printed using acrylonitrile butadiene styrene (ABS) plastic. The probe dimensions are illustrated in fig. 4.3.

Impedance analysis for the coils used in these experiments was presented in section 2.2.1, However, the impedance response of the coil changes when another coil is in close proximity to it. The impedance response over a frequency range of 40 Hz to 5 MHz for one of the coils connected to a 110 mm long, RG178 coaxial cable is presented in fig. 4.4. The maximum operating frequency defined for these experiments is 2 MHz denoted by the black dashed line. Due to the proximity of the two elements within the probe, resonance occurs at 2.94 MHz, and 3.44 MHz. The resonance events in fig. 4.4 correspond to each roil resonating at these frequencies, and is reflected in the impedance response of this one coil because of the magnetic flux coupling between the coils.

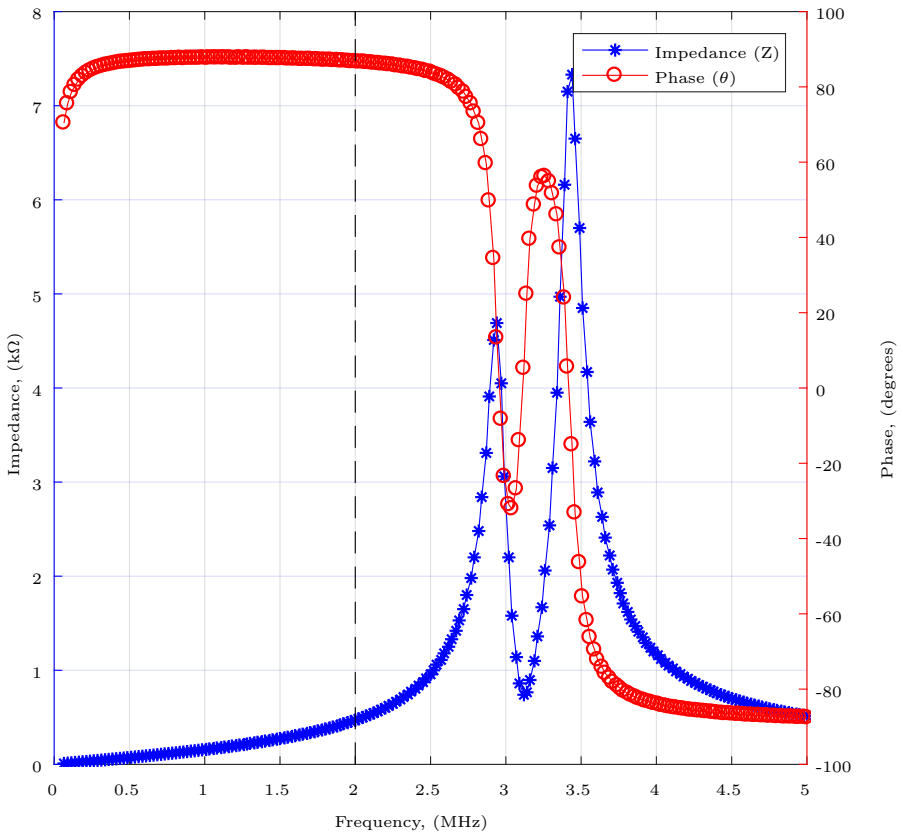

Figure 4.4: Impedance analysis for one of the coils in the two coil probe connected to a 110 cm RG178 coaxial cable. The maximum operating frequency for these experiments is 2 MHz denoted by the black dashed line, and resonance occurs at 2.94 MHz, and 3.44 MHz.

4.2 Data Processing

In eddy current testing, the effects of the material's properties on the coil impedance is measured. Since the current in the transmit coil is kept constant, the coil voltage will reflect the same changes in the coil impedance. The sinusoidal wave coil voltage can be represented as a complex value, $V = a + jb$. The complex components of the voltage are used to generate C-scan images mapping the defects on the test piece. Figure 4.5 presents a typical plot of the sine wave voltage across the coils. Voltage across the coils in this plot is a sine wave, at a frequency of 300 kHz. It has been averaged 16 times to minimise noise, and to enable an accurate measurement of the amplitude, and phase of the voltage. 16 averages are taken as tests showed that more than 16 averages took more time to record, and showed no improvement in the data. The effects of the material on the coil voltage phase tends to be so small, that a high sampling rate is required to measure it. The sampling rate for this data is 2.5 GSs^{-1}. More important than the sampling rate for measuring phase is the amount of intrinsic time jitter on the oscilloscope. This is specified in the oscilloscope manual as the long term sample rate and delay time accuracy, and is measured in parts per million over a $\geq$ 1 ms time interval. Phase measurements from initial experiments using a Tektronix DPO3034, with a long term sample rate and delay time accuracy of 10 ppm, produced noisy and unusable phase measurements. The higher specification Tektronix DPO4104B-L oscilloscope has a long term sample rate and delay time accuracy of 5 ppm, and was used to take the phase measurements presented in this thesis.

The magnitude, and phase of the voltage are used to construct the C-scan images. Coil voltage magnitude, $|V|$, and phase, θ, are calculated as,

$$|V| = \sqrt{a^2 + b^2}, \tag{4.1}$$

$$\theta = \tan^{-1} \frac{b}{a} \tag{4.2}$$

The probe is used to scan the test piece, with the amplitude, and phase of the voltage measured at each step of the scan. Two methods of measuring the voltage amplitude and phase are evaluated. The first method is to fit a sine wave to the voltage data, and use the parameters of the fitted sine wave to evaluate the amplitude, and phase[96].

$$y = \sum_{i=1}^{n} a_i \sin(b_i x + c_i), \tag{4.3}$$

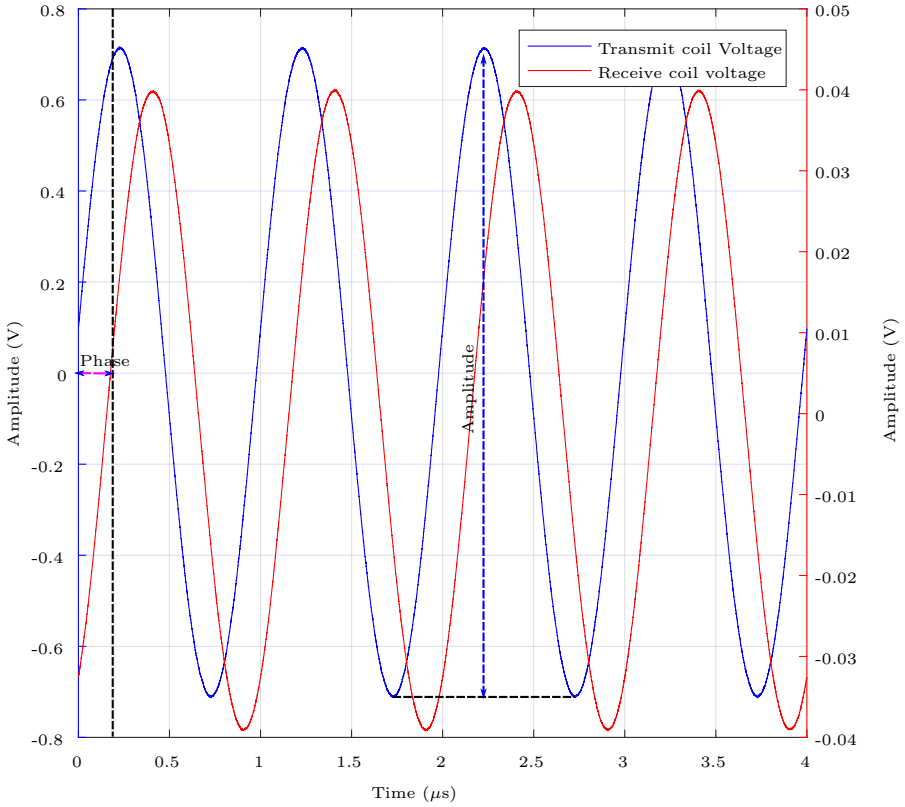

Figure 4.5: 300 kHz sine wave voltages across the transmit and receive coils for 4μs, showing the parameters measured as the amplitude and phase of the voltage signal. The data was sampled at 2.5 GSs^{-1}, and averaged 16 times to minimise noise.

where, a_i is the amplitude, b_i the frequency, and c_i, the phase. This is achieved using the 'sum of sines' algorithm available in the Matlab digital signal processing toolbox. The second method is to perform a fast Fourier transform (FFT)[97] on the voltage data, to convert it from time domain, to frequency domain data, and to use the amplitude, and phase of the transformed data at the drive frequency. Both methods produced similar data, with differences being the form of the data produced, and computational speed. Fitting a sine wave enabled the evaluation of the exact values for the amplitude, and phase of the voltage, whereas with the FFT, values related to the amplitude, and phase are retrieved. The most accurate fit was achieved using a sum of 2 sine waves, with no improvements observed when more sine functions are fitted. Fitting sine functions to the data however, took considerably more time to compute than using a fast Fourier transform. For the application of generating C-scan images, the exact values of voltage, and phase are not required, as the relative change in voltage as the probe scans the material is the important information. Therefore the magnitude values generated by the FFT are used for generating the images.

4.2.1 Impedance Matching

The impedance of the coil, coaxial cable, and termination impedance of the oscilloscope are very important considerations when performing the eddy current measurements. The RG178 coaxial cable has a characteristic impedance of 50 Ω, and each coil, and coaxial cable combined has an impedance of 49.4 Ω, at 300 kHz. To get the maximum transfer of power to the oscilloscope, and to minimise reflections [46], which will affect the measured amplitude, and phase values, the oscilloscope has to have a termination impedance of 50 Ω, to match with the 50 Ω output impedance at the Howland current source terminals, and the 50 Ω characteristic impedance of the coaxial cables. The coaxial cables connected to the coil behave as transmission lines (see chapter 2), thus terminating the transmission line at its characteristic impedance minimises reflections[36]. Figures 4.6 and 4.7 compares plots of the magnitude, and phase of the transmit, and receive coils for varying termination impedances at the oscilloscope.

These plots show the severe degradation of data that can result from an impedance mismatch between the oscilloscope and the rest of the circuit. Terminating at 1 MΩ when coil and coaxial cable impedance is close to 50 Ω results in data that is not only noisy but does not accurately reflect the defect being scanned. The noise due to reflection resulting from an impedance mismatch is more visible in the phase data, where amplitude data is rendered inaccurate.

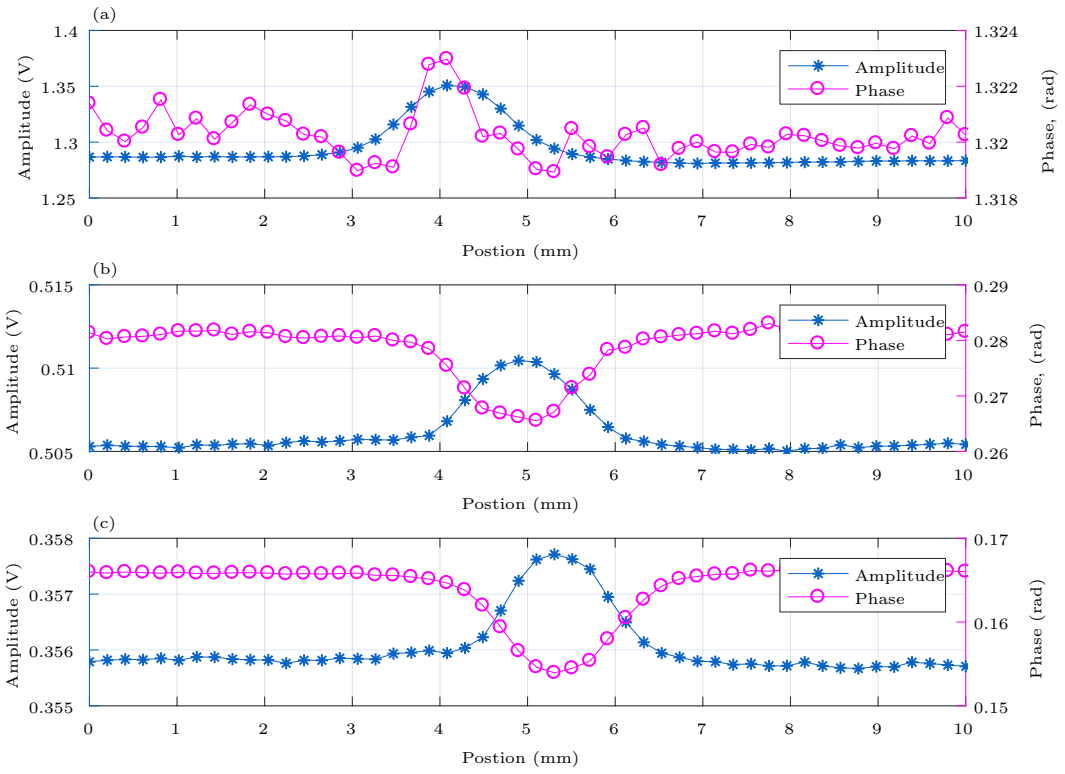

Figure 4.6: Amplitude, and phase of the transmit coil voltage, for a 300kHz line scan of a 2 mm long defect in stainless steel. The oscilloscope was terminated at (a) 1 MΩ, (b) 75 Ω, and (c) 50 Ω. The data accuracy improves from (a) to (c); with (c) reflecting the most accurate indication of the defect, and the least amount of noise in the phase measurements.

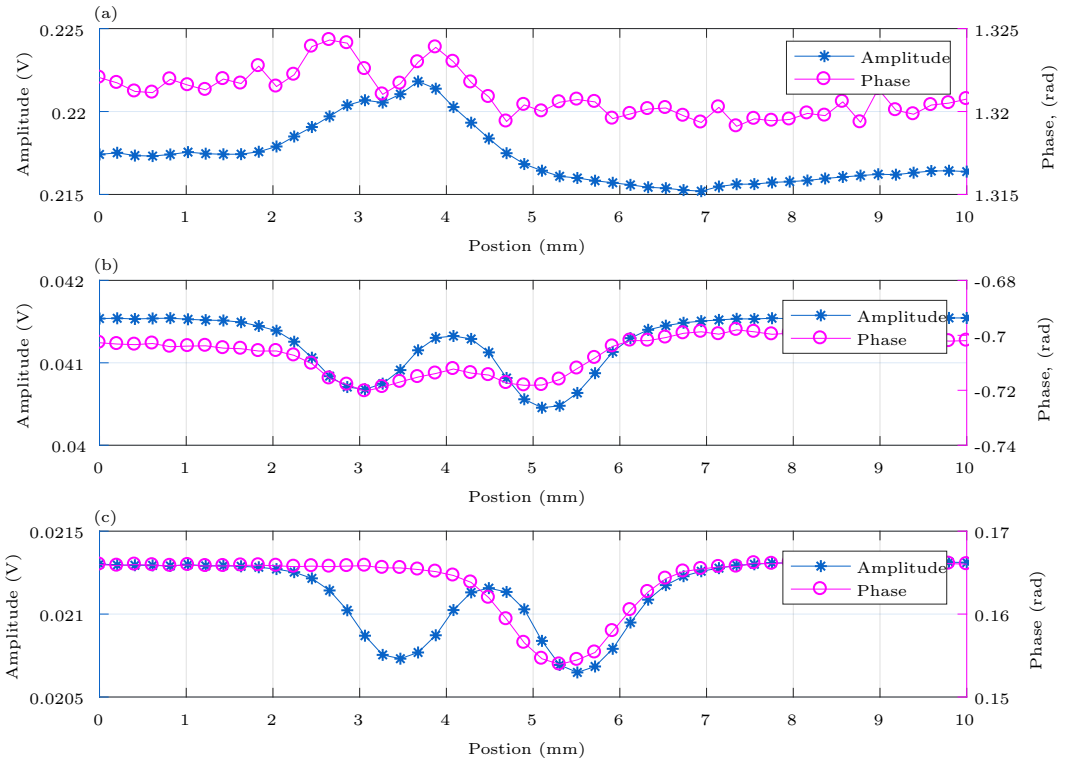

Figure 4.7: Amplitude, and phase of the receive coil voltage, for a 300kHz line scan of a 2 mm long defect in stainless steel. The oscilloscope was terminated at (a) 1 MΩ, (b) 75 Ω, and (c) 50 Ω. The data accuracy improves from (a) to (c); with (c) reflecting the most accurate indication of the defect, and the least amount of noise in the phase measurements.

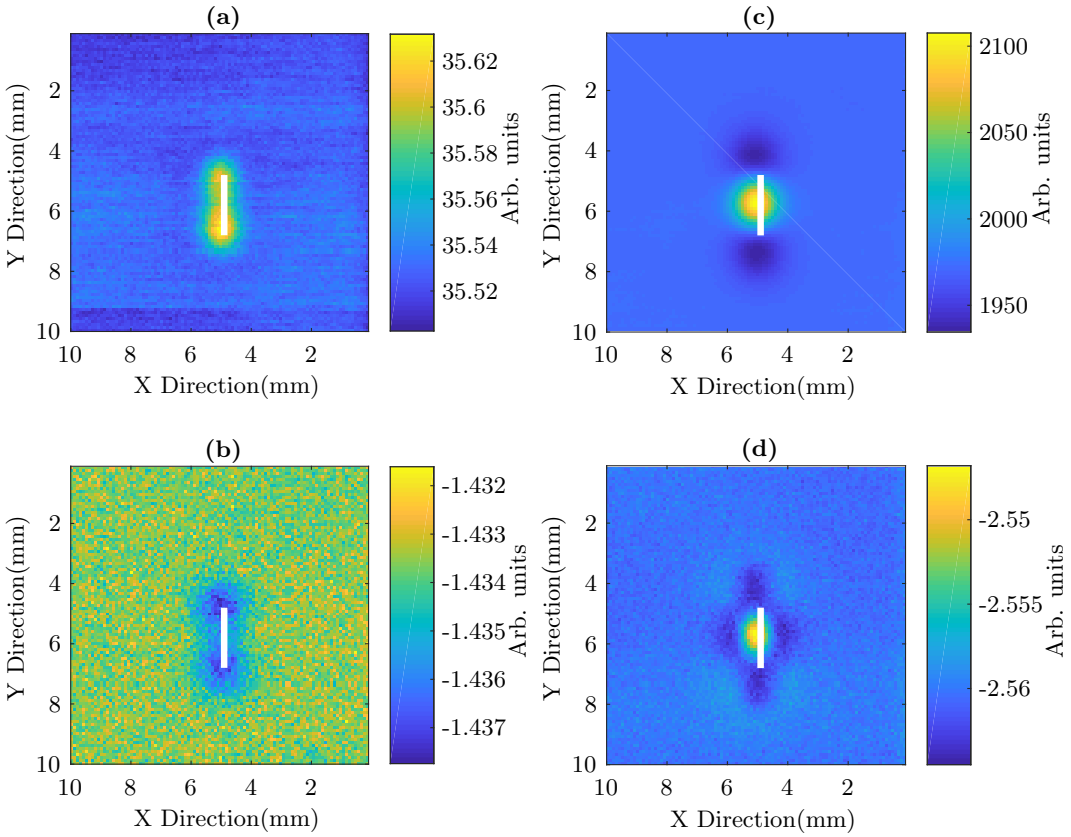

Figure 4.8: C-scans generated by measuring the voltage (a) amplitude across the transmit coil, (b) phase across the transmit coil, (c) amplitude across the receive coil, and (d) phase across the receive coil. The transmit coil was driven by a 50 mA sinusoidal current at 300 kHz. The white bars represent the length, and location of the 2 mm long defect on the stainless steel sample.

4.2.2 Data Filtering

Scanning the sample is done by moving the probe in steps along the surface of the test piece using the X-Y stage. The size of the steps is dependent on the size of the defect being scanned, as a step size that is much larger than the defect might not reflect the defect in the resulting image. Figure 4.8 presents C-scans generated from the amplitude, and phase of the transmit, and receive coils after scanning a stainless steel plate with a 2 mm long defect, with current at 300 kHz.

The coils were moved 100 steps in each direction at 0.1 mm per step, to generate a 10 mm by 10 mm pixel gird of the sample surface. The data presented has had no filtering or noise reduction done, save for the averaging done on the oscilloscope. Figure 4.8 (a) and (b) are generated from the magnitude, and phase of the voltage across the transmit coil (absolute), while (c) and (d) are generated from

the magnitude, and phase of the voltage across the receive coil (transmit-receive). It is observed through the experiments and FE modelling that the transmit coil data serves to size defects larger than the coil diameter, and receive coil data serves to determine the location of the centre of the defect.

The signal to noise ratio (SNR) of each image is evaluated to quantify the amount of noise in the data. This is especially useful in automation, where a SNR above a certain threshold can confirm the presence of a defect in situations where a human inspector is not present. The SNR is calculated by applying eq. (4.4)[98] to sections of the image. Before the SNR is calculated however, it is important to normalise the data, to get a more accurate evaluation. This also enables better visualization, wherein pixel values that represent the defect are high, and pixel values for the defect free areas of the sample are low. Normalisation is done by taking a line of the scan with the smallest standard deviation, to represent a section of the sample where no defect is present, taking the average of the pixel values on that line, and subtracting the value from all the other pixel values in the image. This sets pixel values for areas of the sample without defects to zero. Part of the normalization process is also taking the absolute of all the pixel values, so they are all positive.

$$\mathrm{SNR(dB)} = 20 \log \frac{\text{net signal}}{\text{backround noise}} \tag{4.4}$$

The background noise defined is the mean standard deviation of pixel values in a section of the image where no defect signal is expected, and the net signal is defined as an average of the pixel intensities in any section of the image which is above a defined intensity threshold. The section of the image has to have connected pixels, which have all external boundary pixels with an equal or lower value. First, the pixels in the image with intensities less than the defined threshold are suppressed, and set to zero, then the image is binarised, with regional maxima, which are connected neighbouring pixels representing the defect indication[99, 100] , set to 1. The other pixels are set to 0. This is a form of morphological image processing[101]. The indices for pixels set to one are collected, and the corresponding pixel intensities in the original image are averaged to get the net signal. Evaluating the net signal in this manner ensures that only clusters of pixels above the defined threshold are considered. A disadvantage of measuring the net signal in this manner however, is that a noisy image with random high intensity pixels will have those pixels included in the signal area. The solution is to apply a median filter to the image, which smooths out any random noise pixels . An example of the image sections taken for the SNR measurements is presented in fig. 4.9. Here, a median filter has been applied to

the images, and then the images have been binarised, setting regional maxima with values higher than 5 times the standard deviation of the image to 1, and the others to 0. In calculating the SNR, the threshold defined for the signal area selection affects the calculated value for the SNR, especially in the receive coil images, where the indication corresponding to the centre of the defect has a higher intensity than the edges. Hence, unless stated otherwise, the threshold for measuring SNR in this thesis is 5 times the standard deviation of the image.

Figure 4.10 re-plots the normalised image for the scan data presented in fig. 4.8. The transmit coil data images fig. 4.10 (a) and (b), have SNRs of 59.23 dB and 39 dB respectively, while the images for the receive coil measurements, fig. 4.10(c) and (d), have SNRs of 119.79 dB, and 66.17 dB respectively.

The data presented in fig. 4.10 shows a high SNR in the receive coil voltage fig. 4.10(c) and (d), compared the transmit coil voltage fig. 4.10(a) and (b). This is attributed to random noise introduced into the data as a result of backlash as the X-Y stage scans, and the accuracy of the scope time base measurement, which affects the phase data. The receive coil also tends to have a higher relative amplitude when on a defect, compared to when it is not on a defect. The median filter[102, 103, 104] performs better than a 2D Butterworth low pass filter[105, 106], weighted moving average filter[107, 108], and Gaussian filter[109, 110], in removing random high frequency noise spikes, as it uses an actual pixel value from the image, to replace the noise spikes, which preserves the magnitude of the defect indications within the image, while having a less blurring effect on the edges of the indications. This is particularly useful in data where the pixel value of random noise spikes is much higher than that of the actual data. Figure 4.11 presents the C-scan from fig. 4.10 filtered with a median filter. The improvement in the data is visible when the plots are compared, and the new calculated SNRs for the images show an increase in all cases. This method for calculating SNR requires that the magnitude of the pixel values representing a defect indication be high enough to meet whatever signal area threshold is defined.

A low threshold means that more of the pixel values in the defect indication will be used in the SNR calculation, and in cases like for the receive coil data fig. 4.11(c) and (d), where the pixel values at the centre of the defect are much higher than those at the defect edges, the calculated SNR values will be lower. This is not a disadvantage, and a major advantage of using a lower threshold, is that cases where the pixel values for the defect indication are not very high compared with the values for sections of the defect free sample, the defect is still detected in the SNR calculation. Too high of a threshold might lead to the probe missing

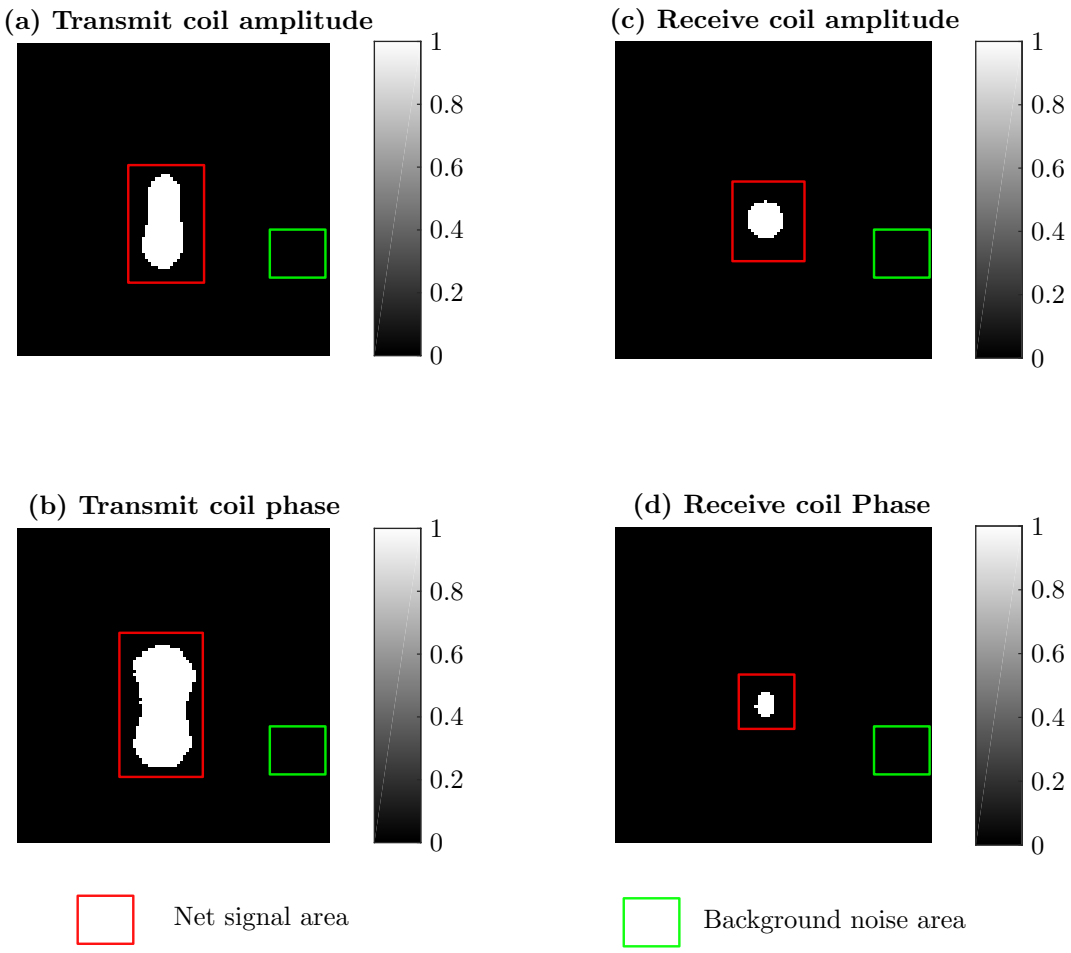

Figure 4.9: The image sections used in the calculation of SNR. The net signal area consists of pixels with values higher than 5 times the standard deviation of the image. The background noise area is an area of the image where no defect indication in expected. The images have been binarised, and pixels to be collected for evaluating the net signal have been set to 1, while the others have been set to 0. A median filter has also been applied to the images to smooth out random noise pixels.

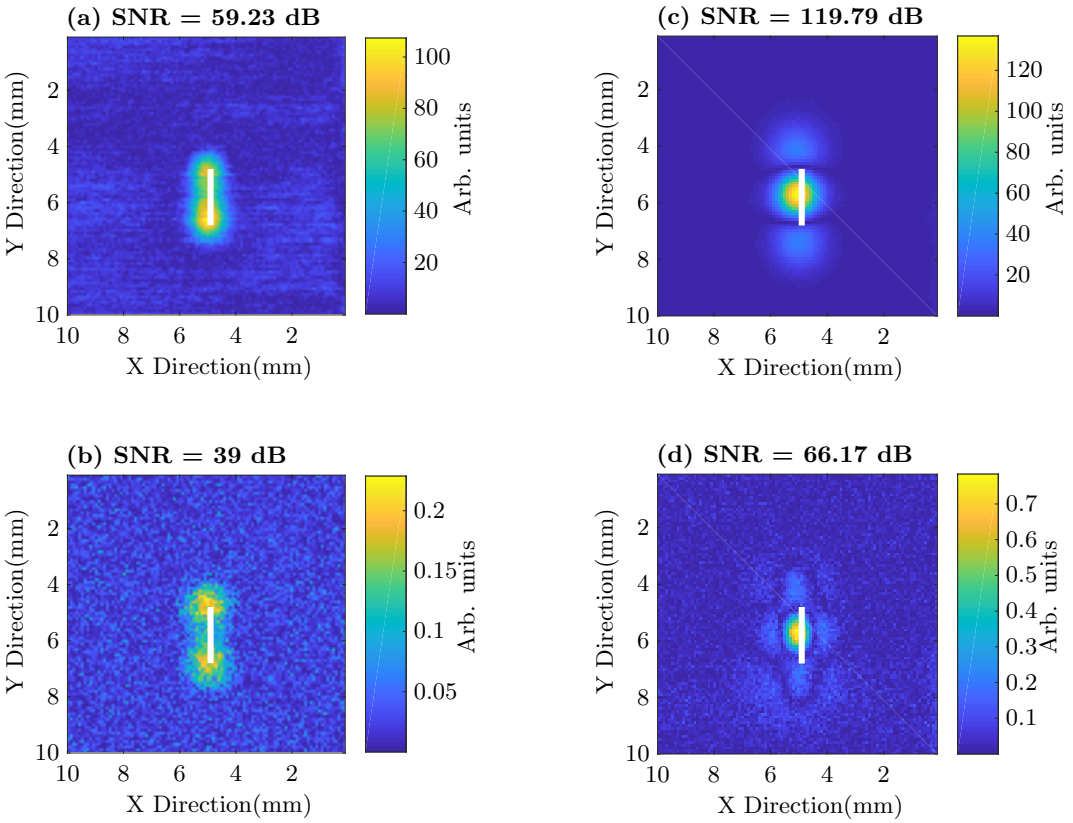

Figure 4.10: Normalised versions of the C-scans presented in fig. 4.8. (a) Amplitude across the transmit coil, (b) phase across the transmit coil, (c) amplitude across the receive coil, and (d) phase across the receive coil. The SNR in the transmit coil amplitude plot is 59.23 dB, and 39 dB in the phase plot, while for the receive coil, the SNR for the amplitude plot is 119.79 dB, and 66.17 dB in the phase plot. The white bar represents the size, and location of the 2 mm long defect on the stainless steel sample.

C-scan image	SNR - Image area 9 × SD (dB)	SNR - Image area 5 × SD (dB)
Transmit coil amplitude	No signal	69.8
Transmit coil phase	No signal	65.2
Receive coil amplitude	118.22	127.13
Receive coil phase	77.62	82.32

Table 4.3: Comparison of the SNR and defect detection when the signal area is defined as a low threshold, 5 times the standard deviation, and a high threshold, 9 times the standard deviation, for the median filtered images in fig. 4.11. The table shows that too high of a threshold might cause a defect to be missed entirely.

defects, and too low of a threshold might lead to false positives. Table 4.3 presents the SNR values of the amplitude, and phase images with the signal threshold set to 5, and 9 times the standard deviation of the images. The defects in the transmit coil images are missed when the SNR threshold is set too high, and the receive coil SNRs are higher, due to fewer pixels with higher intensities used for evaluating the net signal.

4.2.3 Data Combination

In improving the SNR of eddy current C-scan measurements, different approaches can be taken. Some authors consider frequency mixing, whereby eddy current probe measurements at multiple frequencies are combined in order to isolate various defect types, thereby increasing the SNR of a particular defect indication[82, 111], and pulsed eddy current imaging which has an extended penetration depth, and more information in the frequency domain, due to the utility of a frequency band for eddy current excitation[72, 112]. In most cases however, the authors tend to express the eddy current C-scan images as a measure of the in-phase and in-quadrature impedance values (real and imaginary components), or the amplitude and phase of the probe impedance (eqs. (4.1) and (4.2))[113, 60, 111, 114, 115]. In this thesis, images are generated using amplitude and phase of the voltages across both the transmit, and the receive coils, and as demonstrated in this section, the combination of all these images, result in a substantially improved SNR.

The images are combined by the way of multiplication. Presented in fig. 4.12, are the images resulting from multiplying the amplitude with the phase of the voltages across the coils. The magnitude and phase data are different, but both show indications of the defect, and have different noise content. Multiplying the data together serves to suppress the noise by destructively interfering the noise content from each data, while constructively superimposing the defect indications. This increases the overall amplitude of the defect indication, while decreasing the overall

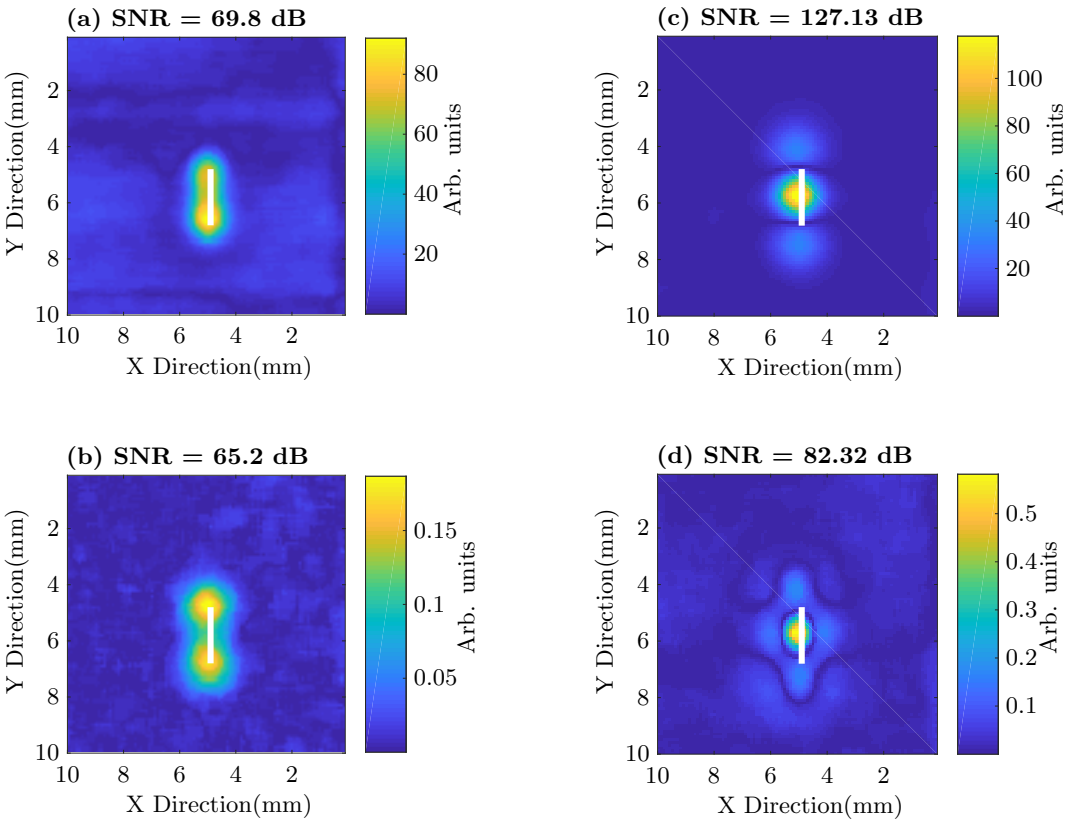

Figure 4.11: C-scan of a 2 mm long defect in stainless steel with a median filter applied. (a) Amplitude across the transmit coil, (b) phase across the transmit coil, (c) amplitude across the receive coil, and (d) phase across the receive coil. Application of a median filter leads to an increased SNR. The white bars represent the size, and location of the defect on the stainless steel sample.

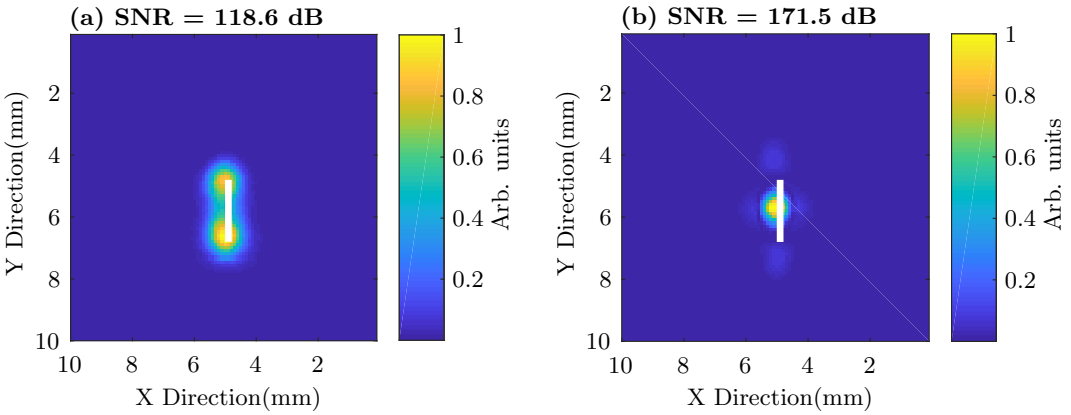

Figure 4.12: C-scan generated from multiplying the amplitude and phase images from the voltage across the (a) transmit coil, and (b) receive coil. The SNR for the combined transmit coil amplitude, and phase is 118.6 dB, and for the receive coil, 171.5 dB. The white bars represent the size, and location of the defect on the stainless steel sample.

noise content. This is a novel approach, which at the time of this writing has not been seen before. The improvement in SNR for both transmit coil, and receive coil images are visible, and are indicated in the calculated SNR values. What this shows, is that the combination of amplitude, and phase data increases the magnitude of the defect indication, while decreasing the standard deviation of the background noise. Hence, if required, a stricter threshold can be defined and the defect is still detected. As demonstrated in section 5.3, the transmit coil data is shifted spatially with respect to the receive coil data, and compensating for this shift, the transmit coil image can be also be combined with the receive coil image to further increase the SNR. This combined image is presented in fig. 4.13, with a SNR of 265.65 dB. Combining the data in this manner leads to a significant improvement in SNR, and an improved indication of the defect. A comparison of the SNRs as the images are combined, is presented in table 4.4, with the signal area threshold defined as 9 times the image standard deviation.

The C-scans presented thus far have high SNRs as a result of the high specification equipment such as the oscilloscope with low intrinsic time jitter, and careful steps used in collecting the data. Inspections in the field may yield noisier images, which could possibly be attributed to complex shaped samples, or issues with sensor delivery. Figure 4.14 presents the original C-scans, made noisier by convolving them with a zero mean Gaussian noise matrix with a standard deviation of 0.1. These images have significantly degraded SNRs with no filtering applied, and even at a signal area threshold of 5 times the image standard deviation, the defects are not

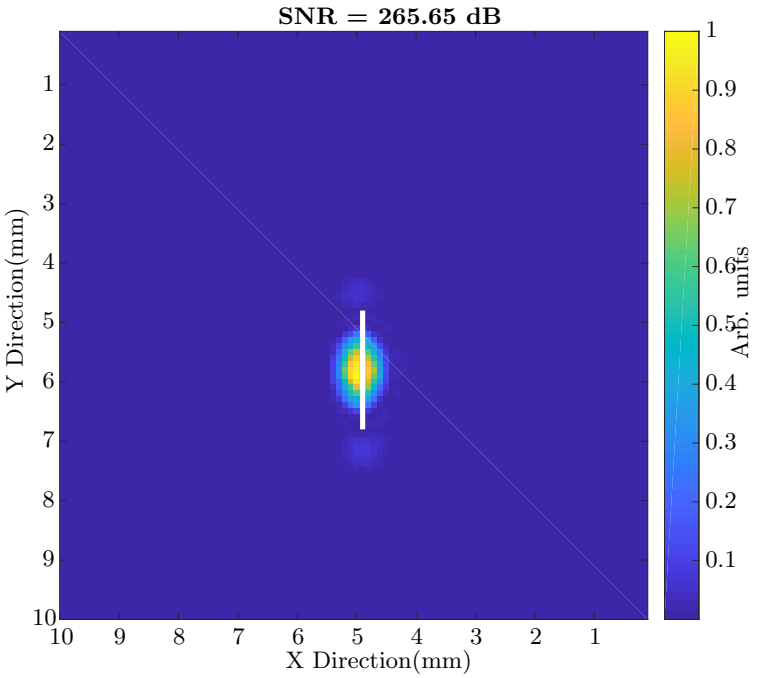

Figure 4.13: C-scan resulting from the combination of the transmit coil images with the receive coil images. The resulting SNR is substantially higher at 265.65 dB, with a clear defect indication. The white bar represents the size, and location of the defect on the stainless steel sample.

Coil	Amplitude (dB)	Phase (dB)	Combined A & P (dB)	Combined T & R (dB)
Transmit coil	No signal	No signal	108.6	260.39
Receive coil	131.13	86.69	168.24	

Table 4.4: Comparison of the SNRs for the images before combination, with amplitude and phase multiplied, and with transmit coil, and receive coil voltages multiplied. The SNRs are calculated with the signal area defined as pixel values higher than 9 $\times$ the standard deviation of the image. With this criterion, the defect indication is not high enough in the transmit coil images, but after combination of amplitude with phase, the defect indication meets the threshold.

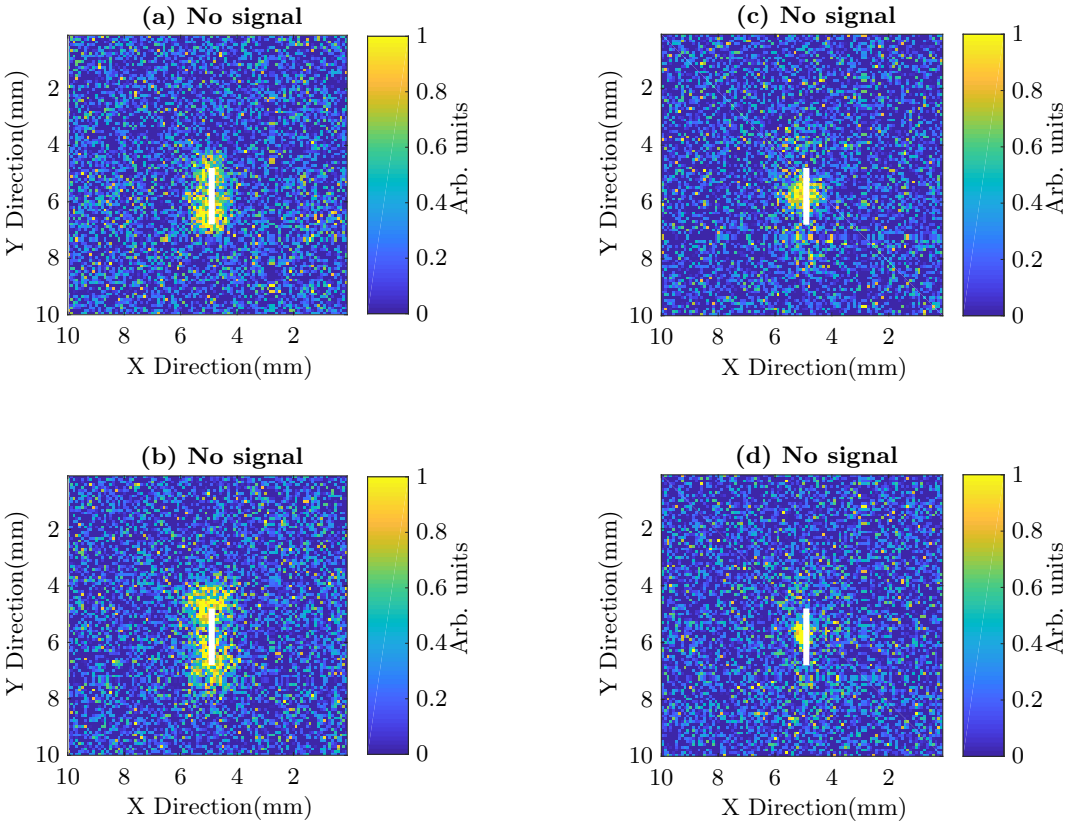

Figure 4.14: The original C-scans with a zero mean Gaussian noise matrix applied. The Gaussian distribution has a standard deviation of 0.1. The images have significantly degraded SNRs, and at a signal area threshold of 5 times the standard deviation of the image, the defect is not detected. The white bars represent the size, and location of the defect on the stainless steel sample.

detected. This was done to demonstrate the advantage of combining the amplitude, with phase data, and absolute with transmit receive where available. Presented in fig. 4.15 are the images resulting from combining the amplitude with phase C-scans for the voltage across the coils. Using the same criterion for measuring the signal, the defects are detected, albeit with poor SNRs. The SNRs are considerably lower when compared with the scans in fig. 4.12, however this is to be expected as the images combined are more noisy. Furthermore, in situations as these where the voltage across both transmit and receive coils are available, combining the data further increases the the SNR as demonstrated in fig. 4.16. While the SNR is lower than for the image in fig. 4.13, the SNR for the image in fig. 4.16 is substantially higher than those for the individual transmit and receive coil images in fig. 4.15.

Attempting to recover the noisy images through the application of a median filter, it can be observed that while the SNRs of the individual amplitude and phase

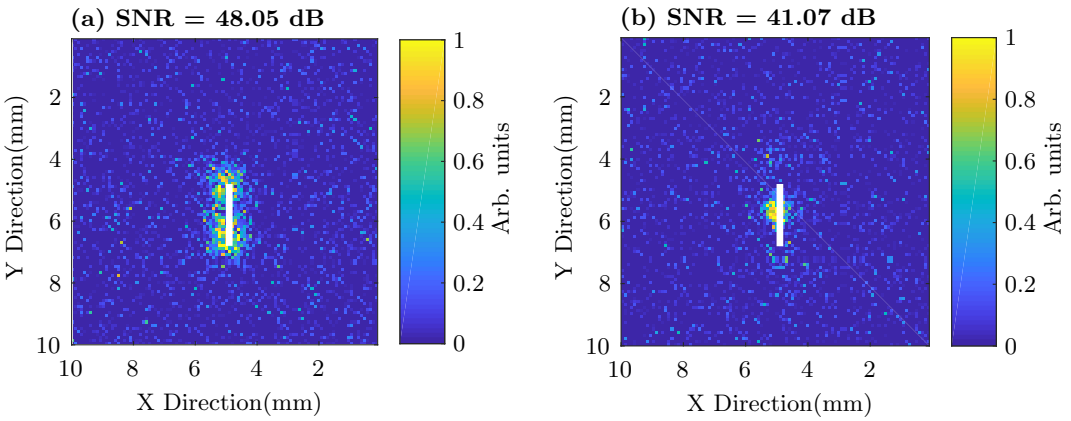

Figure 4.15: C-scans resulting from combining the amplitude and phase images generated from the voltage across (a) the transmit coil, and (b) the receive coil; with Gaussian noise applied. The SNRs are calculated with the signal area threshold defined as 5 times the standard deviation of the image. While not detected in the individual amplitude and phase C-scans, the defect is detected in both the absolute, and transmit receive C-scans after amplitude, and phase combination. The white bars represent the size, and location of the defect on the stainless steel sample.

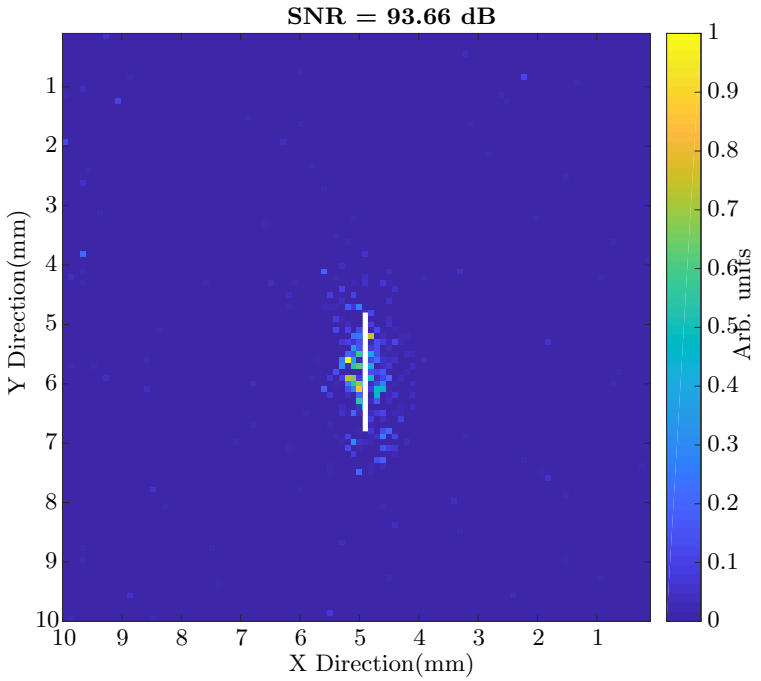

Figure 4.16: C-scan resulting from the combination of the transmit coil images with the receive coil images with Gaussian noise applied. The resulting SNR, while lower than the less noisy data is still a substantial improvement over the individual transmit, and receive coil images. The white bar represents the size, and location of the defect on the stainless steel sample.

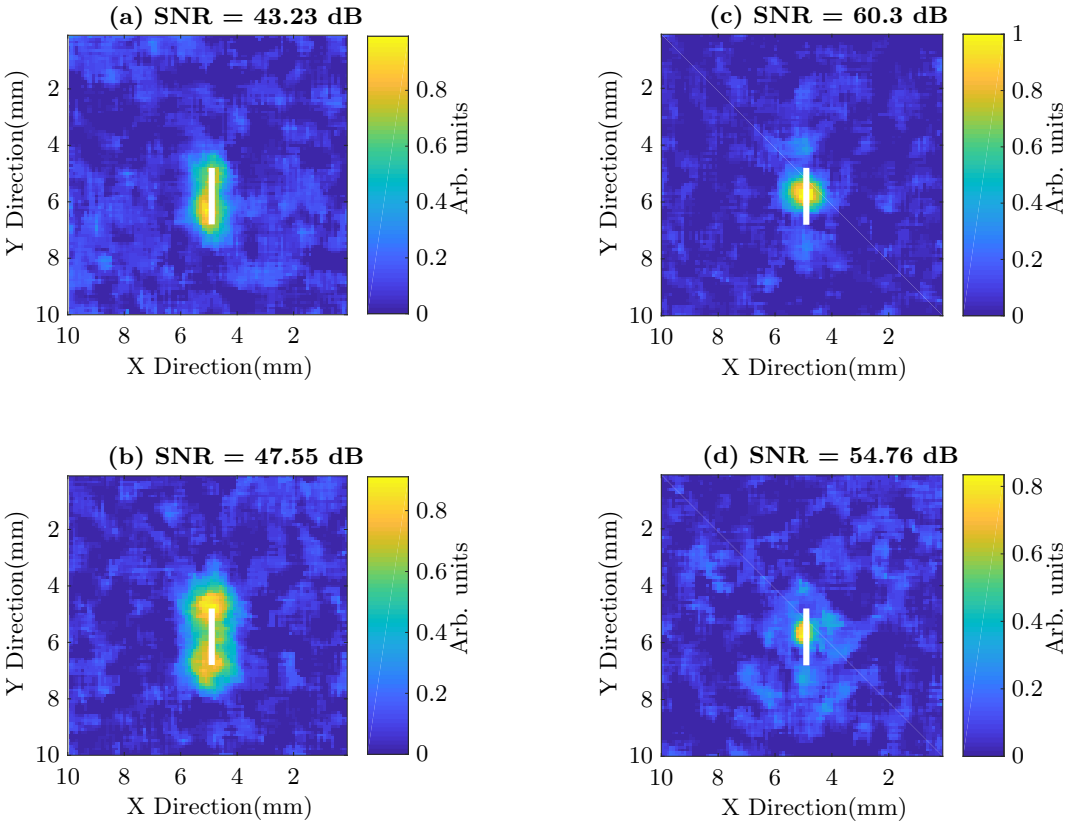

Figure 4.17: The C-scans with Gaussian noise with a standard deviation of 0.1, and a median filter applied. The images have significantly degraded SNRs, however, at a signal area threshold of 5 times the standard deviation of the image, the defects are detected. The white bars represent the size, and location of the defect on the stainless steel sample.

images are improved, and the defect signals high enough for a SNR calculation fig. 4.17, they are not as high as the originals in fig. 4.11. In addition, the defect indications are much less sharp. The combined amplitude, and phase images fig. 4.18 show a clearer defect indication with an improved SNR. It can also be observed that the defect indications are not as sharp as those in fig. 4.12. Although in this case, the recovered images fare better than those in fig. 4.17. The combined absolute, and transmit receive image, fig. 4.19 can be said to fare the best in terms of SNR. However, the indication is also not as good as the original image in fig. 4.13.

There is a limit however to the amount of noise from which the signal can be recovered through data combination. Figures 4.20 to 4.22 present the images with a zero mean Gaussian noise matrix applied, with a standard deviation of 1. In all the images, the signal strength is not high enough above the image standard deviation to register a SNR. In fig. 4.22 a SNR is calculated, however this is inaccurate, as it

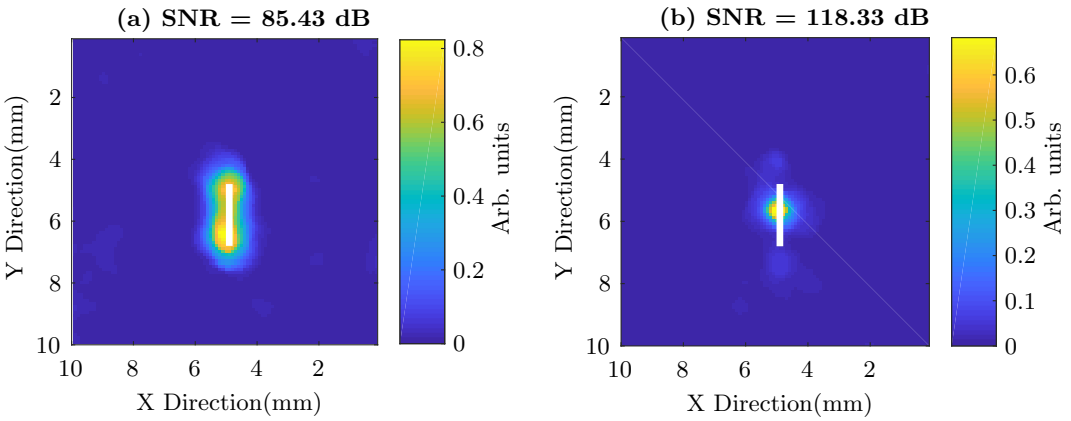

Figure 4.18: C-scans resulting from combining the amplitude and phase images generated from the voltage across (a) the transmit coil, and (b) the receive coil; with Gaussian noise and a median filter applied. The SNRs are calculated with the signal area threshold defined as 5 times the standard deviation of the image. The combined data results in a better SNR compared to the individual C-scans, although the defect indication is less sharp. The white bars represent the size, and location of the defect on the stainless steel sample.

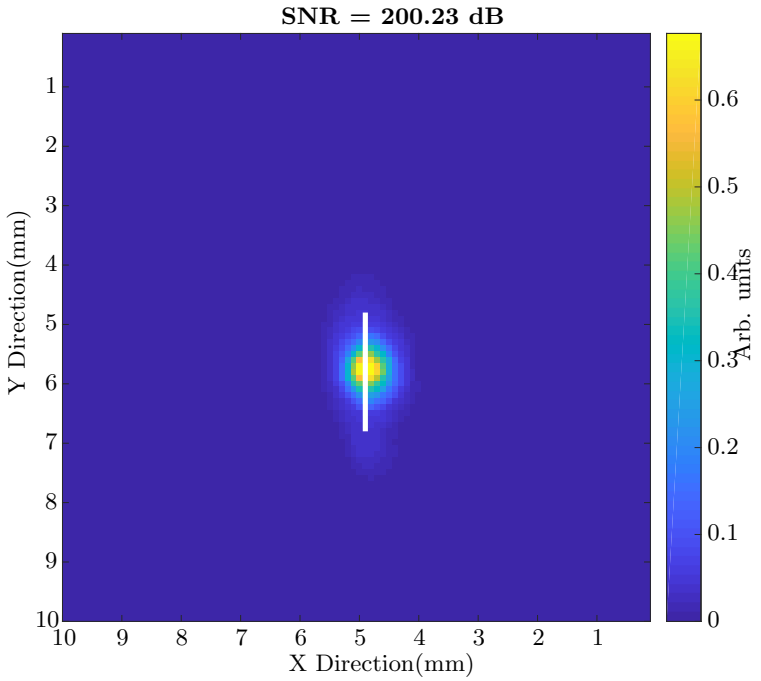

Figure 4.19: C-scan resulting from the combination of the transmit coil images with the receive coil images with Gaussian noise and a median filter applied. The resulting SNR, while lower than the less noisy data is still a substantial improvement over the individual transmit, and receive coil images. The white bar represents the size, and location of the defect on the stainless steel sample.

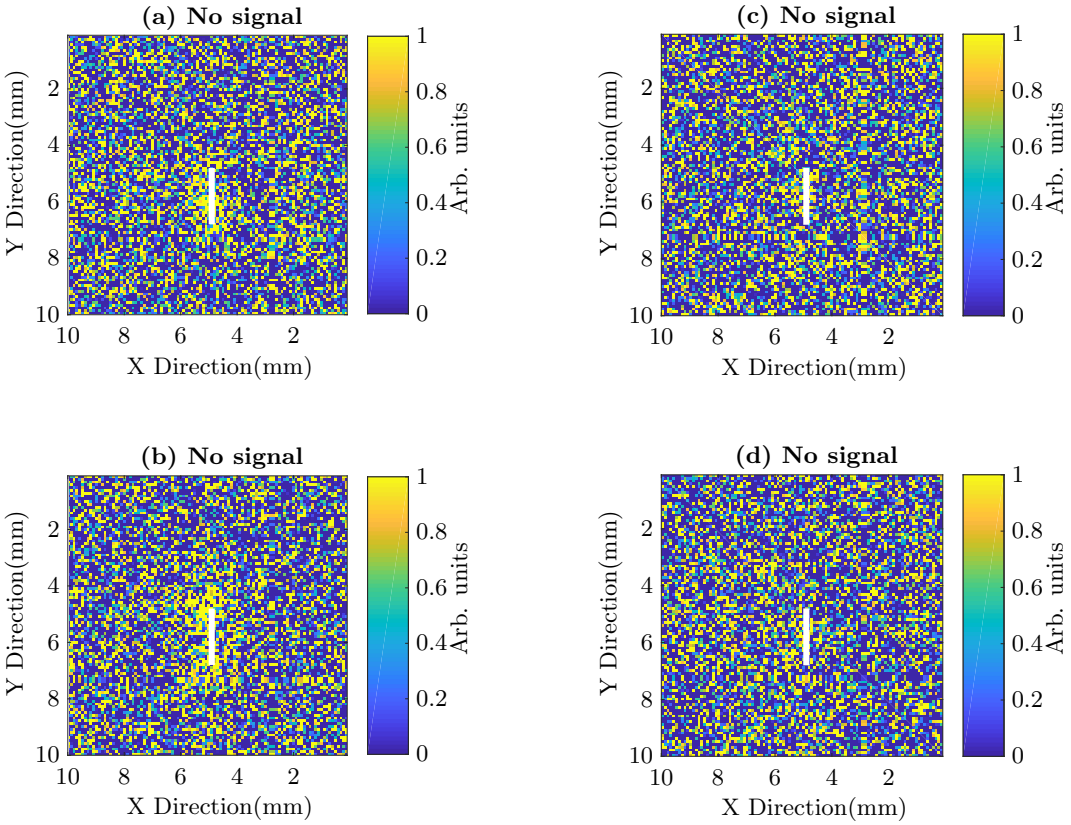

Figure 4.20: The original C-scans with a zero mean Gaussian noise matrix applied. The Gaussian distribution has a standard deviation of 1. The images have significantly degraded SNRs, and at a signal area threshold of 5 times the standard deviation of the image, the defect is not detected. Visually, the defect is indiscernible from the images. The white bars represent the size, and location of the defect on the stainless steel sample.

uses random noise pixels which register as regional maxima for the calculations.

Applying a median filter to these images, the results are shown in figs. 4.23 to 4.25. From fig. 4.23 the defects in the C-scans are barely discernible, and the images have very low SNRs. The combined amplitude, and phase plots in fig. 4.24 have better SNR values, however, the defect indications are blurred and much less accurate. The combined absolute, and transmit receive image, fig. 4.25 also shows the defect indication, at the correct location, but the shape of the indication has been degraded. It can also be observed that in recovering defect signal after combining noisy images, the receive coil C-scans tend to come out worse then the transmit coil C-scans. This can be attributed to the defect indications in these images having a smaller area, and so while the pixel intensities for the defect indication are high, the pixel area is small, hence filtering has a more degrading effect.

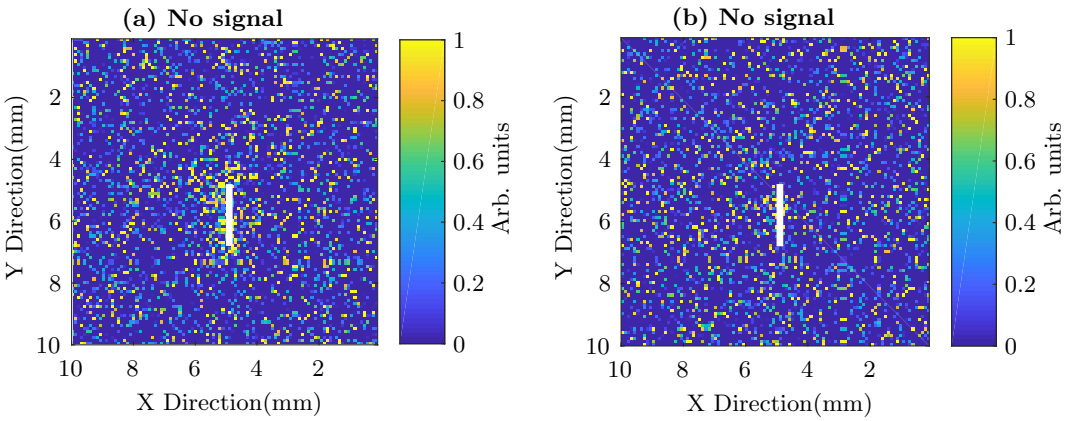

Figure 4.21: C-scans resulting from combining the amplitude and phase images generated from the voltage across (a) the transmit coil, and (b) the receive coil; with Gaussian noise applied. The SNRs are calculated with the signal area threshold defined as 5 times the standard deviation of the image. At such a high noise level the defect is not detected even after combining amplitude with phase data on the stainless steel sample.

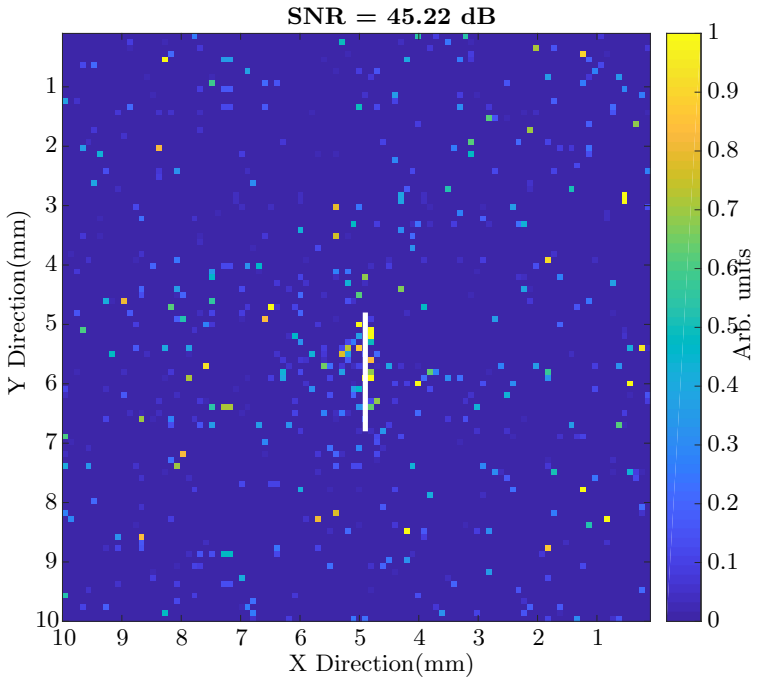

Figure 4.22: C-scan resulting from the combination of the transmit coil images with the receive coil images with Gaussian noise applied. The SNR calculated is inaccurate due to random noise pixels being recognised as regional maxima. Hence it is concluded that the defect in not detected in this image. The white bar represents the size, and location of the defect on the stainless steel sample.

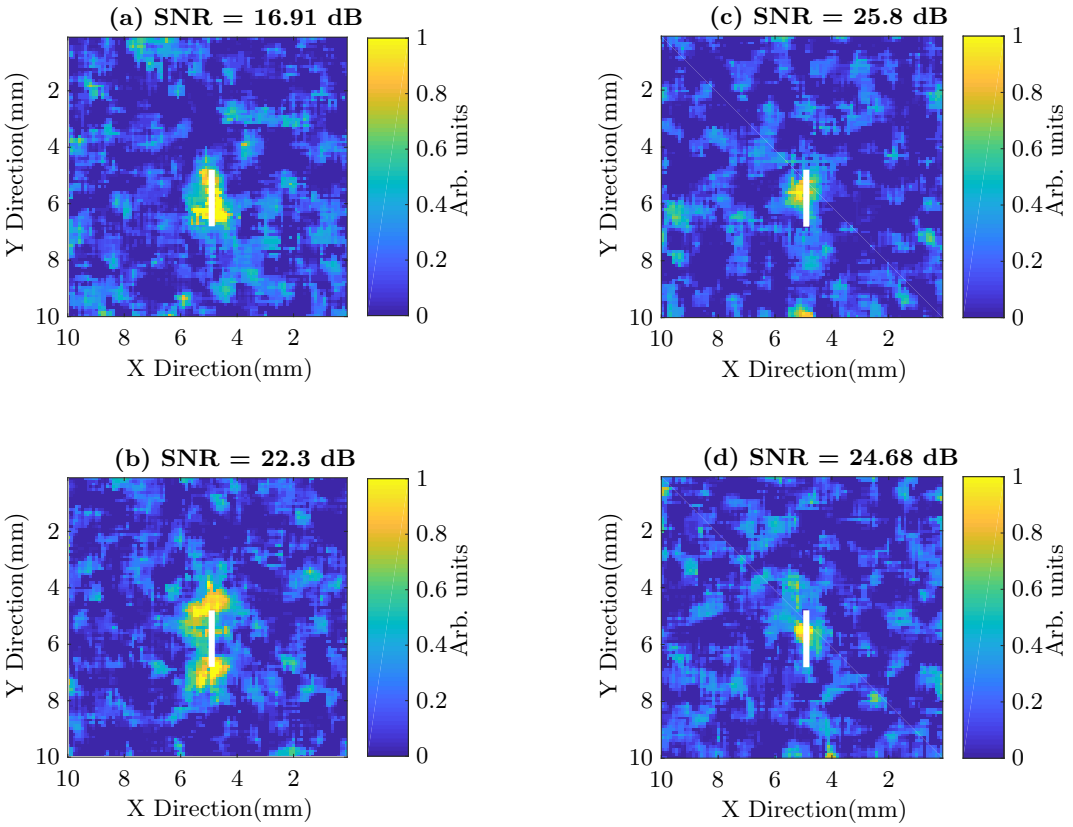

Figure 4.23: The C-scans with Gaussian noise with a standard deviation of 1, and a median filter applied. Depending on the application, the defect signals can be said to have been recovered. However, the SNR values are very low, hence the scans are deemed unusable in this form.

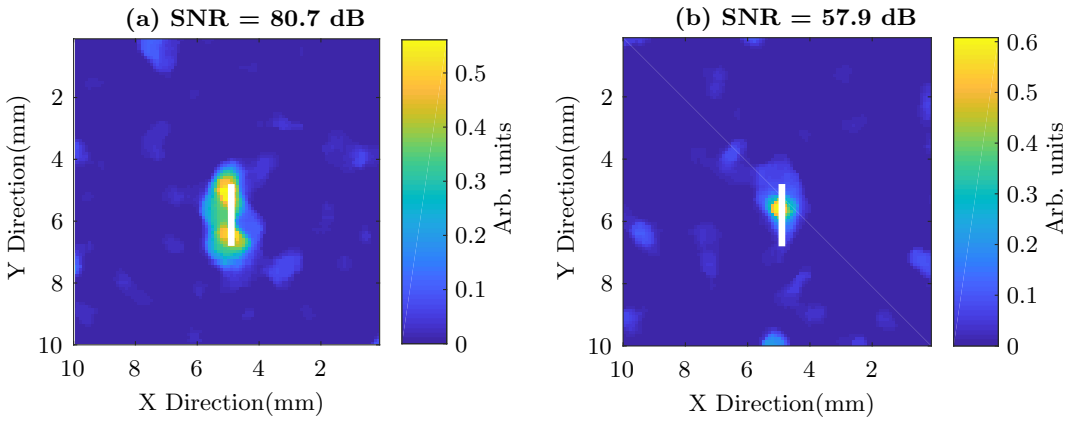

Figure 4.24: C-scans resulting from combining the amplitude and phase images generated from the voltage across (a) the transmit coil, and (b) the receive coil; with Gaussian noise of with a standard deviation of 1, and a median filter applied. The SNRs are calculated with the signal area threshold defined as 5 times the standard deviation of the image. While the calculated SNRs are higher than the individual scans, the defect indication is blurred, and less accurate.

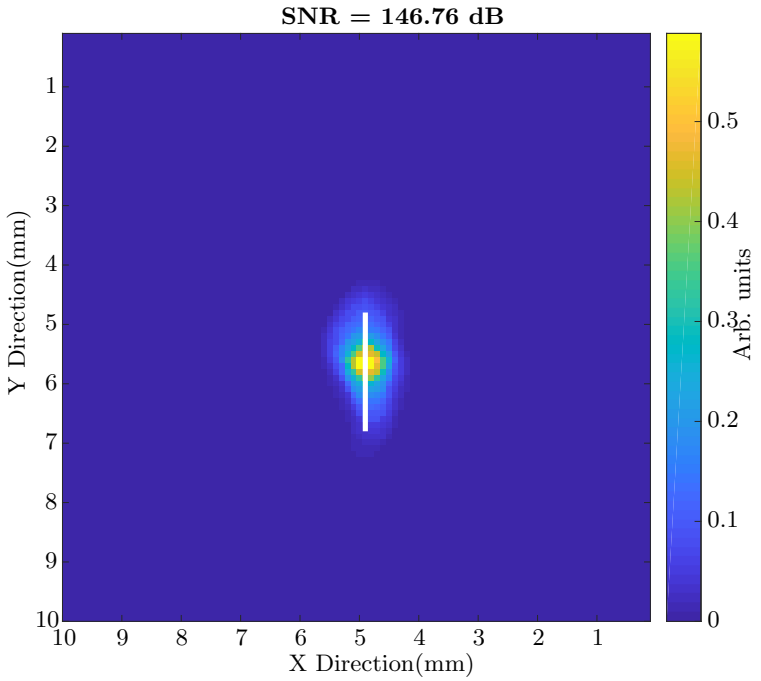

Figure 4.25: C-scan resulting from the combination of the transmit coil images with the receive coil images with Gaussian noise with a standard deviation of 1, and a median filter applied. The resulting SNR is higher than the individual scans, and the defect indication can be considered usable. While it is not as accurate as less noisy data, it still clearly visually identifies the presence of the defect.

	SD = 0		SD = 0.01		SD = 0.1		SD = 1	
	TC	RC	TC	RC	TC	RC	TC	RC
Magnitude	70	127	63	72	43	60	17	26
Phase	65	82	65	73	48	55	22	25
Combined A&P	119	172	117	137	85	118	81	58
Combined T&R	266		241		215		147	

Table 4.5: Comparison of the SNRs in dB for the images before combination, with amplitude and phase combined, and with transmit coil, and receive coil voltages combined. Gaussian noise matrices with increasing intensities, denoted by the standard deviation (SD) are applied to the images. The images have been filtered before the SNR calculation. The degradation of SNR even after data combination can be observed from the values in the table.

Table 4.5 presents a comparison of the SNR for the C-scans as Gaussian noise matrices with ascending standard deviations are applied. A median filter is applied to the scans after the noise convolution, and the SNRs are calculated for a signal area threshold higher than 5 times the standard deviation of the image. The table shows that as more intense noise is applied, it becomes more difficult to recover the image after combining and applying a median filter reflected in the decreasing SNR after combination. While the SNRs of the images remain relatively high after combination, the defect indications become less sharp as observed from the images, hence the limit at which the combination of data as demonstrated is applicable, depends on the application.

4.3 Summary

This chapter presents the steps taken in generating C-scan images of a 2 mm long notch in a stainless steel plate. The equipment used in collecting this data was specified, and the methods and justification for the form in which the data is presented were addressed. The methods of processing the data and calculating the signal to noise ratio (SNR) of the C-scan images were also presented.

It is demonstrated that a pair of coils driven at 300 kHz using a constant current source, and an oscilloscope with low intrinsic time jitter for voltage measurements can accurately detect defects as small as 0.25 mm in low conductivity materials such as stainless steel. Current EC systems in the market require a much higher excitation frequency to detect defects of this size in these materials, and current ECA systems are not used for high frequency inspections (> 2 MHz), due to the complex electronics required. The experiments presented show that it is possible

to optimise ECAs for inspecting low conductivity materials at sub MHz frequencies, thus reducing the need for short wires and complex electronics.

This chapter demonstrated how the combination of voltage amplitude, with the phase results in an image with a higher signal to noise ratio (SNR) when compared to the individual images. In situations where both the voltage across the transmit, and receive coils are measured, combining the data results in an image with a much higher SNR. For these experiments, the SNR calculations, and thresholds set were used as a means to determine if a defect was properly detected; useful especially in situations where a human operator is not present. These SNR calculations, in addition to setting high or low signal area thresholds, can be used to ascertain the presence of a defect in C-scans. A high SNR value calculated using a high signal area threshold confirms the presence of a defect, but can lead to false negatives, and a low signal area threshold might lead to false positives if the data is noisy. images. This novel approach to eddy current imaging has not been presented anywhere else, and shows potential in improving the detection rate of very small defects in low conductivity materials, which are known to be difficult to inspect.

The versatility of the method was demonstrated by convolving the data with Gaussian noise matrices with increasing values of standard deviation. While the SNRs remained high with data combination and filtering, the defect indications degraded, hence it is concluded that the limit to which data combination is applicable, is dependent on the particular use for the data. If the objective is to confirm the presence of a defect, then the method can be applied to very noisy data with potentially serviceable results achieved. However if the objective is to size, and locate the defect, the method is best applied to less noisy data.

The results presented in this chapter are an in depth analysis of the method as applied to a low conductivity material such as stainless steel. Chapter 6 presents results from experiments conducted on other low conductivity materials - titanium, and titanium aluminide.

Chapter 5

Eddy Current Modelling

Modelling serves to facilitate a better understanding of the inner workings of the electromagnetic behaviour of eddy current probe coils, which are otherwise difficult to visualise. It is a valuable tool, which helps in interpreting signal responses for defect detection and characterisation[116, 117], performing model based probability of detection (PoD) studies for various eddy current sensors in realistic test conditions[118, 119], and performing studies to predict the behaviour of complex sensor configurations, which would otherwise be expensive to test experimentally[120, 121].

Analytical models comprise of mathematical equations with solutions, which can be used to analytically describe the changes in a system. Due to the complexity of field interactions in eddy current systems, the closed form solutions from analytical models tend to be applicable when assumptions are made to simplify the model. These assumptions include the isotropy, and homogeneity of the sample, the coil being of a simple shape, and air cored.

Many authors have presented analytical models, which describe the magnetic field and impedance of an eddy current coil interacting with an electrical conductor. Dodd and Deeds[122] derived equations for calculating the magnetic vector potential of an axially symmetric eddy current coil above a multi-layered conductive sample, and a coil encircling a multi-conductor rod. The calculated magnetic vector potential can then be used to evaluate physical phenomena such as the induced eddy currents, the induced voltage, and the coil impedance. Auld and Moulder[123] presented equations for calculating the impedance of an air cored eddy current probe interacting with a flaw in a test piece. Burke and Ibrahim[124] presented equations for analytically calculating the change in mutual impedance between two air cored eddy current probes, of various orientations in the presence of a conducting plate.

The equations presented enable the evaluation of the effects of probe lift-off, and sample conductivity variations on the coil mutual impedance. Analytical models are however limited in application. Realistic configurations such as the presence of a ferrite core in the coil, or sample edge effects on induced eddy currents cannot be reliably modelled analytically.

This chapter presents an analytical 2-D axi-symmetric model of a single-turn filament coil over a single layered aluminium conductor using the equations derived by Dodd and Deeds[122]. The coil is located 0.2 mm above the conductor, with a sinusoidal wave excitation current flowing through it. The current through the coil has an amplitude of 50 mA, at a frequency of 300 kHz. The analytical model is used to generate an image showing the distribution of induced eddy current in the aluminium test piece.

Finite element (FE) models are created for a more realistic description of the eddy current field interactions. A 2-D axi-symmetric FE model of a 10-turn solenoid coil above an aluminium sample is presented. The coil has a lift-off of 0.2 mm above the sample, and is excited by a 50 mA, 300 kHz alternating current. This model serves to visualise the distribution of eddy currents in the aluminium sample, and as a comparison with the analytical model.

The experiments presented in this thesis were preformed using EC coils with identical geometry. In this chapter, FE models are presented of this configuration to visualise the interaction between the coil pairs and the conductive sample. The models presented show line scan plots of the coils moving along the sample surface, showing the effect of defects on the coil impedance.

5.1 Analytical Modelling

An infinitely thin (filament) coil above a conducting half-space, illustrated in section 5.1, can be modelled using the analytical equations for the magnetic vector potential, $\mathbf{A}$, derived by Dodd and Deeds[122]. The magnetic vector potentials $\mathbf{A}_1(r,z)$, and $\mathbf{A}_2(r,z)$, at a radial position, r, and depth, z, for the layered conductive regions can be calculated as:

$$\begin{aligned}\mathbf{A}_1(r,z) = \mu_1 I r_0 \int_0^\infty & J_1(\alpha r_0) J_1(\alpha r) \exp(-\alpha l)\alpha \\ & \times \left[\frac{(\alpha_1+\alpha_2)\exp(2\alpha_1 c)\exp(\alpha_1 z) + (\alpha_1-\alpha_2)\exp(-\alpha z)}{(\alpha-\alpha_2)(\alpha_1-\alpha_2) + (\alpha+\alpha_1)(\alpha_1+\alpha_2)\exp(2\alpha_1 c)} \right] d\alpha,\end{aligned} \tag{5.1}$$

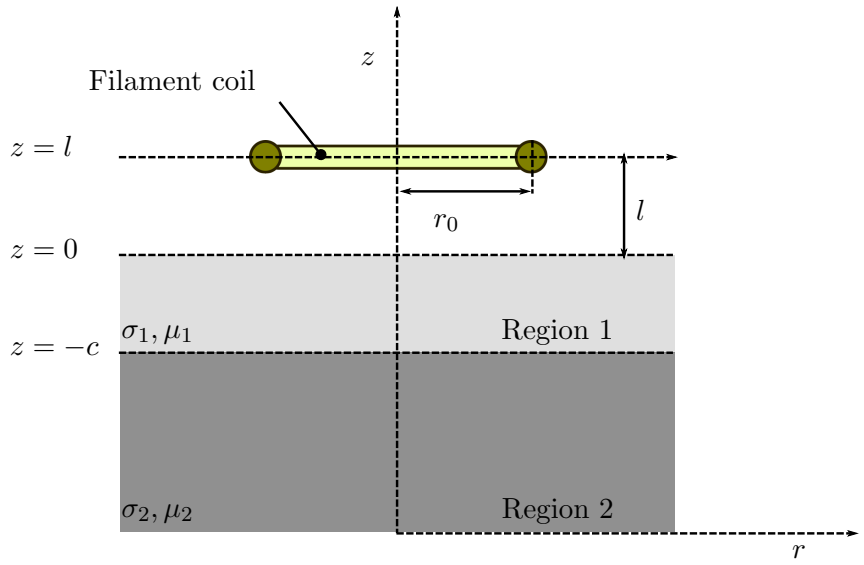

Figure 5.1: Illustration of the filament coil over a two layered conducting half-space, showing the parameters used to calculate the Dodd and Deeds analytical model. The coil with a radius, r, is located at a height, l, above the conductor. The layered conductor has two conducting regions with different, or the same effective conductivities, σ_i, and permeabilities, μ_i, and the top layer has a depth, c. The model is axi-symmetric. After [122] .

$$\begin{aligned}\mathbf{A}_2(r,z) = \mu_2 I r_0 \int_0^\infty & J_1(\alpha r_0) J_1(\alpha r) \exp(-\alpha l)\alpha \\ & \times \left[\frac{2\alpha_1 \exp(c(\alpha_2+\alpha_1))\exp(2\alpha_2 z)}{(\alpha-\alpha_2)(\alpha_1-\alpha_2)+(\alpha+\alpha_1)(\alpha_1+\alpha_2)\exp(2\alpha_1 c)}\right] d\alpha,\end{aligned} \tag{5.2}$$

where, J_1, is a Bessel function of the first kind, I, the alternating current through the coil, r_0, the coil radius, l, the coil height above the surface of the conductive half-space, and c, the thickness of Region 1. The term α is a continuous variable defined by Dodd and Deeds as the separation constant, and α_i is defined as,

$$\alpha_i = \sqrt{\alpha^2 + j\omega\mu_i\sigma_i}. \tag{5.3}$$

The conductive regions 1 and 2 have characteristic conductivities and permeabilities, σ_i and μ, where i represents the region number. The current density, $\mathbf{J}$, in the material can therefore be calculated as[122],

$$\mathbf{J} = -j\omega\sigma\mathbf{A} \tag{5.4}$$

Figure 5.2 shows the current density in a single layered aluminium sample calculated using eqs. (5.1) and (5.2). An alternating current with an amplitude of

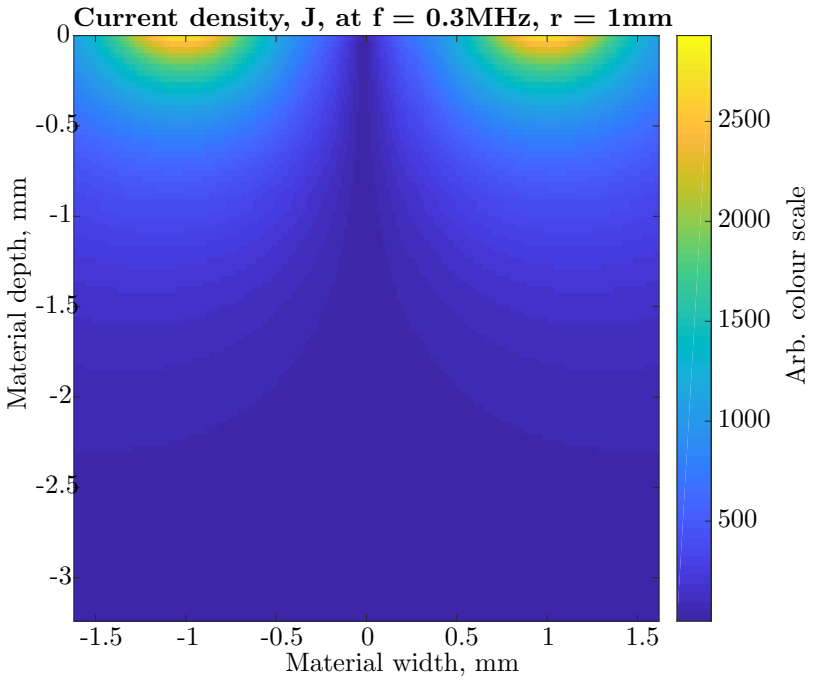

Figure 5.2: Model of a 2 mm wide filament coil, driven at 300kHz, 0.2 mm above an aluminium sample. The current density distribution within the sample is calculated using the equations set out by Dodd and Deeds[122]. The model was calculated using MATLAB.

50mA, and frequency of 300kHz, is flowing the coil of radius 1 mm, located 0.2 mm above the surface of the sample. This model was created using the computation software, MATLAB. The model axi-symmetry enables the calculation of current density in one half of the model, which is then mirrored to produce a full 2-D image. Pixel grids are generated with positions corresponding to the (r, z) values in eqs. (5.1) and (5.2), and the value for current density at each pixel location is calculated.

Equations to calculate the magnetic vector potential due to a finite width coil were also defined by Dodd and Deeds, and an expression for calculating the impedance of a coil in air, and above a conducting half space is given as[122],

$$
\begin{aligned}
Z = \frac{j\omega\pi\mu n^2}{(l_2-l_1)^2(r_2-r_1)^2}\int_0^\infty \frac{1}{\alpha^5} I^2 \Bigg(& 2(l_2-l_1) \\
& + \alpha^{-1}\Bigg\{ 2\mathrm{e}^{[-\alpha(l_2-l_1)]} - 2 + \left[\mathrm{e}^{(-2\alpha l_2)} + \mathrm{e}^{(-2\alpha l_1)} - 2\mathrm{e}^{-\alpha(l_2+l_1)}\right] \\
& \times \left[\frac{(\alpha+\alpha_1)(\alpha_1-\alpha_2)+(\alpha-\alpha_1)(\alpha_2+\alpha_1)\mathrm{e}^{(2\alpha_1 c)}}{(\alpha-\alpha_1)(\alpha_1-\alpha_2)+(\alpha+\alpha_1)(\alpha_2+\alpha_1)\mathrm{e}^{(2\alpha_1 c)}}\right]\Bigg\}\Bigg) d\alpha
\end{aligned}
\tag{5.5}
$$

where, r_1 and r_2 are the internal, and external radius of the coil, and l_1, and l_2 are the bottom and top of the coil in the z plane.

5.2 Finite Element Modelling

The finite element method is a numerical technique for solving the field equations of a body, and in the context of electromagnetism, this method is used to calculate the potentials at any (or all) locations of a body in which a magnetic or electric field is applied. Cases where exact solutions to electromagnetic problems can be found analytically using Maxwell's equations are few, hence the need for numerical methods like the finite element method to find approximate solutions to the problems[125]. The problem domain is divided into multiple sub domains, resulting in the complicated structure being modelled as an assembly of a large number of simple pieces, as illustrated in fig. 5.3, where the model is divided into a number of triangular elements. Interpolation functions are used to calculate the field at any point within the domain bounded by the element. The linear interpolation function for a triangular element is expressed as[126],

$$f(x,y) = \sum_{i=1}^{3} N_i(x,y) f_i, \tag{5.6}$$

where, f_i are the values of $f(x,y)$ at the nodes of the element denoted by i, and $N_i(x,y)$ are named shaped functions for the triangular element[127].

The $A, V-A$ formulation[125, 128] is used to calculate the fields within the finite element model, by considering the magnetic vector potential, A, and the electric scalar potential, ∇V, as degrees of freedom at the nodes. Faraday's law for the electric field, $\mathbf{E}$ (section 2.1), is written as,

$$\nabla \times \mathbf{E} = -\frac{\partial \mathbf{B}}{\partial t}. \tag{5.7}$$

The magnetic flux density, $\mathbf{B}$ can be represented in terms of the magnetic vector potential, $\mathbf{A}$[34]

$$\mathbf{B} = \nabla \times \mathbf{A}, \tag{5.8}$$

therefore, Faraday's law can be written as:

$$\nabla \times \mathbf{E} = -\frac{\partial(\nabla \times \mathbf{A})}{\partial t}, \tag{5.9}$$

$$\nabla \times \left(\mathbf{E} + \frac{\partial \mathbf{A}}{\partial t}\right) = 0., \tag{5.10}$$

$$\mathbf{E} = -\frac{\partial \mathbf{A}}{\partial t}. \tag{5.11}$$

The equation is solved by adding a scalar gradient, ∇V, referred to as the electric scalar potential[34],

$$\mathbf{E} = -\frac{\partial \mathbf{A}}{\partial t} - \nabla V. \tag{5.12}$$

Ampère's law for the magnetic field, $\mathbf{H}$ (section 2.1), is defined as,

$$\nabla \times \mathbf{H} = \mathbf{J} + \varepsilon \frac{\partial \mathbf{E}}{\partial t}. \tag{5.13}$$

If $\mathbf{J} \gg \varepsilon \frac{\partial \mathbf{E}}{\partial t}$ at a sufficiently low frequency; for a good condoctor, it can be written as,

$$\nabla \times \mathbf{H} = \mathbf{J}. \tag{5.14}$$

Ohm's law for the current density is[125],

$$\mathbf{J} = \sigma \mathbf{E} + \mathbf{J}_{\text{ext}} \tag{5.15}$$

where, $\mathbf{J}_{\text{ext}}$ represents any externally generated current, such as current generated in a transmit coil. Equation (5.14) becomes,

$$\nabla \times \mathbf{H} = \sigma \mathbf{E} + \mathbf{J}_{\text{ext}}. \tag{5.16}$$

Substituting for $\mathbf{E}$ using eq. (5.12),

$$\nabla \times \mathbf{H} = \sigma\left(-\frac{\partial \mathbf{A}}{\partial t} - \nabla V\right) + \mathbf{J}_{\text{ext}}. \tag{5.17}$$

The constitutive relationship between the magnetic field, $\mathbf{H}$, and the magnetic flux density, $\mathbf{B}$ is,

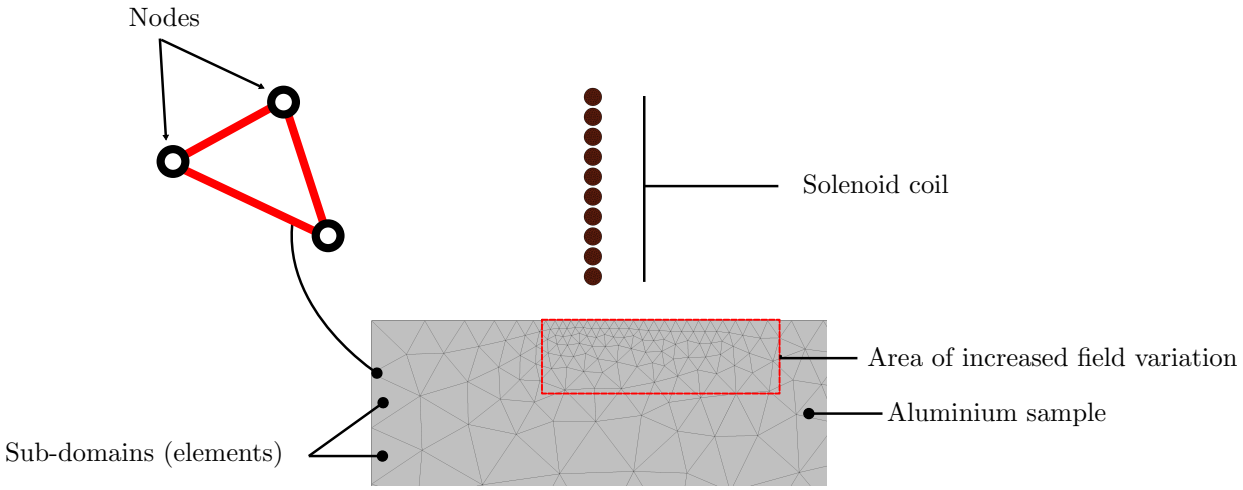

Figure 5.3: 2D axi-symmetric model of a 10 turn solenoid coil over an aluminium block. The model is divided into several sub-domains called elements, to which analytical differential equations can be applied to find an approximate solution for the fields in the body.

$$\mathbf{H} = \frac{1}{\mu}\mathbf{B}, \tag{5.18}$$

for a linear and isotropic material, where μ is the magnetic permeability. Hence eq. (5.17) becomes,

$$\frac{1}{\mu}(\nabla \times \mathbf{B}) = \sigma\left(- \frac{\partial \mathbf{A}}{\partial t} - \nabla V \right) + \mathbf{J}_{\text{ext}}. \tag{5.19}$$

$$\nabla \times (\frac{1}{\mu}\nabla \times \mathbf{A}) = \sigma\left(- \frac{\partial \mathbf{A}}{\partial t} - \nabla V \right) + \mathbf{J}_{\text{ext}} \tag{5.20}$$

rearranging to make $\mathbf{J}_{\text{ext}}$ the subject,

$$\nabla \times (\frac{1}{\mu}\nabla \times \mathbf{A}) + \sigma\left(\frac{\partial \mathbf{A}}{\partial t} + \nabla V \right) = \mathbf{J}_{\text{ext}}. \tag{5.21}$$

For a total current of I_{coil} in a transmit coil, the component of $\mathbf{J}_{\text{ext}}$ in the direction of the wires is defined as,

$$J_{\text{ext}} = N\frac{I_{\text{coil}}}{a}, \tag{5.22}$$

where N is the number of coil turns, and a is the cross sectional area of the coil wire.

The size, and density of the mesh is of great importance, as it determines the accuracy of the model calculations. In electromagnetic finite element modelling, the rate of change in current density is exponential (discussed in section 2.1.4), which means accuracy is increased by increasing the density of elements in areas where larger field variations are expected. The size of the external model boundaries also affects the accuracy of the model calculations as shown by Rosell[116], where the distance of the outer model boundary influenced the accuracy of calculated coil impedance.

The 2-D axi-symmetric model in fig. 5.3, modelled using COMSOL Multiphysics, is of a 10 turn (air-cored coil), located over an aluminium block. The coil has radius of 1 mm, a wire diameter of 0.08 mm, is located 0.2 mm above the sample (coil lift-off), and has a 300 kHz sinusoidal wave current with a peak amplitude of 50 mA. The aluminium block is 3 mm wide, and 1 mm thick.

Comparing the finite element model in fig. 5.4 to the more simplified analytical model in fig. 5.2 shows a good agreement, and validates the finite element model. This is highlighted by the plot presented in fig. 5.5, which shows the induced current density with depth, for a 1 mm thick aluminium block for both the FE model and a comparative analytical model. The parameters for both models are identical, with the coil being a single turn coil, the excitation current, a 50 mA sinusoidal wave current, at a frequency of 300 kHz. As discussed in chapter 2, the current density decays exponentially with depth, and the frequency of excitation determines this rate of exponential decay. The agreement between the analytical model and the FE model is demonstrated in the similarity between their rates of current density decay. The current density is normalised due to the difference in actual values of current density in the models. This is due to the assumptions each model makes. The analytical model assumes that the coil is an infinitely thin filament coil, while for the FE model, the coil wire has finite dimensions. In normalising the current density, each value of current density is divided by the maximum current density, which is the current density at the surface of the block for each model. The utility of finite element modelling is demonstrated in the following sections, where analytical models are not feasible.

Convergence of the model involves finding a solution closest to the analytical calculation within a defined error threshold. The models are solved using the Newton-Raphson method [129, 130], as they are governed by a system of linear equations. Depending on the size, and complexity of the model, it can be solved either directly in one computation, or iteratively, with multiple computations until a solution with an acceptable error threshold is reached.

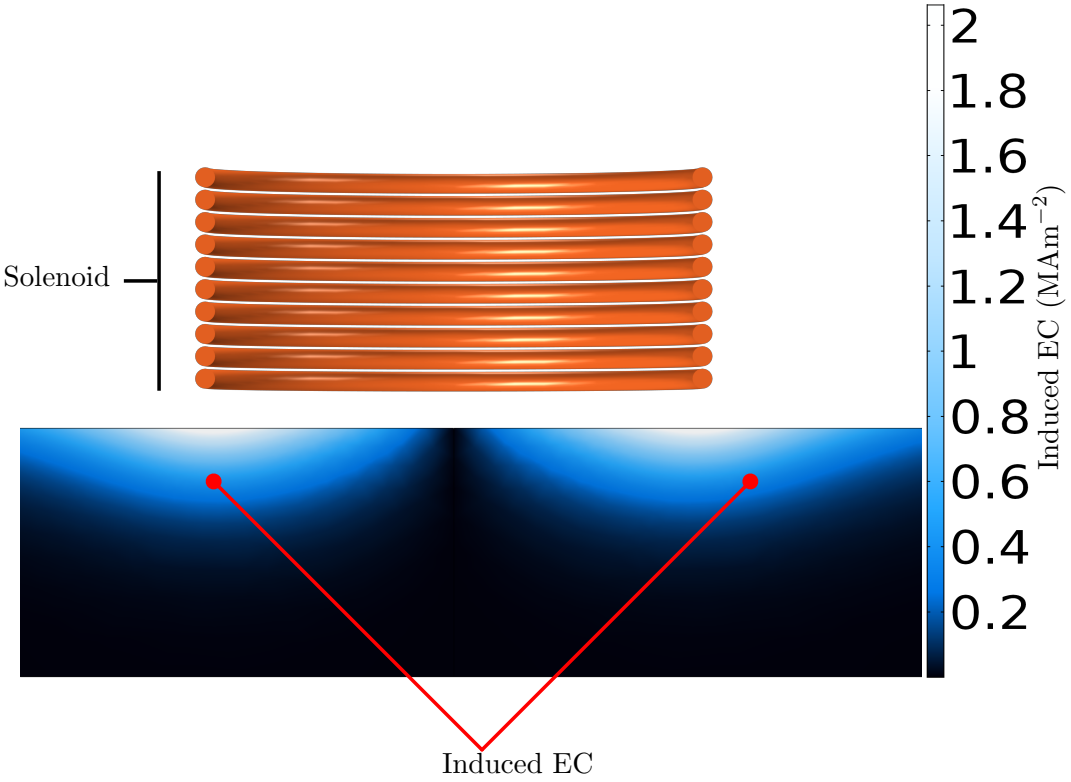

Figure 5.4: 2D axi-symmetric model of a 10 turn solenoid coil over an aluminium block. The coil has radius of 1 mm, a wire diameter of 0.08 mm, is located 0.2 mm above the sample (coil lift-off), and has a current of 50 mA flowing through it at a frequency of 300 kHz. The aluminium block is 3 mm wide, and 1 mm thick. The axi-symmetric nature of the model enables revolution to visualise in 3D. This model was created using COMSOL Multiphysics.

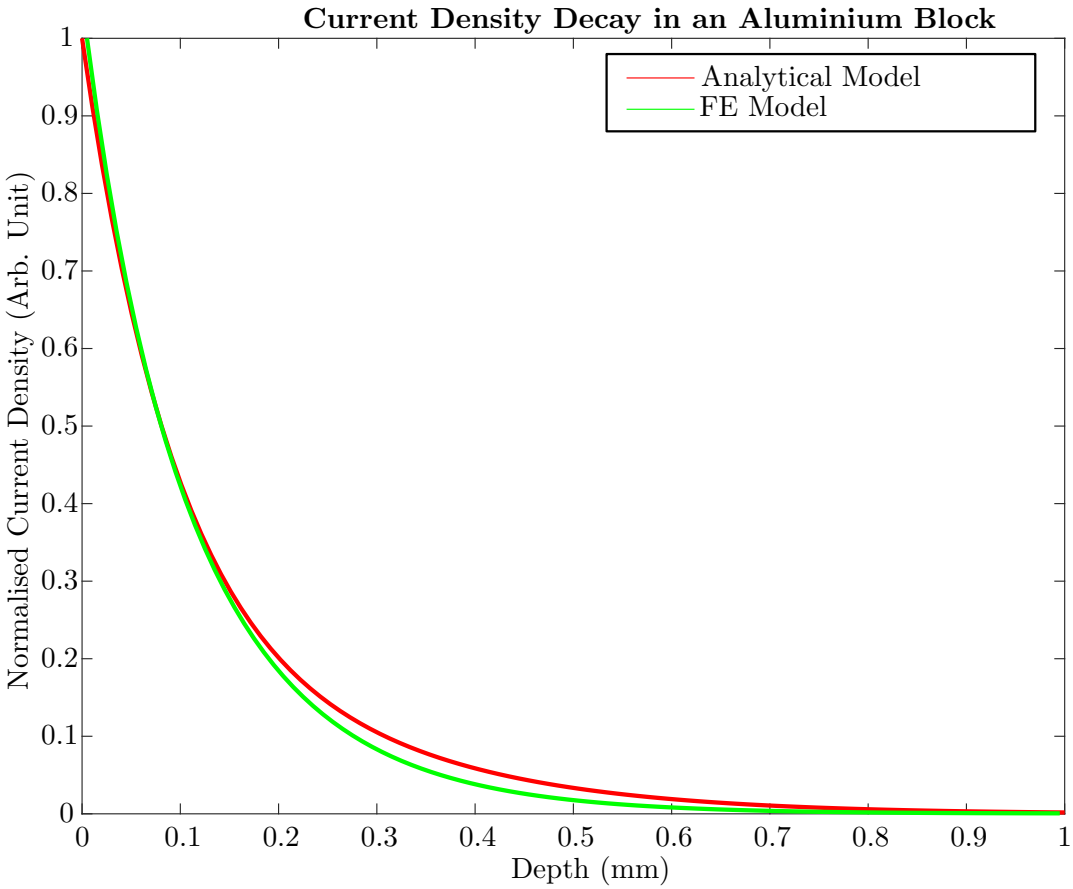

Figure 5.5: Comparison of the normalised current density in a 1 mm thick aluminium block using the analytical model, and the FE model for a 300 kHz excitation current. The current density decays exponentially with depth into the block, and the plot shows that using the parameters defined, the rate of exponential decay for both models is similar. This plot shows the agreement between the analytical, and FE models.

5.3 Modelling a pair of coils

The experiments presented in chapter 4 were conducted using an eddy current probe that contained a pair of solenoid coils with ferrite cores. The probe was used to conduct tests on titanium, and stainless steel samples with defects of different sizes, and finite element models were created using COMSOL Multiphysics to simulate the tests conducted on the samples. The models contain a pair of coils, with and without ferrite cores. One coil is energised with a constant amplitude, alternating current, and the voltage across both coils are measured with the coils located at various positions with respect to the sample surface. The measured voltage across the transmit coil is referred to as absolute data, while that across the receive coil is referred as transmit-receive data.

Modelling the coils as multi-turn coils means that the current density is homogeneous within the coil wires so that factors such as parasitic capacitance and the skin effect are not considered. The model geometry is presented in fig. 5.6. The sample is a stainless steel block with a length of 25 mm, width of 25 mm, and thickness of 2 mm. The large width of the model relative to the coil size, ensures that edge effects of the sample on induced eddy currents are avoided.

The defects of varying lengths, and depths are modelled as semi-circular disks, with the coils 0.4 mm apart, and raised 0.1 mm (coil lift-off) above the sample. The voltage across both coils are calculated at several points as the coil scans across the sample surface in 0.1 mm steps, as shown in fig. 5.7. The coil pair are treated like a probe, with the probe position arbitrarily defined as the midpoint between the axial centres of both coils. The probe is moved a length of 10 mm along the surface of the sample to simulate a scan, as shown in fig. 5.8.

Typically, the measured signal for a transmit - receive probe is the transimpedance [131], defined as the ratio between the voltage in the transmit coil and the current in the receive coil. In the experiments, the current in the transmit coil is kept constant by means of a Howland current source, which means that the change in coil impedances will vary proportionally with respect to the voltage. Hence the coils are modelled as closed circuits, keeping the current within the coils constant, but monitoring the voltages across the coils, which will change as the effective impedances across the coils change. The voltage can be represented as a complex number, $V = a + jb$.

When creating eddy current images, some authors[113, 60], tend to use the real, and imaginary components of the impedance, referred to as 'in-phase' and 'in-quadrature' respectively. A different approach is taken in this thesis, by the use of

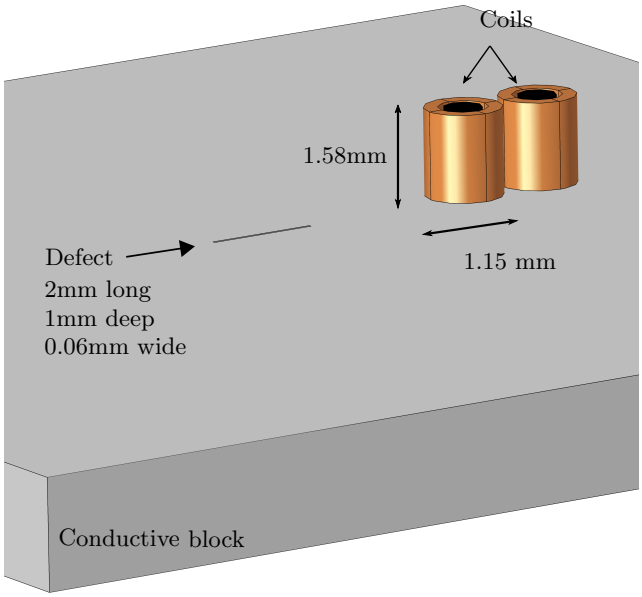

Figure 5.6: Model of a pair of ferrite-cored copper solenoid coils on a conductive sample. The coils are identical with 4 layers at 25 turns per layer, internal and external diameters of 0.9 mm, and 1.15 mm respectively, and heights of 1.58 mm. The conductive block 25 mm × 25mm in area, and 2 mm thick, is made of stainless steel. Semi-circular disk shaped defects of varying lengths and depths are modelled into the block.

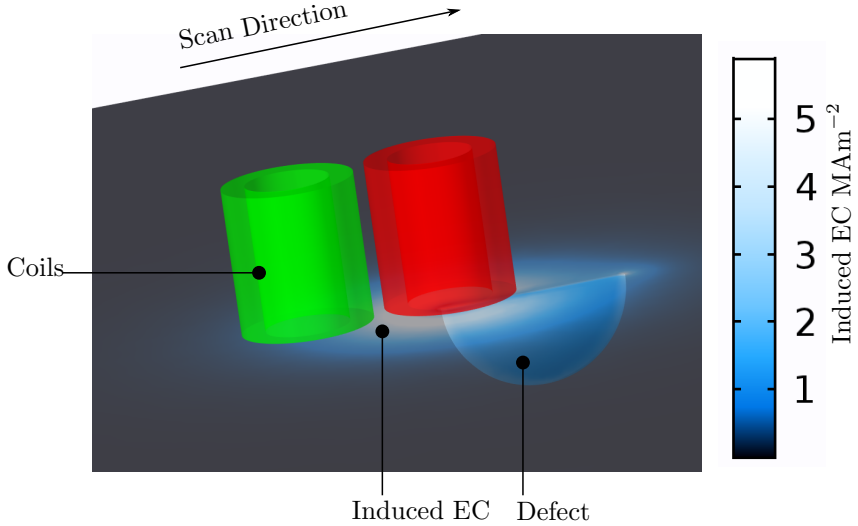

Figure 5.7: Model of a pair of air cored solenoid coils on a conductive sample, showing the currents induced around the semi-circular disk shaped defect. The coils are moved along the length of the defect in the direction shown by the arrow in the image.

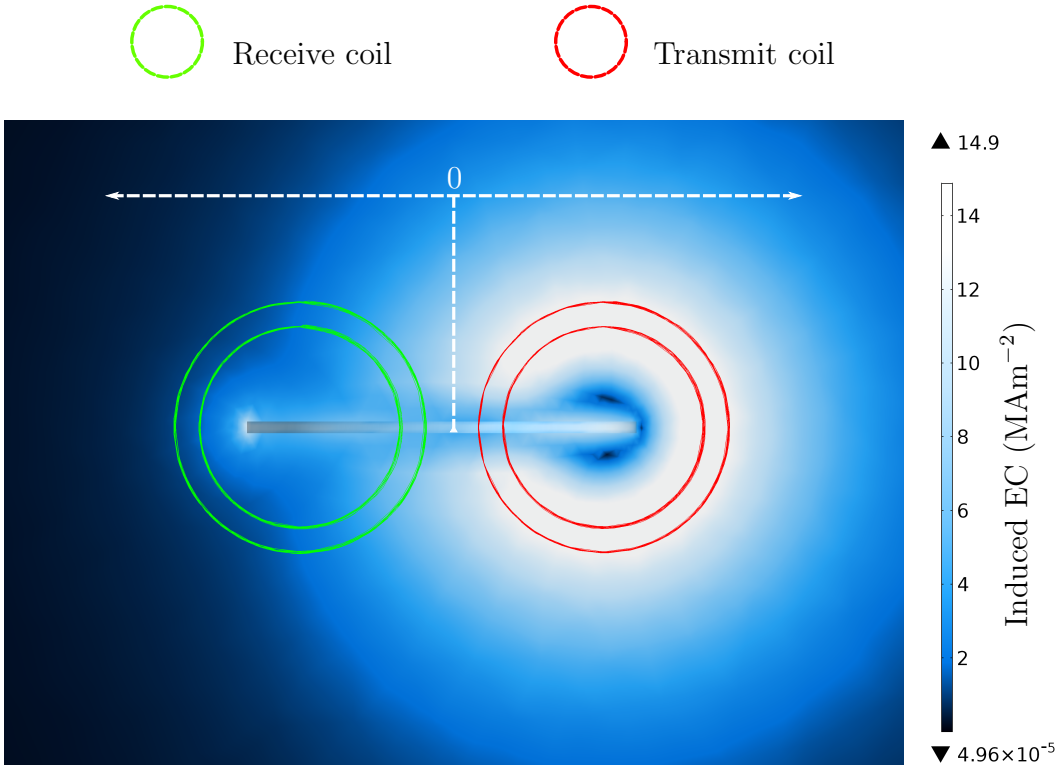

Figure 5.8: Eddy current distribution around a 2 mm long defect induced by a 50 mA, 300kHz current in the transmit coil. The probe position is defined as the midpoint between the axial centres of the coils. The coils are moved a length of 10 mm along the surface of the sample to simulate a probe scan.

the amplitude, and phase of the voltage for generating images. The amplitude $|V|$, and phase, θ, of the coil voltage is evaluated as,

$$|V| = \sqrt{a^2 + b^2} \tag{5.23}$$

$$\theta = \tan^{-1} \frac{b}{a} \tag{5.24}$$

The coils (both air and ferrite cored), are modelled to scan across a stainless steel block, to visualise the interaction between induced eddy currents and the defect. The block has a defect, 2 mm long, 1 mm deep, and 0.06 mm wide. The transmit coil (green) is energized with a 50 mA current alternating at 300 kHz. Eddy currents are induced in the sample skin depth, that flow in a path shaped like the coil footprint. The induced current density is observed to be highest just directly below the coil wires, where the wire is closest to the sample, and decreases away from the wires.

The voltage amplitude (eq. (5.23)), and phase (eq. (5.24)) across the transmit coil, as the coil pair scans along the sample surface is shown in fig. 5.9 (d). The amplitude has two peaks, $\approx$ 2 mm apart, which represent the length of the defect. These peaks show that the maximum change in transmit coil impedance occurs when the defect obstructs one side of the circular eddy current path and not the other. This is because the eddy currents are forced to take the longer path below, or around the defect causing a higher density of current at the edge of the defect as shown in fig. 5.9 (a) and (c).

Figure 5.10 (c) presents the amplitude, and phase of the voltage across the receive coil, as the coil pair scans the surface of the block. A single peak is observed in the receive coil data, which occurs when the defect is most symmetrical in length between the axial centres of the coils as shown in fig. 5.10(a) and (b).

It can be observed that the peaks in the transmit coil voltage data presented in fig. 5.9 (d) do not line up exactly with the edges of the defect, represented by the bar. However, with the probe position defined as the midpoint between the axial centres of the coils, the receive coil data is symmetric along the length of the defect. What this shows is that the coil responses are always shifted by a distance between the midpoint between the coil pair, and the axial centre of the transmit coil, defined as, $r + d/2$. This illustrated in fig. 5.11, where r, is the external radius of the transmit coil, and d, is the length of the separation between the edges of the coils. Compensating for this shift enables the combination of absolute mode with transmit-receive mode data as discussed in other chapters.

It was observed in experiments that the voltage response of the coils differed

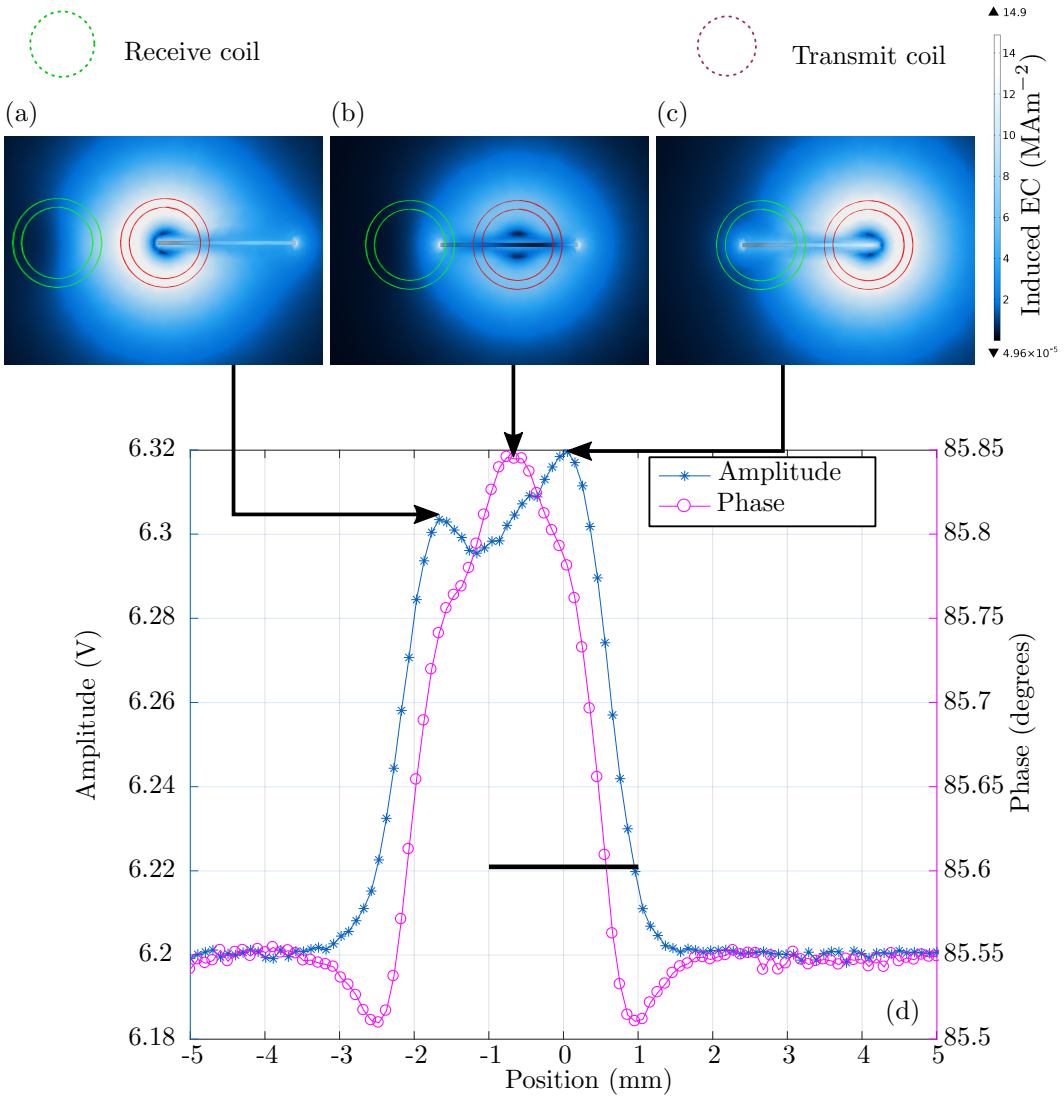

Figure 5.9: Voltage amplitude, and phase of the transmit coil as it scans along a stainless steel block with a 2 mm long defect. The lower amplitude peak, (a) occurs when the probe position is at -1.67 mm, and the higher amplitude peak (c) occurs when the probe position is at +0.05 mm relative to the centre of the defect. The peak phase, (b) occurs at -0.67 mm relative to the defect centre. The plots in (d) represent the amplitude, and phase of the transmit coil voltage for a 10 mm scan on the surface of the sample, with the bar representing the size, and location of the 2mm long defect.

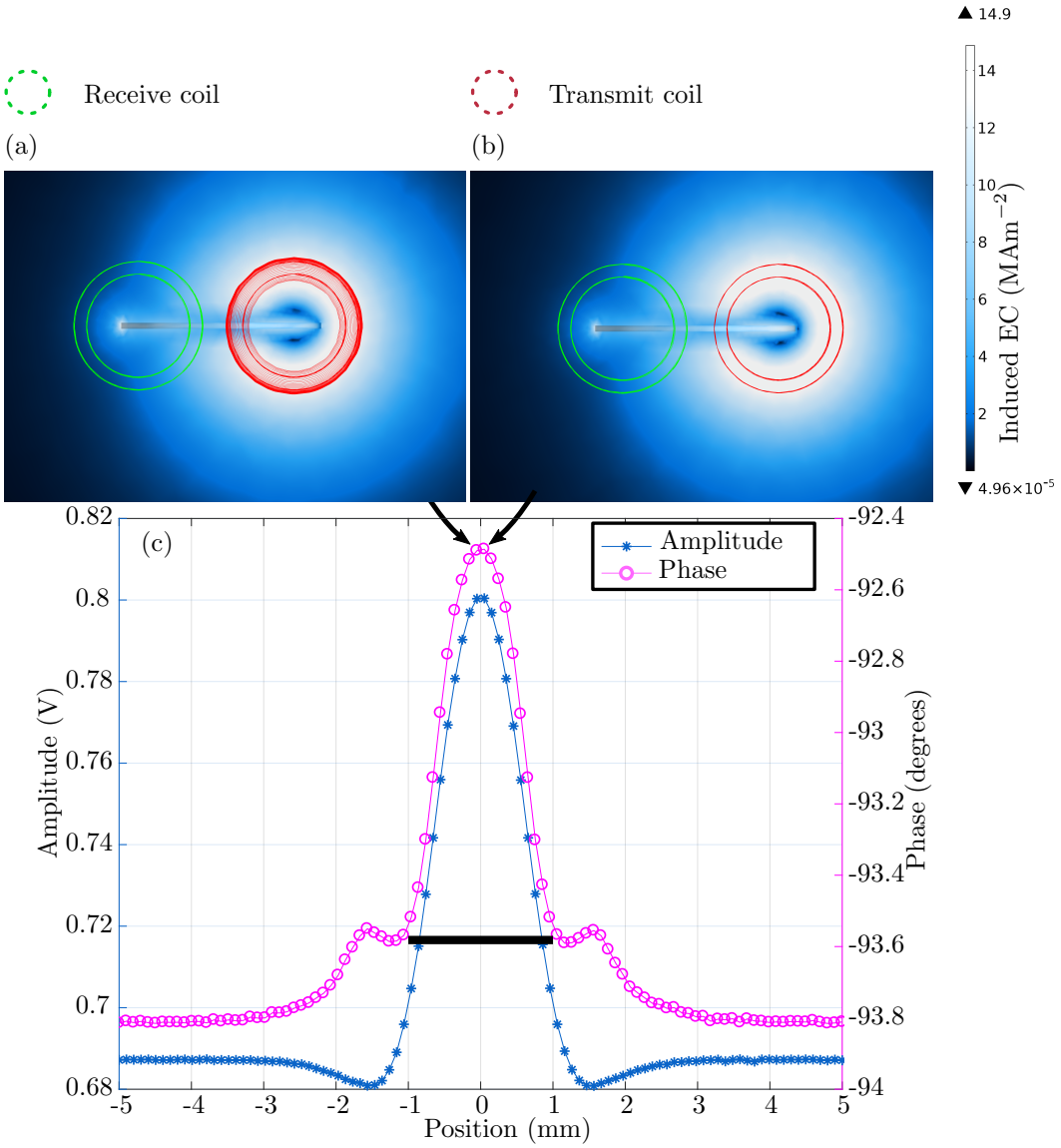

Figure 5.10: Voltage amplitude, and phase of the receive coil as it scans along a stainless steel block with a 2 mm long defect. The probe position (midpoint between the coil axial centres) is at (a) -0.05 mm and (b) +0.5 mm, relative the centre of the defect. Plots in (c) represent the amplitude, and phase of the voltage across the receive coil over the 10 mm line scan, and the bar represents the size, and location of the 2 mm long defect.

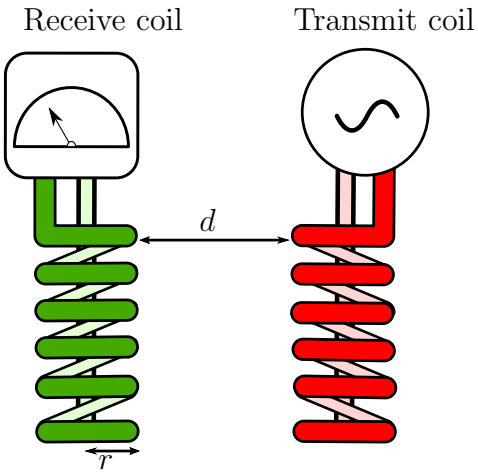

Figure 5.11: Illustration of the dimensions required to calculate the relative shift between the transmit and receive coil data. The transmit coil data is always shifted by $r + d/2$, when probe position is defined as the midpoint between the coil axial centres.

with respect to the orientation of the defect. The data in figs. 5.9 and 5.10 reflected the voltage response when the defect orientation was parallel to the axis of separation between the coils. In fig. 5.12 the eddy current distribution around the 2 mm defect, when the defect is perpendicular to the axis of separation of the coils is presented. Figure 5.12(a) shows the eddy current distribution around the defect, when the transmit coil was on the defect and the receive coil was off, and in Figure 5.12(b), the eddy current distribution is shown, when the receive coil was on the defect, and the transmit coil off.

The amplitude, and phase of the transmit coil voltage response when the transmit coil is on the 2 mm long defect, while the receive coil is off the defect (Figure 5.12(a)) is presented in fig. 5.13(a). The peaks have the same amplitude, and occur symmetrically at -0.86 mm, and +0.86 mm relative to the defect centre. The distance between the peaks is ≈ 2 mm which corresponds to the defect length. As expected, there is no defect indication in fig. 5.13(b), when the transmit coil is off the defect even though the receive coil scans over the defect.

The amplitude, and phase of the receive coil voltage response, when the transmit coil scans over the defect is presented in fig. 5.14(a). The response when the receive coil scans over the defect is presented in fig. 5.14(b). There is some slight variance in the absolute numerical values in the data, which is attributed to rounding errors in the calculations, however, the responses were observed to be identical. The magnitude, and phase in both measurements show peaks at positions that correspond to the edges of the defect, but the phase measurement shows a more

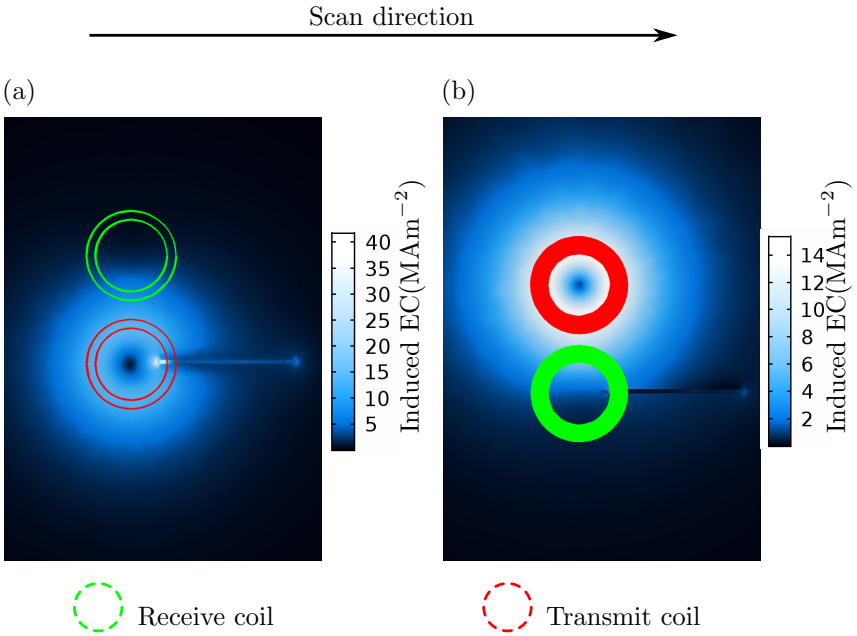

Figure 5.12: Distribution of induced eddy currents around the 2 mm long defect in a stainless steel block, when the axis of separation of the ferrite-cored coil pair is perpendicular to the scan direction. (a) The transmit coil scans along the defect while the receive coil is off the defect, (b) The receive coil scans along the defect while the transmit coil is off the defect.

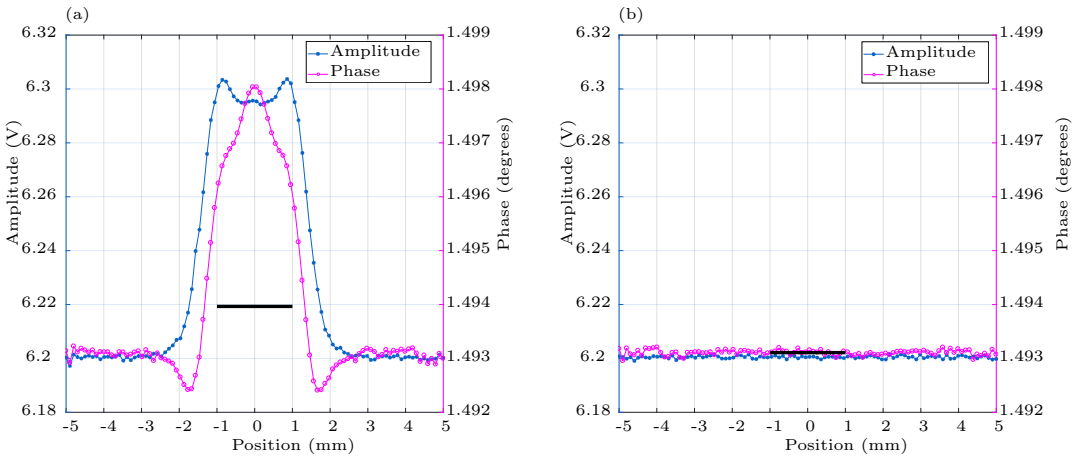

Figure 5.13: (a) Voltage amplitude, and phase across the transmit coil when it scans over the defect, with the receive coil off the defect. The peaks occur at -0.86 mm and +0.86 mm relative to defect centre, and are $\approx$ 2 mm apart, corresponding to the length of the defect. (b) Voltage amplitude, and phase response when the receive coil scans over the defect, with the transmit coil off the defect. There are no indications as the transmit coil does not go over the defect. The bar represents the size, and location of the 2mm long defect.

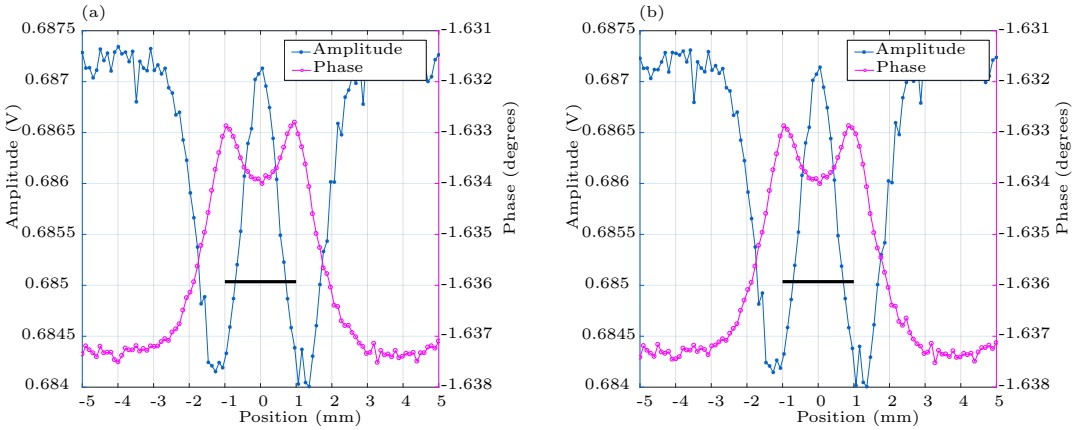

Figure 5.14: Voltage amplitude, and phase across the receive coil (a)when the transmit coil scans over the defect, with it off the defect, and (b) when it scans over the defect with the transmit coil off the defect. Ignoring the slight numerical noise, the responses are identical. The bar represents the size, and location of the defect.

accurate indication of the defect length. The inference from these results is that the receive coil response is independent of the magnetic field fluctuations of the drive coil when the defect is in this orientation. Further analysis of this phenomenon should be done in the future.

5.3.1 Modelling the coil pair with air cores vs ferrite cores

A model with air-cored coils was created to compare with the ferrite-cored coil model. The sample in both models is a stainless steel block, with a defect that is 2 mm long, 1 mm deep, and 0.06 mm wide. The transmit coil is energised with a 50 mA current, at a frequency of 1 MHz. Figure 5.15(a) presents the magnitude, and phase of the voltage across the transmit coil when both coils are air-cored, and fig. 5.15(b), when both coils are ferrite-cored. It can be observed from the plots that the transmit coil voltage amplitude for the ferrite cored model, is more sensitive, with a wider dynamic range compared to the air cored model. This shows that the inclusion of a ferrite core increases the coil sensitivity to defects. From the plots, it can also be observed that the peaks corresponding to the defect edges are more symmetrical in amplitude for the air-cored model fig. 5.15(a), compared to the ferrite cored model fig. 5.15(b), where the second peak, which corresponds to when both coils are on the defect (fig. 5.9 (c)) has a higher amplitude. The symmetry is also visible in the voltage phase response to the defect for the air-cored model, which is not the case for the ferrite cored model. The plots for the air-cored model, are analogous to those in fig. 5.13(a), where the voltage amplitude, and phase

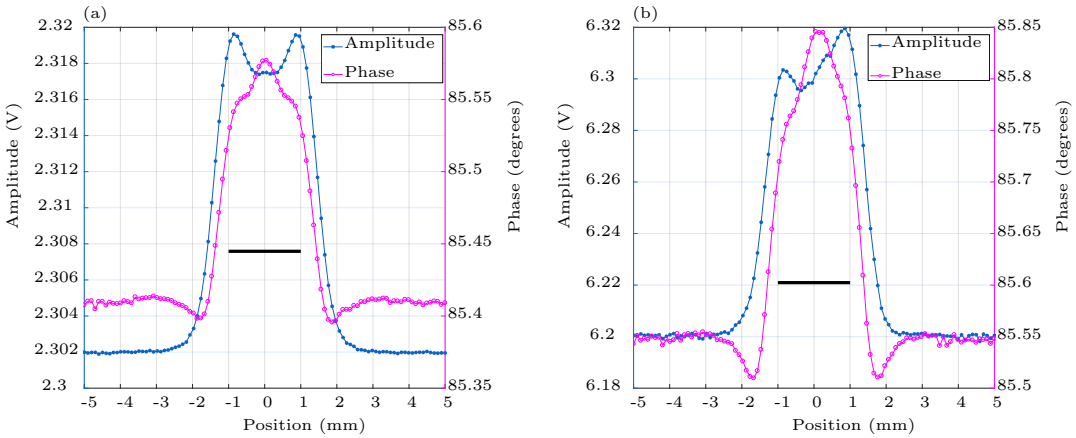

Figure 5.15: Plots of the amplitude, and phase of the voltage across the transmit coil (a) with air cores in both coils, and (b) with ferrite cores in both coils. In these plots, the relative shift between the transmit, and receive coil data has been compensated for. The bar represents the size, and location of the defect.

responses are also symmetrical along the length of the defect, albeit with a higher dynamic range. These results show that the presence of a core in the receive coil causes a higher inductive response in the transmit coil, when both coils are over the defect. The ferrite core in the receive coil focuses the magnetic field from the transmit coil, causing an increase in induced eddy current density in the sample. When this happens, the edge of the defect causes an even higher concentration of eddy currents, thereby increasing the inductive coupling between the transmit coil and the eddy currents in the sample.

The voltage amplitude, and phase across the receive coil for the air-cored model is presented in fig. 5.16(a), and for the ferrite-cored model, in fig. 5.16(b). From these plots the increased dynamic range contributed by the presence of the ferrite cores is visible.

5.3.2 Modelling scans of 0.25 mm and 0.5 mm long defects

The coils were modelled to scan along a stainless steel block containing semi-circular disk shaped sub-millimetre long defects, oriented parallel to the axis of separation between the coils. The first defect is 0.25 mm long, 0.125 mm deep, and 0.06 mm wide, while the second is 0.5 mm long, 0.25 mm deep, and 0.06 mm wide. The coils contain ferrite cores, and the transmit coil was energized with a 50 mA alternating current, at a frequency of 300 kHz.

Figure 5.18 presents the shift compensated voltage amplitude, and phase of the transmit coil for a line scan along the surface of the sample. The data reflects

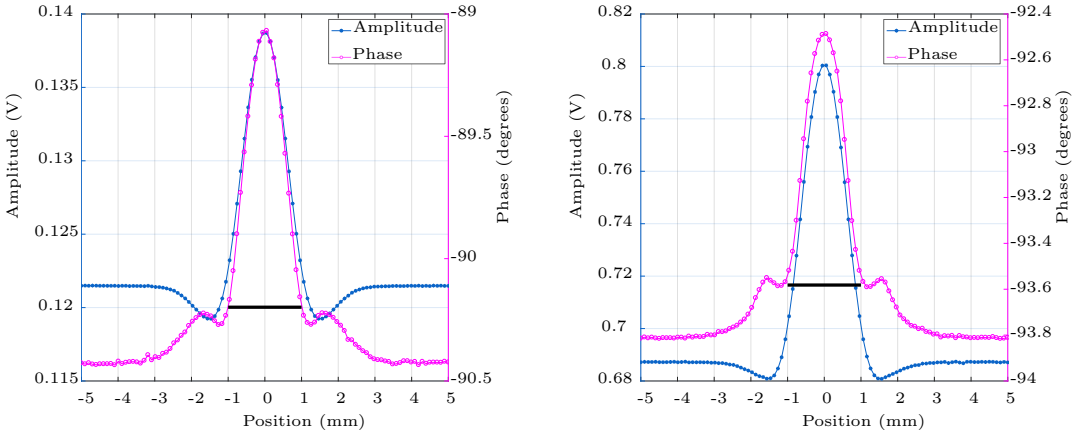

Figure 5.16: Plots of the amplitude, and phase of the voltage across the receive coil (a) with air cores in both coils, and (b) with ferrite cores in both coils. The increased dynamic range is visible in the ferrite-cored model. The bar represents the size, and location of the defect.

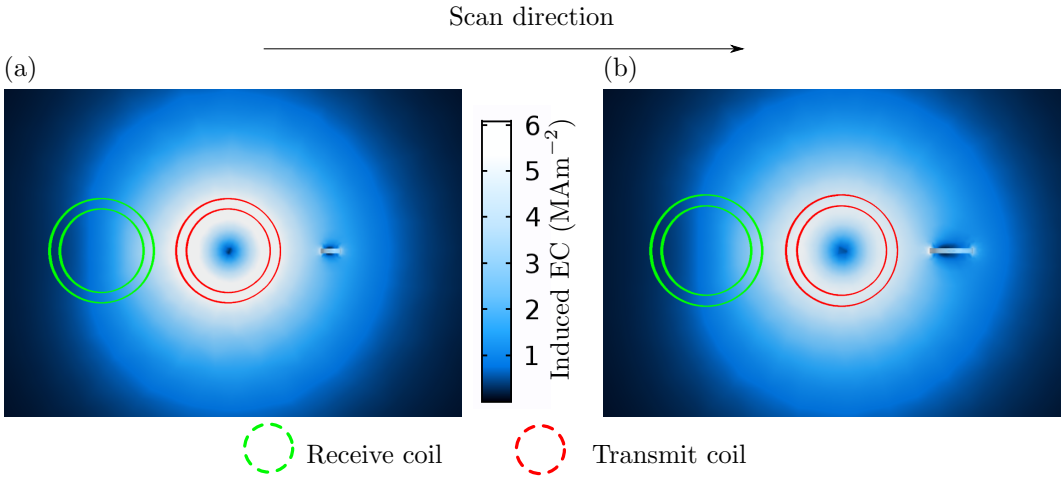

Figure 5.17: Eddy current distribution around the (a) 0.25 mm long defect, and (b) 0.05 mm long defect. The defects are oriented parallel to the axis of separation of the coils, as the coils scan 10 mm along the surface of the stainless steel block.

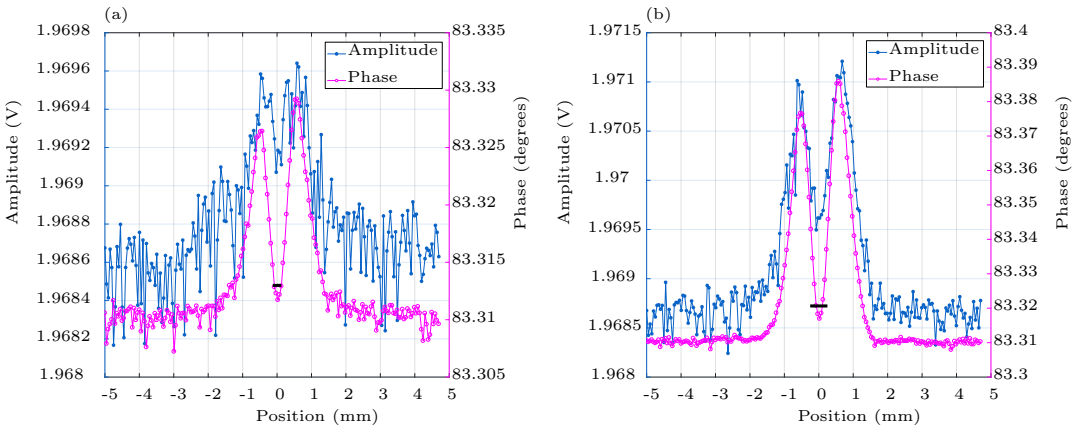

Figure 5.18: Voltage amplitude, and phase of the transmit coil as it scans along the block (a) with a 0.25 mm long defect, and (b) a 0.5 mm long defect. The bars represent the size, and location of the defect.

two peaks in each case, which correspond to the defect being located at each edge of the coil. The small size of the defects relative to the coil diameter results in the peaks not accurately reflecting the size of the defects, however, the defect locations are reflected in both cases. From these plots, while similar, it can be observed that the voltage phase plots have a higher dynamic range than the amplitude plots, but in either case, the signal is worse with the smaller defect. Compared to the amplitude plots in figs. 5.9 and 5.15, the troughs between the peaks have a much lower amplitude for the sub-millimetre defects. This is as a result of the defects being smaller than the internal diameter of the coil, which means that at these points, the defects are located in areas where the density of induced eddy currents is much lower.

The location of the transmit coil relative to the defect, when the peaks and troughs of the voltage, amplitude, and phase occur is depicted in fig. 5.19. Figure 5.19(a) and (c) show that the defect obstructs the circular flow of eddy currents at the sides of the coil, which causes an increased density of eddy currents at the edge of the defect. The defect however, is neither long, nor deep enough to completely obstruct the flow of eddy currents, hence the peaks do not completely identify the defect edges. The trough fig. 5.19(b) occurs when the defect is completely encompassed within the induced eddy currents circular path. The coil voltage phase indicates a lower trough compared to the coil voltage amplitude, but the edges of the defect still obstruct the flow of eddy currents to a small extent, which causes the trough to have a higher absolute value than the case where there is no defect, indicating the presence of a defect. These scenarios are equally applicable to the

0.25 mm long defect case.

The voltage amplitude, and phase of the receive coil for the scans is presented in fig. 5.20. Figure 5.20(a) is a plot of the voltage amplitude, and phase across the receive coil as it scans along the surface of the stainless steel block with a 0.25 mm long defect, and fig. 5.20(b) is the scan of a stainless steel block with a 0.5 mm long defect. These plots follow the trend of previous scans, showing a less noisy indication of the defect location, with the peaks being symmetrical along the length of the defect.

The location of the receive coil with respect to the defect location when the peak occurs for the 0.5 mm defect scan is presented in fig. 5.21. Figure 5.21(a) shows that the peak in the receive coil voltage occurs when the defect is symmetrically between the transmit coil and receive coil.

The peaks in the receive coil data for the 0.25 mm scan fig. 5.20(a) also occur at the location depicted by fig. 5.21. The receive coil data also shows an increase in noise content as the defect gets smaller, which is attributed to the defect not being big enough to have a high density of induced eddy currents at its edges, resulting in a less prominent alteration of the coil inductance due to the coupling between the induced eddy currents and the coil. The apparent noise in the plots in figs. 5.18 and 5.20 is numerical noise, and is visible due to the scale of the defect signal. The defect sizes are very small compared to the 2 mm long defect, thus the defect signals are smaller, meaning the data has a much smaller signal to numerical noise ratio.

Chapter 4 presented experiments conducted using coils, and samples with the same parameters as in these FE models. The modelling was necessary, and used as a guide for the design of the experimental coils, and as a means of validating the experimental results at the low frequency used. The models also served to aid with the interpretation of the experimental results. The design of the coils used in the experiments was iterative. Experiments were conducted using an initial coil design, and models were created and tweaked to improve on the initial design, and to validate the results. The experiments showed that the defects considered were detectable at the low frequency considered, and this was validated using the FE models presented.

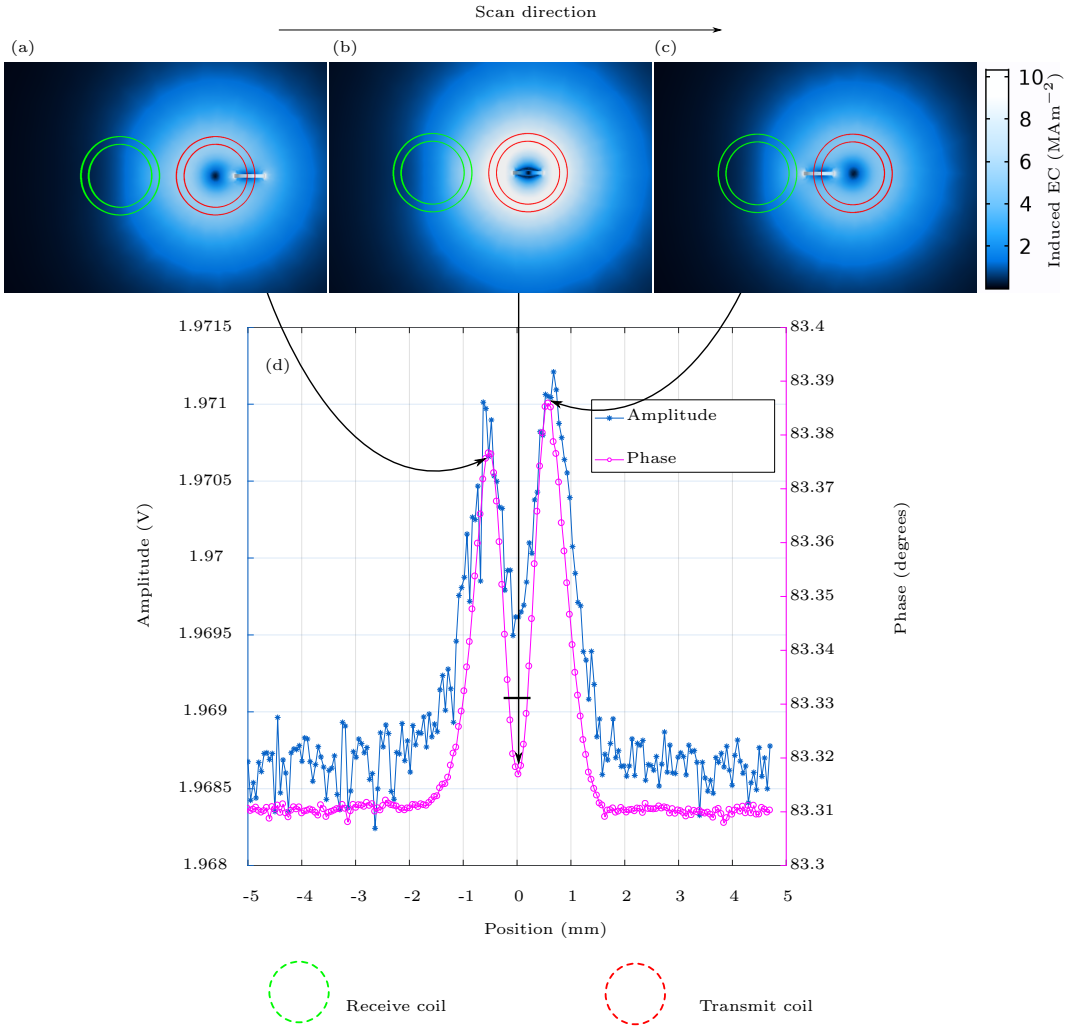

Figure 5.19: The distribution of induced eddy currents when the transmit coil voltage peaks occur. (a) The first peak occurs when the defect obstructs one side of the circular eddy current path. (b) The trough occurs when the entire defect is with the internal diameter of the coil. (c) The second peak, with a higher amplitude occurs when the defect obstructs the circular flow of eddy currents at the side of the coil closest to the receive coil. The bar in (d) represents the size, and location of the defect.

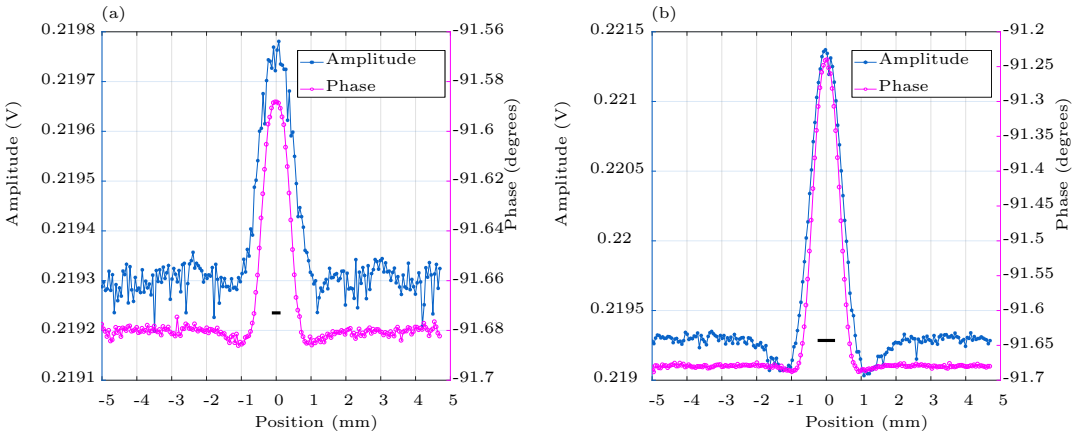

Figure 5.20: Voltage amplitude, and phase of the receive coil as it scans along the stainless steel block (a) with a 0.25 mm long defect, and (b) a 0.5 mm long defect. The bars represent the size, and location of the defect.

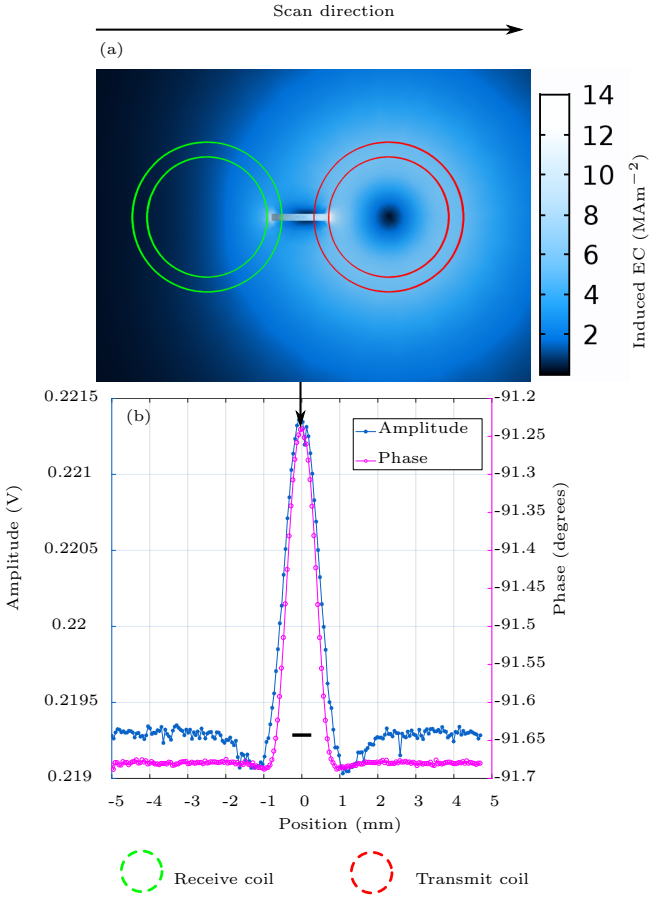

Figure 5.21: The distribution of induced eddy currents when the receive coil voltage peak occurs. (a) The peak occurs when the defect is symmetrical between the edges of the transmit and receive coils. The bar in (b) indicates the size, and location of the defect.

5.4 Summary

This chapter outlines the steps taken in creating finite element models that show the interaction between eddy current probe coils and defects in stainless steel samples. A single solenoid coil on an aluminium block was modelled using the Dodd and Deeds analytical equations, and compared to a final element model with similar parameters.

Models of a pair of coils scanning along the surface of a stainless steel sample were demonstrated. The samples contained defects with lengths of 2mm, 0.5mm, and 0.25mm, and the locations of the coils with respect to the defect when the peaks occurred in the data were demonstrated for both absolute, and transmit receive modes.

The difference in coil voltage response for ferrite-cored coils, compared to air-cored coils was demonstrated, and showed that air-cored coils reflected a symmetrical voltage response, but ferrite-cored coils were more sensitive, with a higher dynamic range.

The transmit-receive data was shown to have lower noise content compared to absolute mode data, and to have peaks which were symmetrical along the length of the defects, enabling accurate identification of defect locations. Absolute mode data, while having more noise, served to accurately identify the length of the defect, which is longer than the diameter of the coils.

The relative shift in absolute mode data with respect to transmit-receive data was demonstrated, and a method for calculating this shift was outlined. It was shown that absolute and transmit receive data can be combined when one of them is shifted.

Chapter 6

Detecting Sub-Millimetre Defects Using Low Frequency Eddy Currents

The main physical parameters that affect ECT measurements of conductive materials are the electrical conductivity, σ, and the magnetic permeability, μ. The work done in this thesis has been based on non ferromagnetic conductors, and thus for the samples tested, the relative magnetic permeability of these materials, $\mu_r = 1$.

Titanium alloys are widely used in the aerospace[89, 132], and biomedical[133, 134] industries due to their favourable properties such as high strength, and corrosion resistance. The increased use of titanium components for critical systems in industry, and the relative brittleness of the material[135], has given rise to the demand for reliable and accurate inspection methods for the detection of small defects to prevent potential catastrophic failures of these systems.

Low conductivity materials such as titanium have much deeper depths of penetration at the same frequency (based on eq. (2.54)) when compared to high conductivity materials such as aluminium and copper[136](see table 6.1). This is why high frequency ($>$ 2 MHz) measurements are commonly used for the detection of surface flaws in titanium[137, 138, 139]. High frequency, conventional EC measurements come with challenges however, such as a higher rate of core losses when using ferrite cores, and more pronounced parasitic capacitance between the coil turns as the transmit coil excitation frequency approaches resonance. Optimising an eddy current coil for high frequency measurement can be achieved by making it air cored, and using a single layered wound coil. This however decreases the coil sensitivity, as the effective coil inductance is also decreased.

Material	Resistivity ($\mu\Omega$m)	Conductivity (MSm^{-1})
Stainless steel (AISI Type 316)	0.77	1.30
Titanium (Ti)	0.78	1.27
Gamma titanium aluminide (γ-TiAl)	2.29	0.44
Aluminium (Al)	0.027	37.7
Copper (Cu)	0.017	59.5

Table 6.1: Material resistivity and conductivity values. After[90, 91, 92, 93, 140].

This chapter presents the results from experiments done to detect defects with lengths as short as 0.25 mm in stainless steel, titanium, and titanium aluminide using coils driven in absolute, and transmit-receive mode, with an excitation current frequency of 300 kHz. The data processing applied in revealing the defect is discussed, as are the limitations of the modes of operation. The ability to detect such small defects in materials with such low conductivities is a significant advancement in eddy current testing, and has not been presented anywhere before.

6.1 Experimental Method

The experimental set-up presented in chapter 4 is used to scan for surface defects in stainless steel (AISI Type 316), and titanium (Ti - 99.6% purity) plates. The plates contain laser micro-machined sub-millimetre surface defects with dimensions as presented in table 6.2. The experimental set-up consists of a function generator, connected to a Howland current source, which provides a constant amplitude alternating current to the transmit coil (see fig. 4.2). The internal circuitry of the current source enables the measurement of the voltage across the transmit coil, using an oscilloscope to which the receive coil is also directly connected.

The probe contains two solenoid coils mounted adjacent to each other, and the transmit coil is energised by a $\pm$50 mA, alternating current at a frequency of 300 kHz. Chapter 4 presents further details on the dimensions and configuration of the experimental components. MATLAB software is used for controlling the experimental components, and processing the measured voltage data. The signal to noise ratio (SNR) of the data is calculated using the eq. (4.4). Similarly to the criteria defined for the data presented in chapter 4, the threshold for the signal region in the data presented in this chapter is 5 times the standard deviation of the image. This means that a cluster of points with pixel values higher than 5 times the standard deviation of the image is identified to be a location of interest, and the pixel values of the cluster are used for calculating the net signal.

Length (mm)	Depth (mm)	Width (mm)
0.5	0.25	0.1
0.25	0.125	0.1

Table 6.2: Dimensions of the defects tested in stainless steel and titanium.

6.1.1 0.25mm long and 0.5mm long defects in Stainless Steel (AISI Type 316)

The stainless steel plate is 150 mm × 150 mm, and 6 mm deep, and contains two defects with the dimensions presented in table 6.2. Surface C-scans with an area of 10 mm × 10 mm were performed on areas surrounding the defects. The step size of the X-Y stage when generating these scans was 0.05 mm producing an image grid containing 200 pixels × 200 pixels. The measurements for voltage amplitude, and phase across the coils as the pair are scanned along the 0.25 mm long defect is presented in fig. 6.1.

A median filter has been applied to the C-scans to suppress random noise errors that occur during the data measurement process. fig. 6.1(a), and (b) present the C-scans generated from measuring the magnitude, and phase respectively, across the transmit coil (absolute mode data). It is observed that no indication of the defect is shown in these images. The receive coil voltage magnitude, and phase, fig. 6.1(c), and (d) respectively show indications that correspond to the location of the defect. This is concurrent with the observations from the scans in chapter 4 which show the higher dynamic range of the transmit-receive mode data, compared to the absolute mode data.

The C-scans also show trending variations from top to bottom, and left to right in both absolute and transmit-receive mode C-scans. These trends are attributed to a number of factors, such as the unevenness of the surface being scanned, and a backlash in the gears of the X-Y stage. The main cause of these trends however is the variation of lift-off over the course of the scan. The materials are not perfectly flat, and the probe is neither weighted nor spring loaded onto the material surface to prevent scraping as the scan is performed. Absolute mode measurements are more susceptible to lift-off variations than transmit-receive, and this is reflected in the images in fig. 6.1. The low signal response of the coils to the very small defect in a material with a very low conductivity also makes the trends more pronounced.

As discussed in chapters 4 and 5, the absolute mode data is shifted relative to the transmit-receive mode data. This shift can be calculated, and compensated

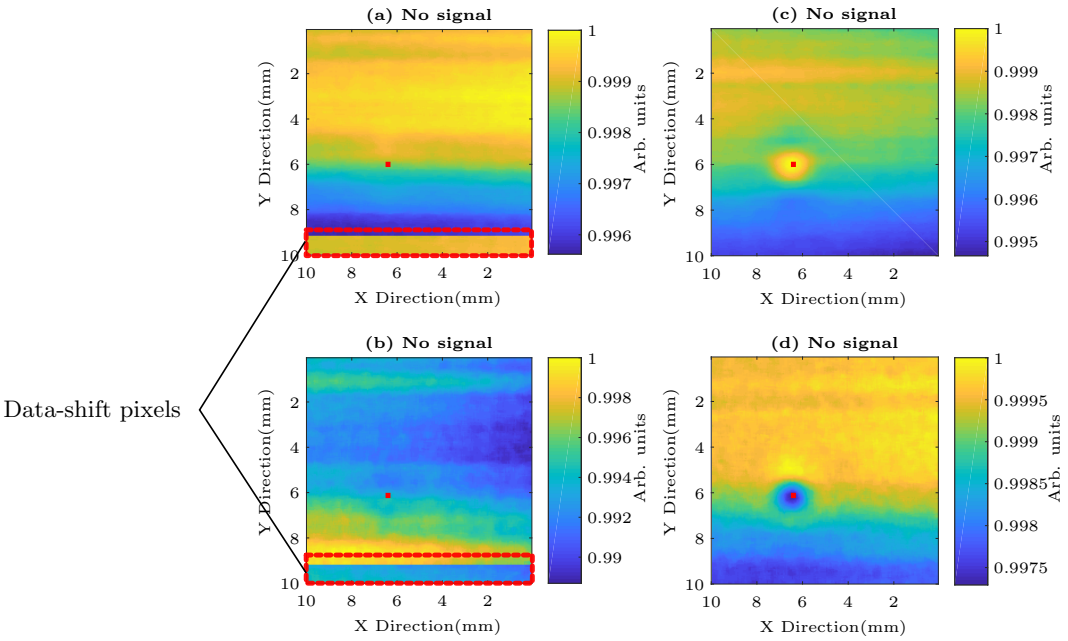

Figure 6.1: C-scans of a 0.25 mm long defect in stainless steel. (a) and (b) are measurements of the transmit coil magnitude, and phase respectively. (c) and (d) are measurements the receive coil magnitude and phase respectively. The red boxes show how shifted pixels are more visible due to the trends present in the data. A median filter has been applied to the data. The SNR measured in all cases do not meet the predefined threshold, and the red bars represent the size, and location of the 0.25 mm long defect on the stainless steel sample.

for to enable combination of the data. The areas in the shift usually correspond to sections of the sample where no defect is present, and ideally should have the same pixel values as other defect free areas of the sample. However, due to the trending variations in the data in fig. 6.1, the areas where the pixels have been shifted are more pronounced.

Absolute mode data is much less sensitive to the defects compared to transmit-receive mode data in terms of the signal response, hence the trends completely hide the defect indications. Improving this data requires the removal of these trends by fitting polynomials to each line of pixels, and subtracting the fitted polynomial from the data. Care is to be taken however in selecting the direction in which the lines are selected. The lines fitted have to be in the direction in which the trends are most linear as to enable the fitting of the lowest order polynomial to the data. From the scans in fig. 6.1, it can be observed that the trends are more linear in the X direction compared to the Y direction. Fitting a high order polynomial (2 and above) in the Y direction resulted in much less accurate removal of the trends compared to fitting a first order polynomial in the X direction.

Figure 6.2 presents the images resulting from fitting a 6th order polynomial to the lines in the Y direction, The absolute magnitude and phase images, fig. 6.2(a) and (b) respectively, have reduced trending variations, but no discernible indication of the defect. The SNR calculated in fig. 6.2(b) is inaccurate, as it uses a section of the image that has artefacts from the de-trending. The transmit-receive magnitude data (c), and phase data (d) are improved compared with the originals, as the background noise standard deviation is now low enough for the pixel values in the defect indication to meet the threshold defined, however there are ringing artefacts in the background aligned with the defect indications along the direction, which the de-trending was applied.

The images in fig. 6.3 result from fitting a 1st order polynomial to the lines in the X direction. Here, the background noise standard deviation is low enough for the signal pixel values to meet the threshold defined for calculating SNR. The absolute mode magnitude, and phase images fig. 6.3(a) and (b) respectively have been considerably improved by de-trending in this manner. The defect indications are visible, but the signal to noise ratios are very low. Transmit-receive mode magnitude, and phase images fig. 6.3(a) and (b) respectively show a considerably higher SNR than the original images, and those resulting from fitting the 6th order polynomial. Ringing corresponding to the direction in which the de-trending was applied is also present, however, it is much less severe, and the location of the 0.25 mm long defect is clearly indicated.

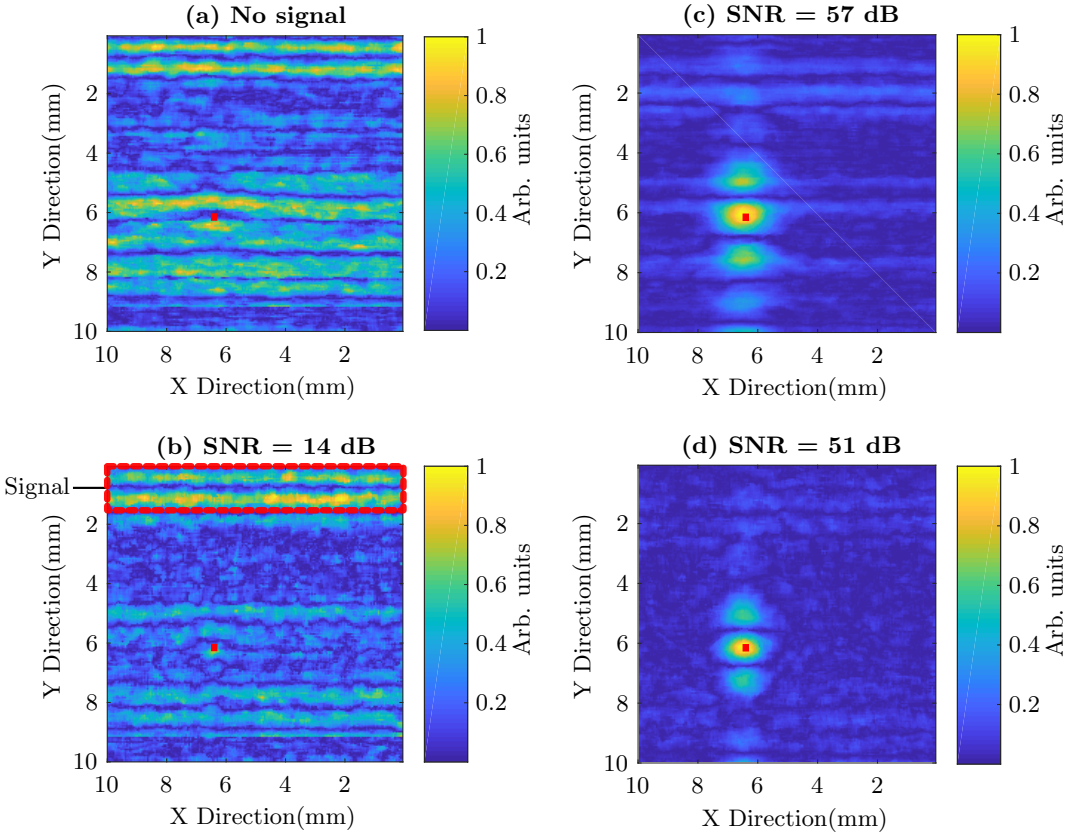

Figure 6.2: Resulting images from de-trending the lines by fitting a 6th order polynomial to the data in fig. 6.1, along the Y direction. The absolute magnitude data (a), and phase data (b) have decreased trending variations, but the images are not improved as the defect indication is not visible. The SNR calculation in (b) is inaccurate, as the program identifies de-trending artefacts (the red box) as signal pixels. Transmit-receive magnitude data (c), and phase data (d) are improved, however there are also ringing artefacts around the defect indication due to the de-trending. The red bars correspond to the size and location of the 0.25 mm long defect.

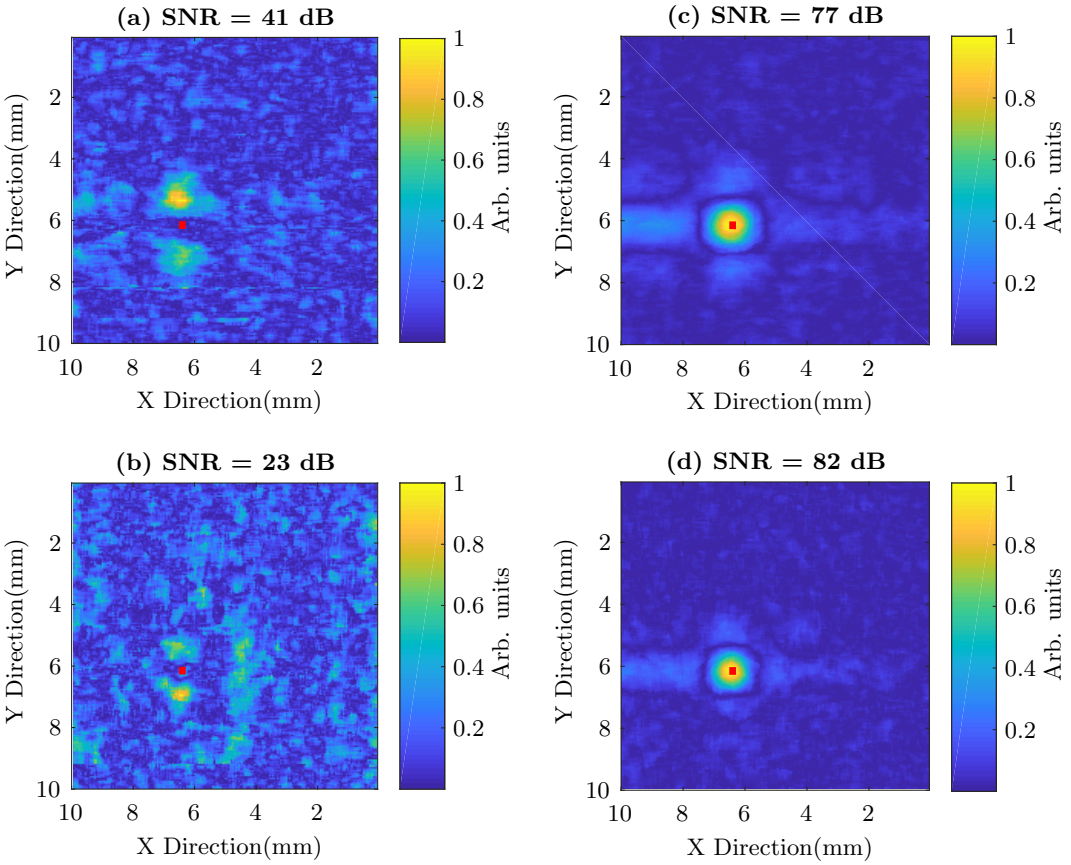

Figure 6.3: Images resulting from de-trending the lines by fitting a 1st order polynomial to the data in fig. 6.1, along the X direction. The absolute magnitude data (a), and phase data (b) are comparably more improved, with the defect indication visible, albeit with a low SNR. The transmit-receive magnitude (c), and phase (d) are also improved, with a higher SNR and clearer defect indication. The red bars represent the size and location of the 0.25 mm long defect on the stainless steel sample.

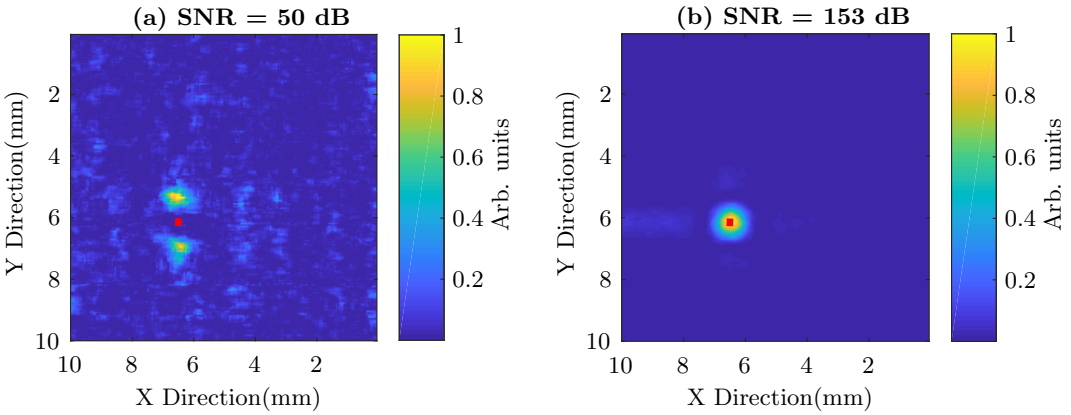

Figure 6.4: Images resulting from the multiplication of absolute mode magnitude with absolute mode phase (a), and the multiplication of transmit-receive mode magnitude with transmit-receive mode phase (b). The resulting absolute mode image is improved, but combination does not increase the defect signal intensity, as it was already too low in the original images. The combined transmit-receive image SNR is considerably improved, and background noise is strongly suppressed. The red bars correspond to the size, and location of the 0.25 mm long defect.

The combination of images by multiplication, to improve SNR was discussed in chapter 4. When the magnitude, and phase images from fig. 6.3 are multiplied, i.e (a $\times$ b), and (c $\times$ d), the resulting combined images are presented in fig. 6.4.

The result of combining absolute mode magnitude with absolute mode phase results in the image presented in fig. 6.4(a). There is visible improvement over the original absolute magnitude data. The small size of the defect results in relatively weak pixel intensities for the defect indication, however, combining the data in this manner significantly suppresses the background noise, resulting in a slightly higher SNR. The combined transmit-receive mode images presented in fig. 6.4(b) also result in a significantly higher SNR compared to the original data. The combined C-scans also result in a tighter indication closer to the exact location of the 0.25 mm long defect, while suppressing the background noise. The increased intensity of the defect indication also serves to suppress the artefacts from the de-trending process. In either case, combining magnitude with phase increases the SNR by suppressing the background variations and increasing the pixel intensities of the defect indication.

When the relative shift between the absolute mode data, and transmit-receive mode data is compensated for, they can be combined to produce a single image with an improved total SNR. From fig. 6.5 it can be observed that the quantitative SNR resulting from the multiplication of absolute mode data with transmit-receive mode data significantly increases the SNR. Visually however, the low resolution of absolute

mode data degrades the resulting combined data.

Scanning a larger 0.5 mm long defect in the stainless steel plate produces the images presented in fig. 6.6, with a median filter applied to the images. The absolute mode magnitude, and phase data fig. 6.6(a and b) show vague indications of the defect. However, the trends present in the image highly obscure the defect indication, and contribute to the large total standard deviation of the entire image. As a SNR value is only calculated when the pixel intensities at the defect indications are higher than 5 times the image standard deviation, SNR values are not calculated in fig. 6.6 (a and b).

The adverse effect of large trends in the image is also evident in the transmit-receive mode C-scans in fig. 6.6(c and d). Here, the defect indications are very visible despite the trend, however the SNRs calculated in these C-scans are very high, but also inaccurate. The high SNR values calculated are due to the program identifying the areas of the trend with high pixel intensities as signal areas and applying them to the SNR calculations. The solution in the case of both absolute mode, and transmit-receive mode data is to de-trend the data to get more accurate defect indications, and SNR calculations. The resulting de-trended images are presented in fig. 6.7.

Figure 6.7(a and b) presents the de-trended magnitude, and phase C-scans (respectively) of the absolute mode data. Here, compared to the original, the defect indication is more visible in both images, with higher SNRs compared to the 0.25 mm long defect scan. The same is the case for the transmit-receive magnitude and phase images (fig. 6.7 (c) and (d) respectively). The pixel intensities of the defect indication are higher for the slightly larger defect, however the artefacts around the defect indication due to the de-trending process are also present.

Combining the magnitude, with phase C-scans for absolute mode (a $\times$ b), and transmit-receive mode (c $\times$ d) results in the images presented in fig. 6.8. Here, as was the case with the 0.25 mm defect in fig. 6.4, there is a significant improvement in SNR for both absolute mode fig. 6.8 (a) and transmit-receive mode fig. 6.8 (b). The improvement in SNR is more significant however, for the larger defect, and in the absolute mode data the indication can be said to produce the minimum length of the defect, while for transmit-receive fig. 6.8 (b), the exact location of the defect centre is clearly indicated.

Compensating for the relative shift in the data, and combining absolute mode data with transmit-receive mode data, the image in fig. 6.9 is produced. In the resulting image, the SNR is significantly improved, almost completely suppressing any background noise. With this data, the location of the 0.5 mm long defect can be confidently determined.

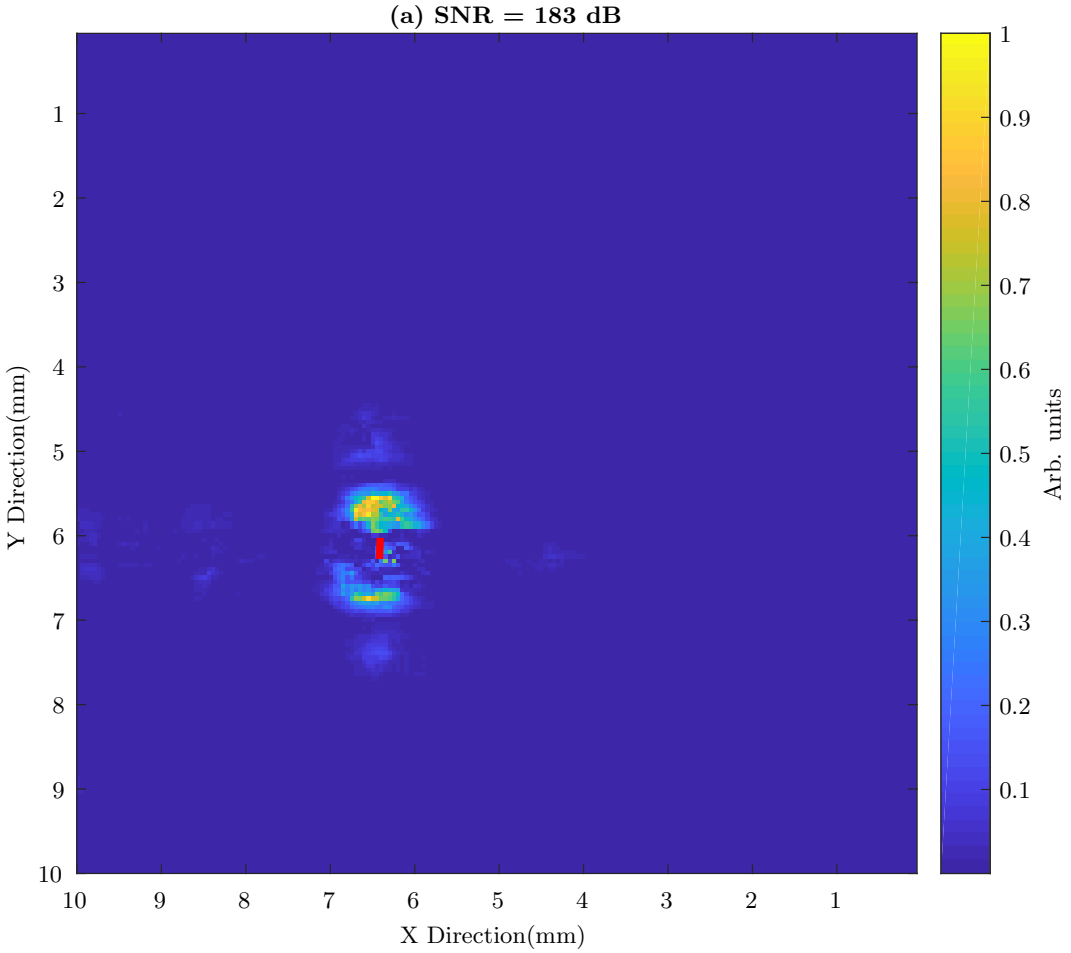

Figure 6.5: Image resulting from the multiplication of absolute mode data, with transmit-receive mode data. This image, albeit with a high SNR, is considered to produce no visible improvement over the individual transmit-receive mode data due to the low resolution of the absolute mode data. The red bar represents the size, and location of the 0.25 mm long defect on the stainless steel sample.

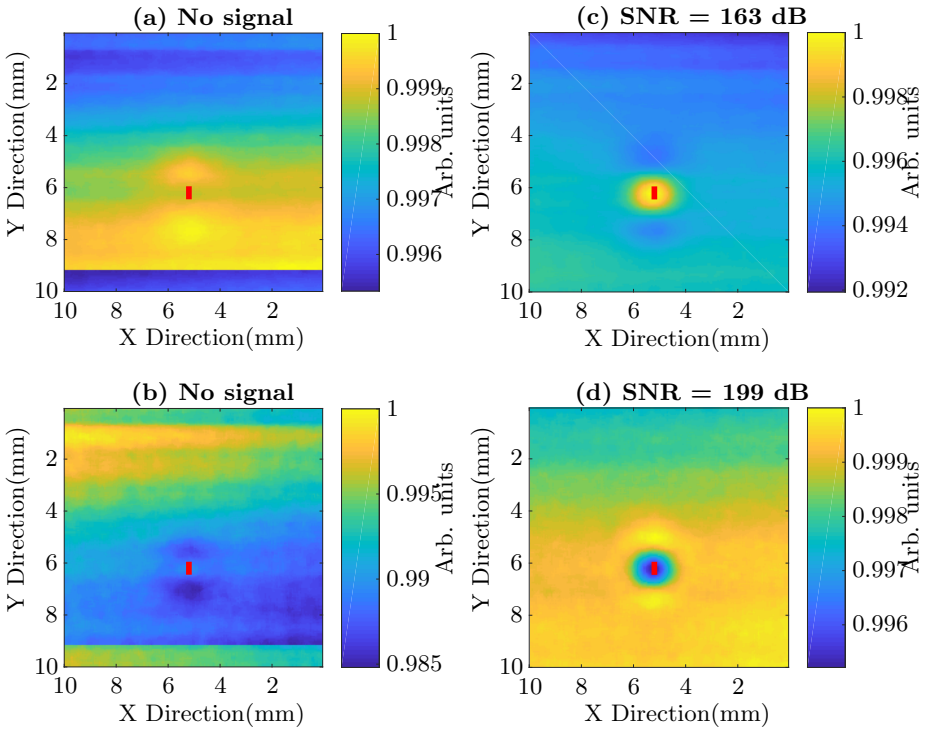

Figure 6.6: C-scans generated after applying a median filter to a scan of a 0.5 mm long defect in stainless steel. the absolute mode magnitude, and phase data, (a) and (b) respectively show vague indications of the defect however the intensities of the defect indication pixels are not high enough relative to the image standard deviation to be used in the SNR calculation. The transmit receive mode magnitude, and phase data, (c) and (d) respectively, show clear indications of the defect with high SNR values which are inaccurate due to the trend in the data.

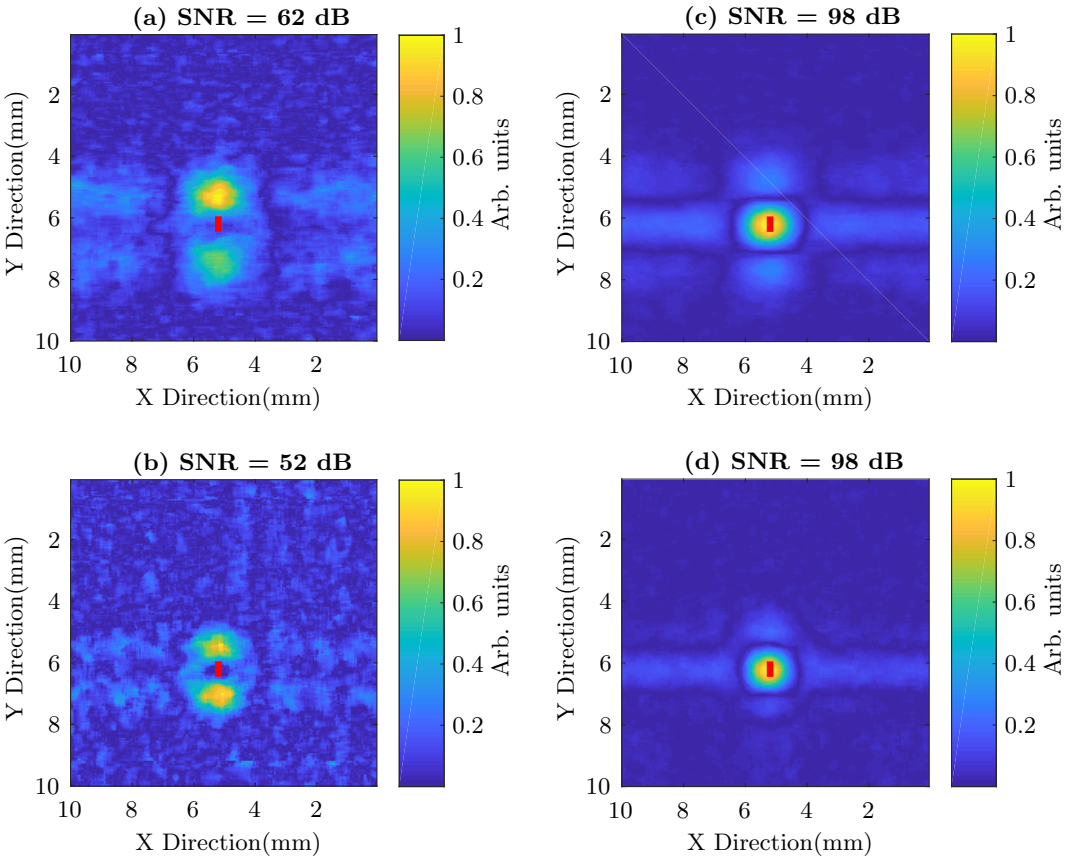

Figure 6.7: C-scans resulting from de-trending the images from fig. 6.6, the absolute mode magnitude, and phase images, (a) and (b) respectively show clearer indications of the defect with higher SNRs compared to the 0.25 mm defect scan. The transmit-receive mode images, (c) magnitude, and (d) phase, also show clear indications of the defect with high SNRs. The red bars represent the size, and location of the 0.5 mm long defect on the stainless steel sample.

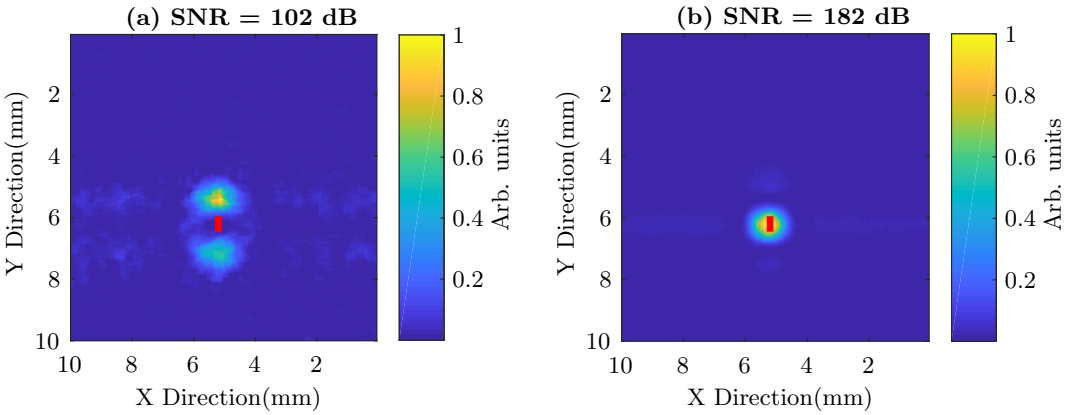

Figure 6.8: C-scans resulting from multiplying amplitude with phase data in absolute mode(a), and transmit receive mode (b). The SNR is improved, as a result of the suppressed background noise, and de-trending artefacts. The red bars represent the size, and location of the 0.5 mm long defect on the stainless steel sample.

6.1.2 0.25mm long and 0.5mm long defects in Titanium (Ti - 99.6 Purity)

A titanium plate, 150 mm × 150 mm in area, and 5 mm thick was scanned with the same experimental set-up discussed previously. The plate contains laser micro-machined surface defects with the same dimensions as presented in table 6.2. The images in fig. 6.10 are the C-scans generated from measuring along the surface of a 0.25 mm defect on the titanium plate. The absolute mode magnitude, fig. 6.10 (a), and phase, fig. 6.10 (b) show no sign of the defect indication, and are heavily trended due to the unevenness of the surface. The transmit-receive magnitude data, fig. 6.10 (c), and phase data fig. 6.10 (d) Show clear indications of the defect, but inaccurate SNR values influenced by the presence of the trends in the data.

De-trending the C-scans result in the images presented in fig. 6.11. It can be observed from fig. 6.10 that the trends in the images are not linear in either direction. This results in the presence of ringing artefacts, irrespective of the direction in which the de-trending polynomial is fitted and shown in fig. 6.11. However, de-trending the data significantly improves the defect indication, with the defect clearly indicated in the absolute mode C-scans (fig. 6.11 (a and b)) unlike the original images, where the defect is not visible. Quantitatively, the SNR is higher in the titanium plate compared to the stainless steel plate for the 0.25 mm defect. Combining magnitude with phase for the absolute mode data, fig. 6.11 (a × b), and the transmit receive mode data fig. 6.11 (c × d) results in the images presented in fig. 6.12. The calculated SNR is considerably improved in both absolute mode fig. 6.12 (a), and transmit-

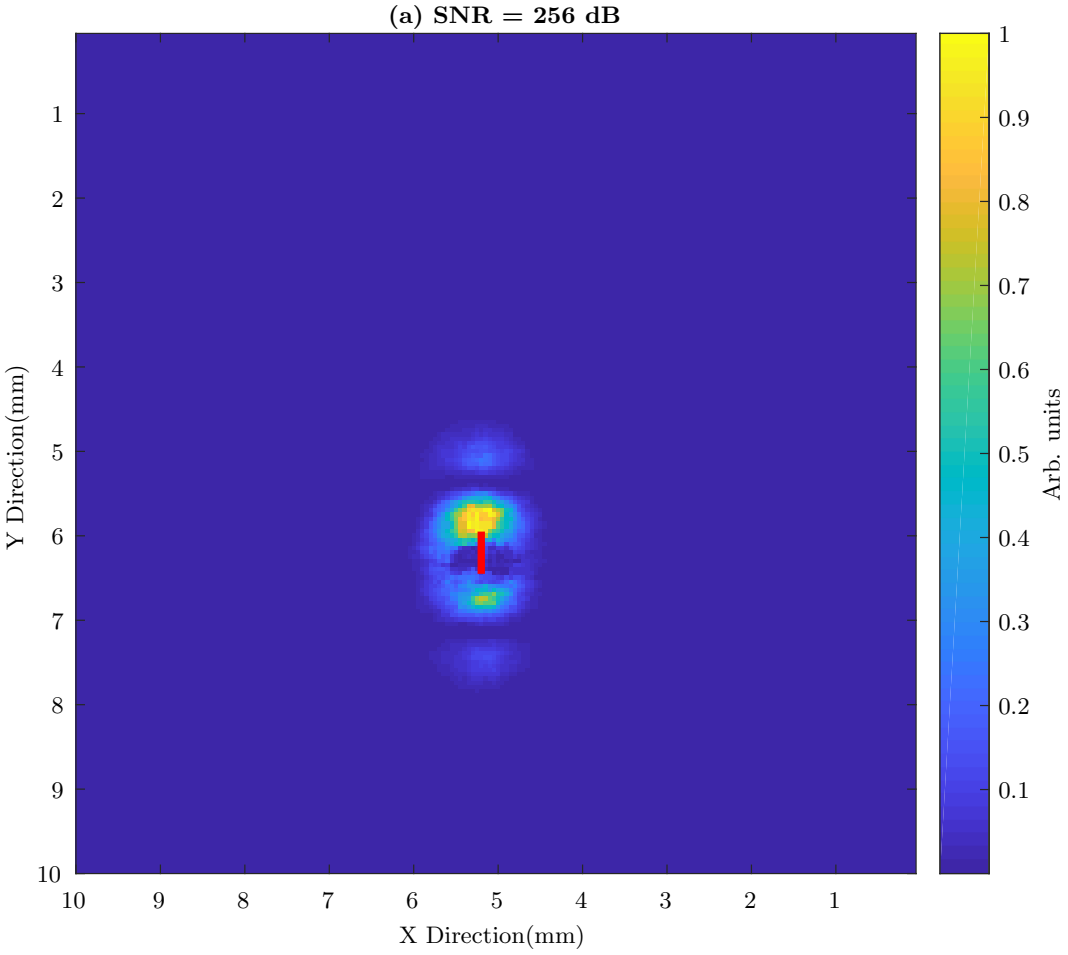

Figure 6.9: The image resulting from multiplying absolute mode data, with transmit-receive mode data. background noise and artefacts are very strongly suppressed and the defect indication is clear. The red bar represents the size, and location of the 0.5 mm long defect on the stainless steel sample.

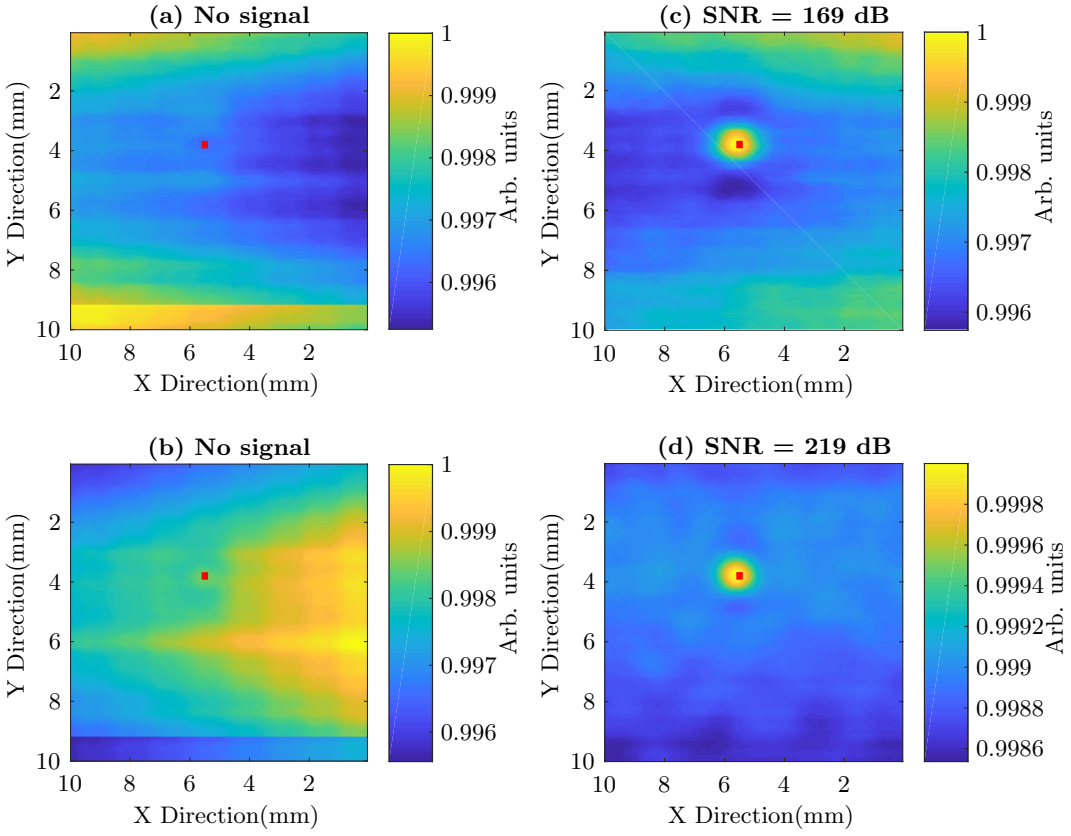

Figure 6.10: C-scans generated from scanning for a 0.25 mm long defect in a titanium plate. The absolute mode data, (a and b) show no indication of the defect, and the standard deviation of the background noise is too high, hence the signal area does not meet the threshold for SNR calculation. The transmit-receive mode data (c and d) show clear indications of the defect, however the calculated SNR values are inaccurate as they are influenced by the trends in the data. The red bars represent the size and location of the 0.25 mm long defect on the titanium sample.

receive mode fig. 6.12 (b), and visually, the 0.25 mm long defect indication is much clearer, in both images with the de-trending artefacts significantly suppressed in the absolute mode data, fig. 6.12 (a), and almost entirely eliminated in the transmit-receive mode data, fig. 6.12 (b).

Compensating for the shift between the absolute mode and transmit-receive mode data, and multiplying them together results in the single image presented in fig. 6.13. Here, the SNR is very much improved, and all traces of background noise, and ringing artefacts resulting from the de-trending process have been suppressed.

Presented in fig. 6.14, are the C-scans generated from scanning the titanium sample for the 0.5 mm long defect. As was the case for the 0.25 mm long defect, the generated C-scans have non-linear directional trends. However, for this slightly longer defect, the absolute mode data fig. 6.14(a and b) show vague indications of the defect. The transmit-receive data (fig. 6.14 (c and d)) show clear indications of the defect location, but inaccurate SNR values resulting from the trends present in the data.

De-trending the data produces a more accurate representation of the defect, and SNR values as shown in fig. 6.15. The non-linear trends in the data result in the artefacts present in the images. The de-trended absolute mode data fig. 6.15 (a and b), show a much clearer indication of the defect edges, while the de-trended transmit receive data fig. 6.15 (c and d), show clear indications of the location of the defect centre.

Combining magnitude data with phase, and then absolute with transmit-receive, the images in figs. 6.16 and 6.17 are produced. Figure 6.16 (a) presents the combined absolute mode magnitude, and phase, showing a substantially improved SNR compared to the original images, and visually, the background noise, and de-trending artefacts are considerably suppressed. For the transmit-receive mode data presented in fig. 6.16 (b), the background noise is almost entirely eliminated, which contributes to the significantly improved SNR. When absolute mode data is combined with transmit-receive mode data, almost all background noise is eliminated, and a sharp indication of the defect is observed (fig. 6.17).

As shown in table 6.1, titanium has a similar conductivity to stainless steel, and in essence, the results from the images presented thus far show a similar performance of this method in detecting sub-millimetre defects in both titanium, and stainless steel. Comparing the results from scanning the defects in stainless steel with those from scanning the defects in titanium, the results show consistently higher sensitivity in titanium. Table 6.3 compares the calculated SNR values for the 0.25 mm, and 0.5 mm long defects in both stainless steel and titanium.

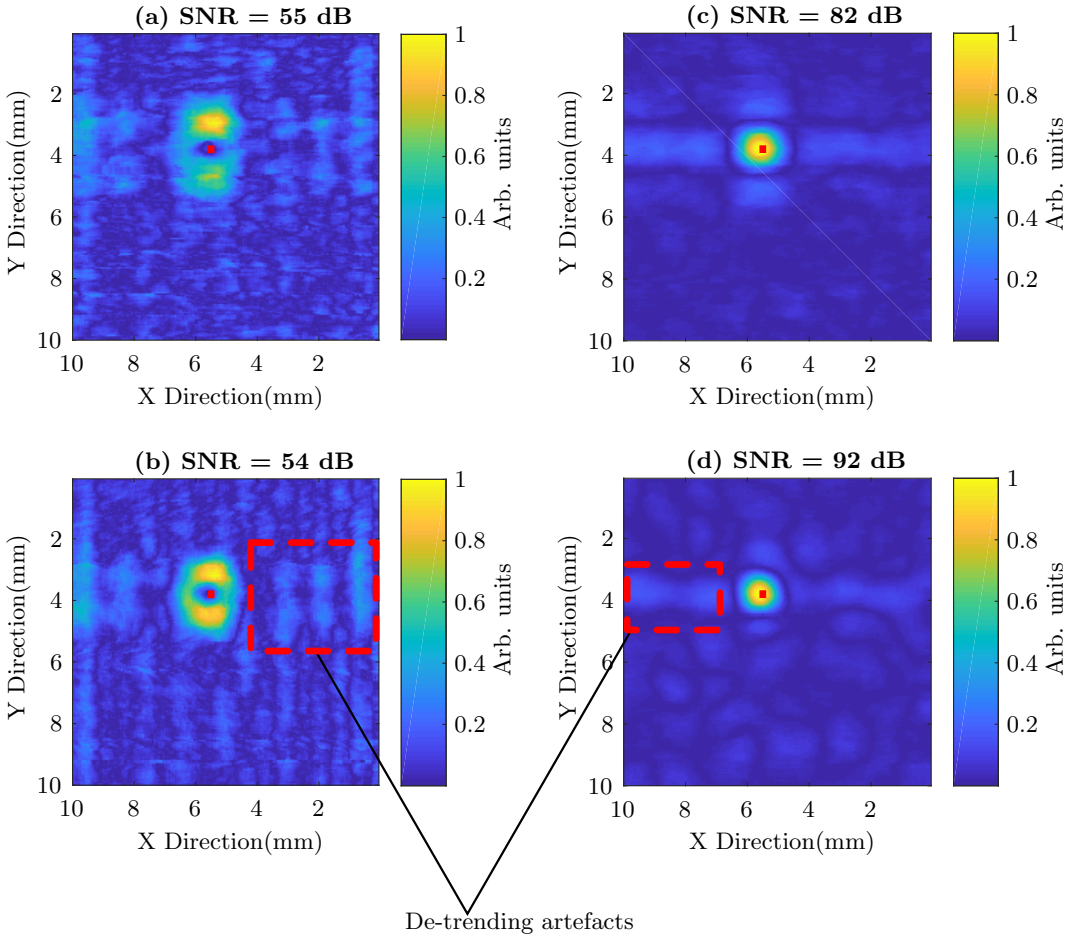

Figure 6.11: De-trended C-scans of the 0.25 mm long defect in titanium. The data is significantly improved, and the absolute mode images (a and b) show clear indications of the defect. The transmit-receive mode images (c and d) show clearer indications of the defect centre location. The de-trending process introduces artefacts into the data (red boxes) irrespective of the direction in which the polynomials are applied. The red bars correspond to the size, and location of the 0.25 mm long defect on the titanium sample.

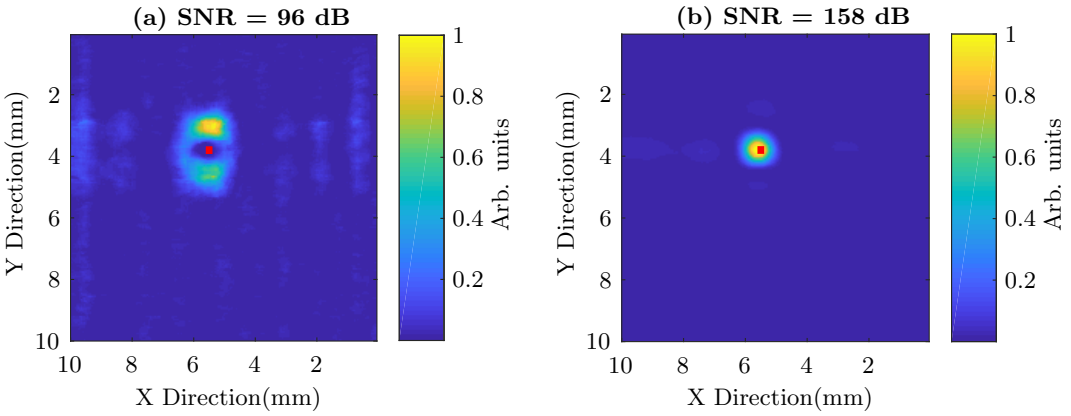

Figure 6.12: Images generated from combining the magnitude, with phase for the absolute mode data (a), and transmit-receive mode data (b), from fig. 6.11. The red bars represent the size, and location of the 0.25 mm long defect on the titanium sample.

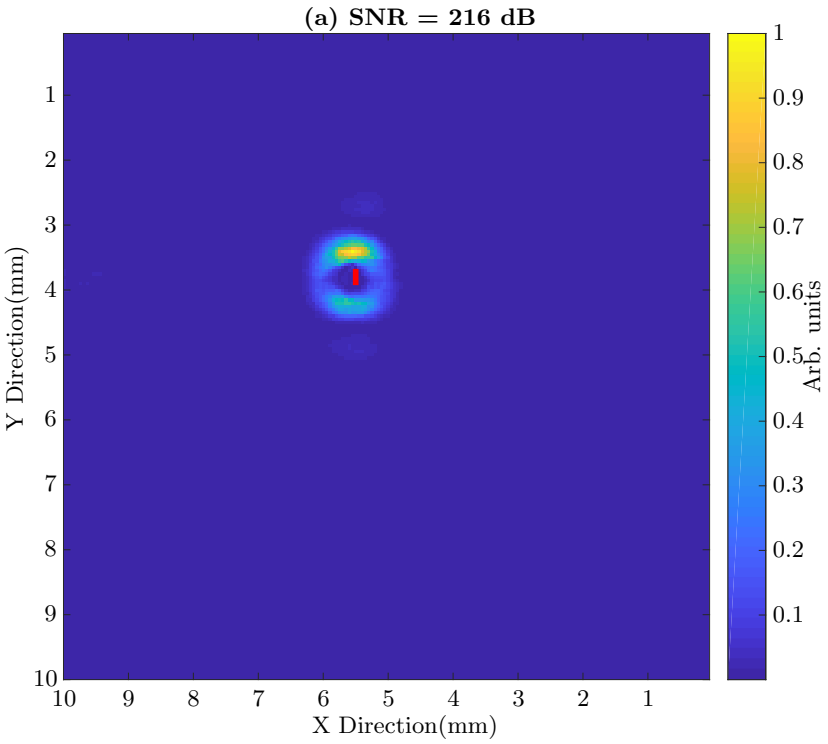

Figure 6.13: The single image generated when absolute mode data is combined with transmit-receive mode data for the C-scans of the 0.25 mm long defect in titanium. The SNR is significantly improved, and the defect indication is clear. The red bar represents the size and location of the 0.25 mm long defect on the titanium sample.

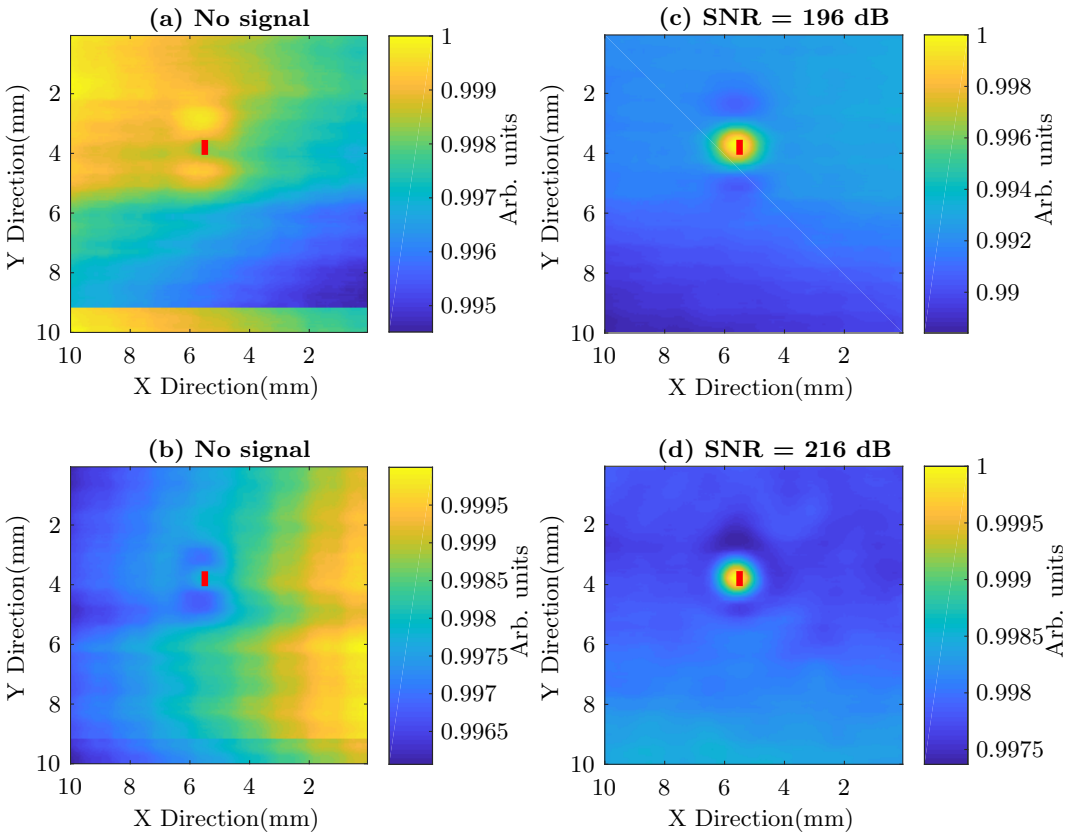

Figure 6.14: Initial C-scans generated from scanning for a 0.5 mm long defect in titanium. The absolute mode images (a and b) show vague indications of the defect, while the transmit-receive mode images show clear indications of the defect The trends in the data lead to inaccurate SNR evaluations, and the red bars represent the size and location of the 0.5 mm long defect on the titanium sample.

	SS - 0.25 mm		Ti - 0.25 mm		SS - 0.5 mm		Ti - 0.5 mm	
	Abs	T-R	Abs	T-R	Abs	T-R	Abs	T-R
Magnitude	41	77	62	98	55	82	64	96
Phase	23	82	52	98	54	92	56	96
Combined M&P	50	153	102	182	96	158	107	174
Combined A&T-R	183		256		216		235	

Table 6.3: Comparison of the SNRs in dB for the images after de-trending, with amplitude and phase combined, and with absolute mode, and transmit-receive mode data combined. The calculated SNRs from the scans of the 0.25 mm long and 0.5 mm long defects in stainless steel, and titanium are presented in this table, showing the comparatively higher sensitivity to sub-millimetre defects in titanium compared to stainless steel.

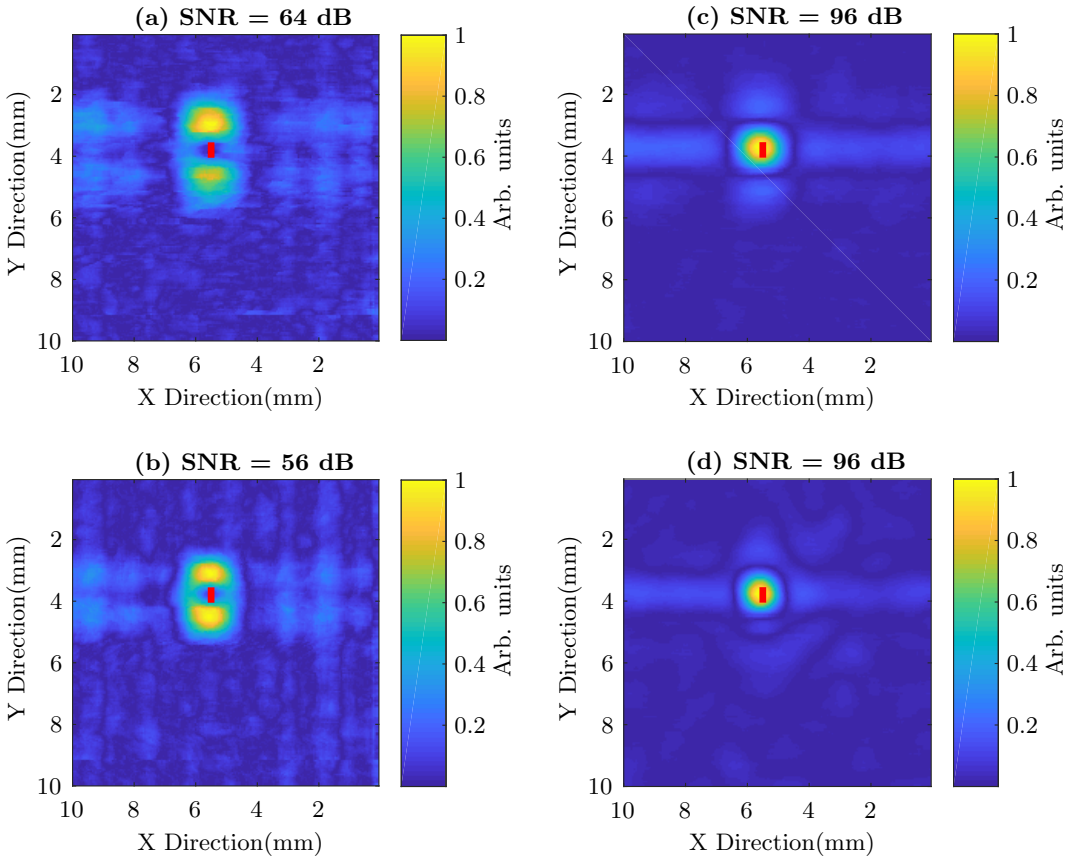

Figure 6.15: Images resulting from de-trending the initial C-scans from fig. 6.14 for the 0.5 mm long defect in titanium. The absolute mode images (a and b) now show clear indications of the defect with SNRs comparatively higher than the scans in stainless steel for the same defect size. The transmit-receive mode images (c and d) also show clear indications of the defect. Artefacts present in the images are a result of the de-rending process. The red bars identify the size, and location of the 0.5 mm long defect on the titanium sample.

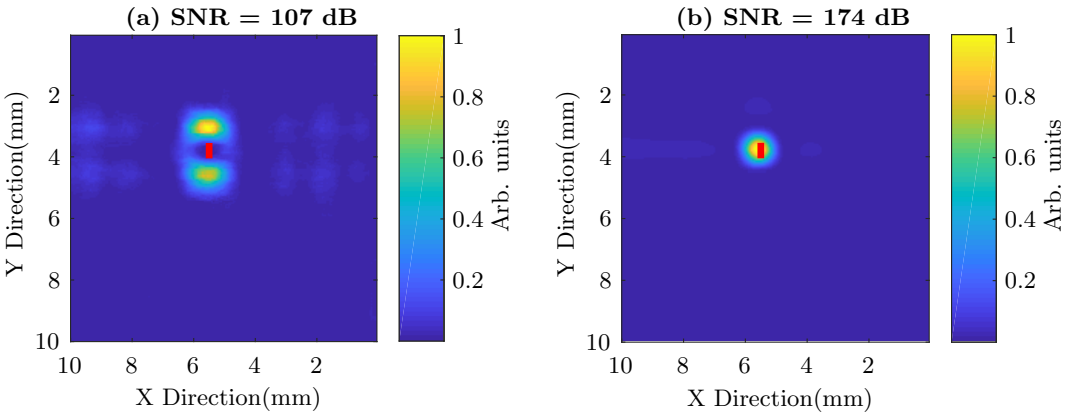

Figure 6.16: Images resulting from the combination of amplitude with phase for absolute mode data (a) and transmit-receive mode data (b). The defects are much more clearly indicated, with the background noise and de-trending artefacts almost completely suppressed. The red bars correspond to the size, and location of the 0.5 mm long defect on the titanium sample.

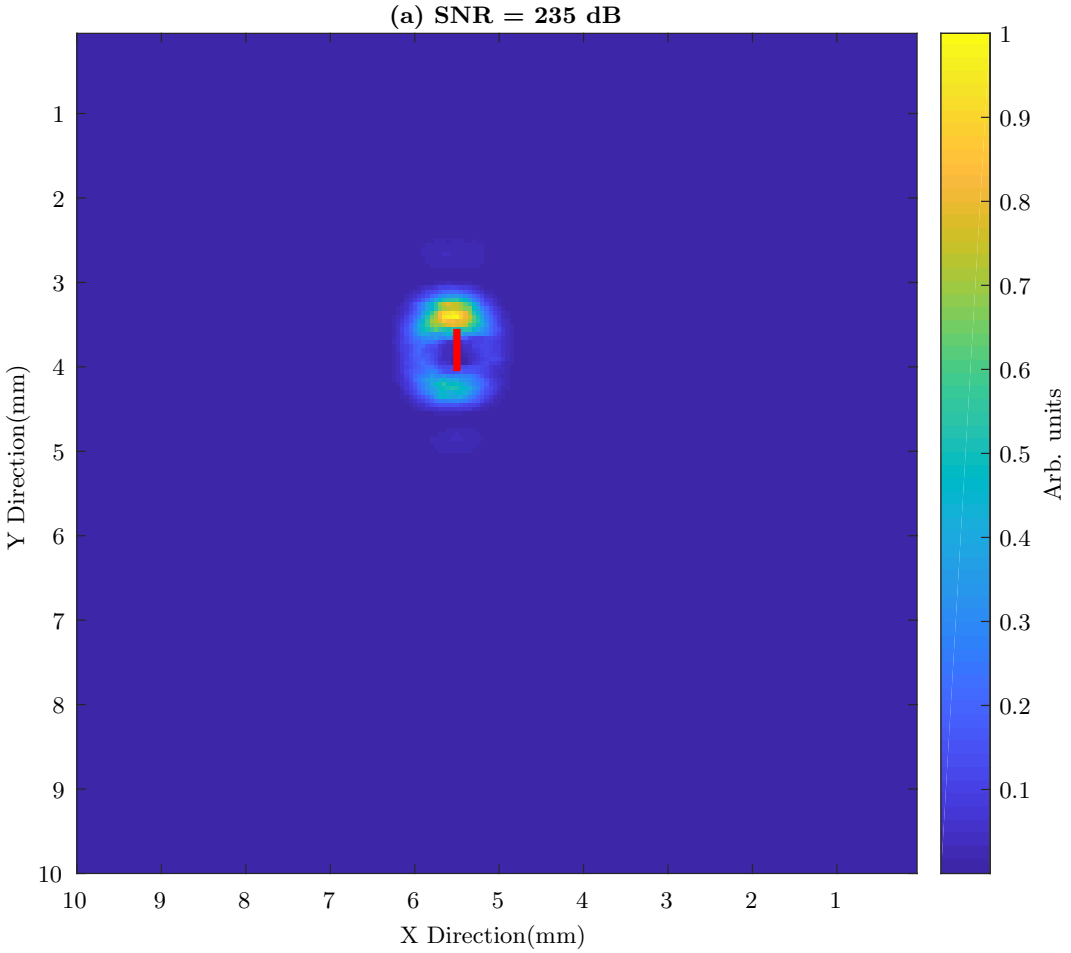

Figure 6.17: The resulting image when absolute mode data is combined with transmit-receive mode data for the 0.5mm long defect in titanium. The defect indication is clearly visible, and all background noise, and de-trending artefacts have been considerably suppressed. The red bar represents the size, and location of the 0.5 mm long defect on the titanium sample.

6.2 Scanning Multiple Defects in Titanium Aluminde (TiAl)

Alloys of titanium aluminide have recently been gaining considerable interest in the aerospace, and automotive industries for their desirable properties such as low density, high specific strength, and resistance to oxidation and creep at moderately high temperatures up to 750°C[141, 142]. Aerospace companies like Rolls Royce are considering using titanium aluminde in their gas turbine engine for its good performance at high temperatures, and lighter weight compared to the nickel alloys currently used. Some TiAl alloys however, are considered inferior to conventional titanium alloys on account of their low ductility and low fatigue strength[143, 144]. It is therefore imperative that small defects are detected in components made from this material, to prevent crack propagation, which could lead to component failure. The TiAl sample tested was provided by Dr David Hu from the University of Birmingham.

The Eddy Current Array System

An eddy current array (ECA) system, based on the EmbedEC board manufactured by EtherNDE was designed to be used for measuring defects of various lengths in a TiAl sample. The ECA system consists of a four element probe connected to two multiplexers, which switch between the coils. The multiplexers are connected to the EmbedEC, which energises the transmit coil, and measures the voltage across the receive coil. This system is an improvement on the one presented in fig. 4.1 as it replaces the function generator, Howland current source, and oscilloscope with the EmbedEC. However, with this system, absolute mode data can not be measured. Figure 6.18 presents a schematic diagram of the designed ECA system.

EmbedEC is a single channel, multi-frequency eddy current system capable of operating compatible probes in absolute and transmit receive modes. It contains two six-pin Lemo sockets, one for digital I/O communication, and the other for operating absolute or transmit-receive probes with compatible cables. It is capable of producing transmit currents up to 5 MHz, and thus, the operating frequency of 300 kHz used for experiments in this thesis is within its specifications. The EmbedEC is only capable of operating in absolute, or transmit-receive mode, and not both concurrently. Hence, based on the sensitivity of transmit-receive data as presented in previous sections, the ECA system was designed to operate the coil elements in transmit-receive mode. An ALL07-L04-015-EEC-R reflection probe cable from EtherNDE was used to connect the EmbedEC to the multiplexers, using a Lemo 0B

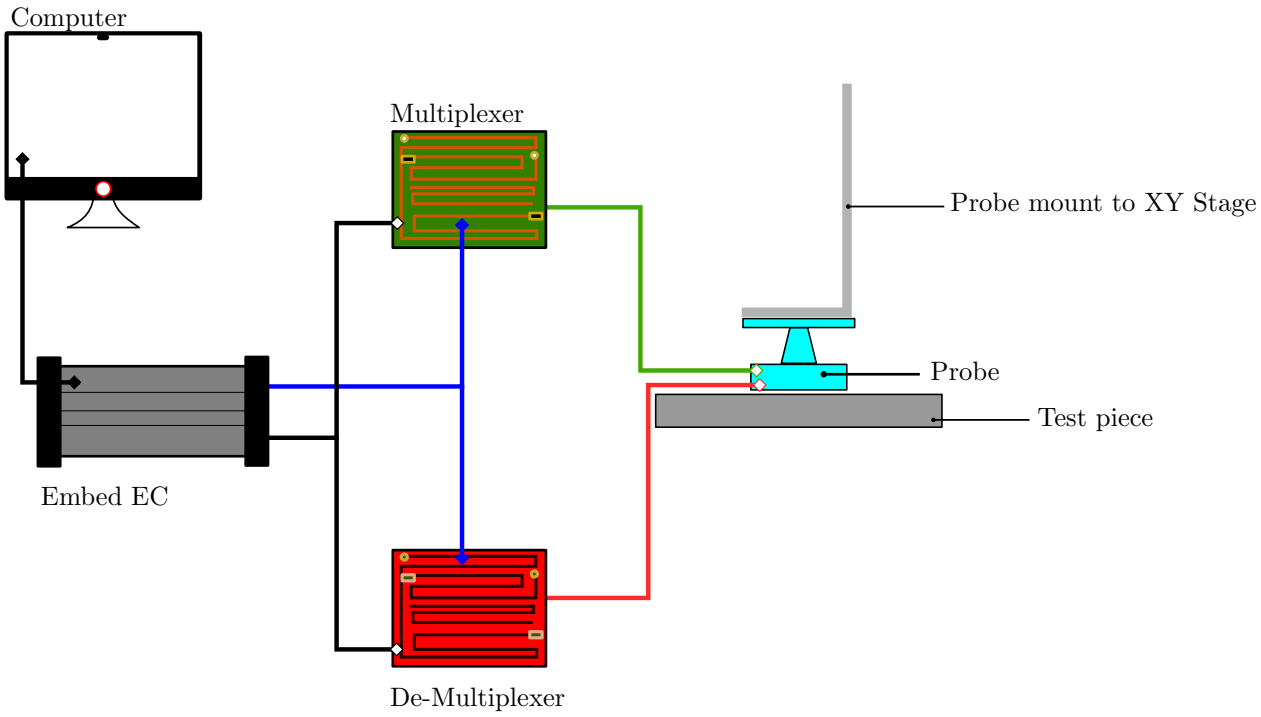

Figure 6.18: Schematic diagram of the designed ECA system. The computer controls the EmbedEC, which energises the transmit coil through the multiplexer, and measures the voltage across the receive coil through the de-multiplexer. The EmbedEC also also switches the multiplexer channels with a 6 pin digital I/O connector.

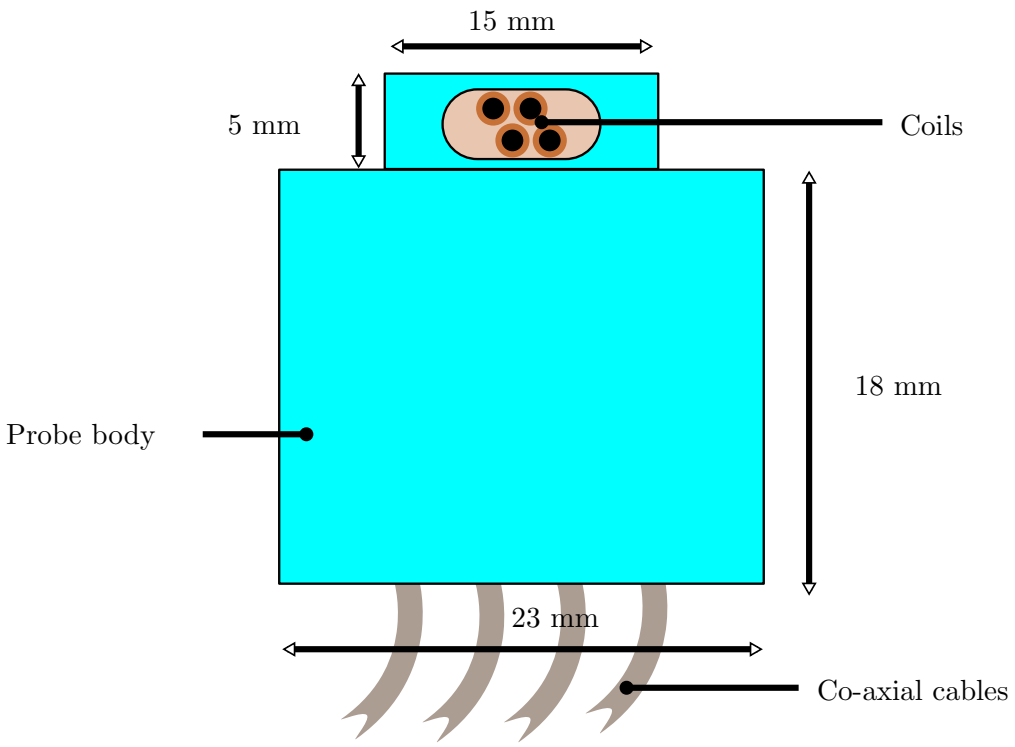

Figure 6.19: Illustration of the four element array probe designed for the ECA system. The coils are identical with internal, and external diameters of 0.9 mm, and 1.15 mm respectively, and heights of 1.58 mm. They each have 100 turns, distributed over four layers with 25 turns per layer, and contain ferrite cores with $\mu_r = 40$. The probe body is 3D printed from ABS plastic.

Series 4-pole socket with two pins connected to each multiplexer.

The multiplexers are ADG1607, 8 channel, differential multiplexers, with four channels of each connected to the four elements in the array probe. The 6-pin I/O socket from the EmbedEC switches the multiplexers, which are powered by a 8 V DC power supply. These multiplexers were selected for their high input impedance, and low output impedance ($\approx 4\Omega$)[145].

The probe is a four element array with the coils arranged as illustrated in fig. 6.19. The array contains four solenoid coils with internal, and external diameters of 0.9 mm, and 1.15 mm respectively, and heights of 1.58 mm. They each have 100 turns distributed over four layers with 25 turns per layer, and contain ferrite cores with $\mu_r = 40$. Each coil is connected to both the multiplexer and de-multiplexer via a 100 cm long, RG178 coaxial cable. The inductance of each coil and coaxial cable combined is 23 $\pm 3.5\mu$H at 300 kHz.

An impedance analysis for one of the coils is presented in fig. 6.20. It shows

Length (mm)	Depth (mm)	Width (mm)
2	1	0.1
1	0.5	0.1
0.5	0.25	0.1
0.25	0.125	0.1

Table 6.4: Dimensions of the defects laser micro-machined onto the surface of the titanium aluminide sample.

four resonance events occurring 2.3 MHz, 2.58 MHz, 2.75 MHz, and 3.35 MHz. These resonance events are attributed to the other coils resonating at these frequencies due to the magnetic flux coupling between them.

The EmbedEC is controlled by the computer using a program written in C#. Communications with the board, and retrieval of the measured voltage data is achieved via a DLL provided by EtherNDE, and data processing is performed using the Matlab IDE.

The test piece is an irregularly shaped piece of titanium aluminide (see fig. 6.21). The sample was corroded, and thus had to be ground to get a smooth surface onto which the defects were laser micro-machined. The dimensions of these defects are presented in table 6.4.

Tests performed with the EmbedEC ECA system were unsuccessful. This was due to the inability to gradually decrease the current from the board when it is turned off. While the board excited the coils, turning it off caused a large spike in the rate of change of the alternating current flowing through the coil. This led to a large back emf across the multiplexer terminals (eq. (2.5)), which burned the multiplexers. There was not enough time to work with EtherNDE to rectify the problem.

With the multiplexers rendered unusable, two coils in the ECA probe were connected directly to the EmbedEC to scan for the defects on the titanium aluminide sample in transmit-receive mode. The results from these scans are presented in the following section.

6.2.1 Results

$\gamma-$Titanium aluminide has a considerably lower conductivity compared to titanium (see table 6.1), and so the depth of penetration in this material is higher than in titanium at the same frequency. The shape of the sample, and the unevenness of the ground surface will influence the data from the EC measurements, and be reflected as trends in the background data of the images. These measurements were

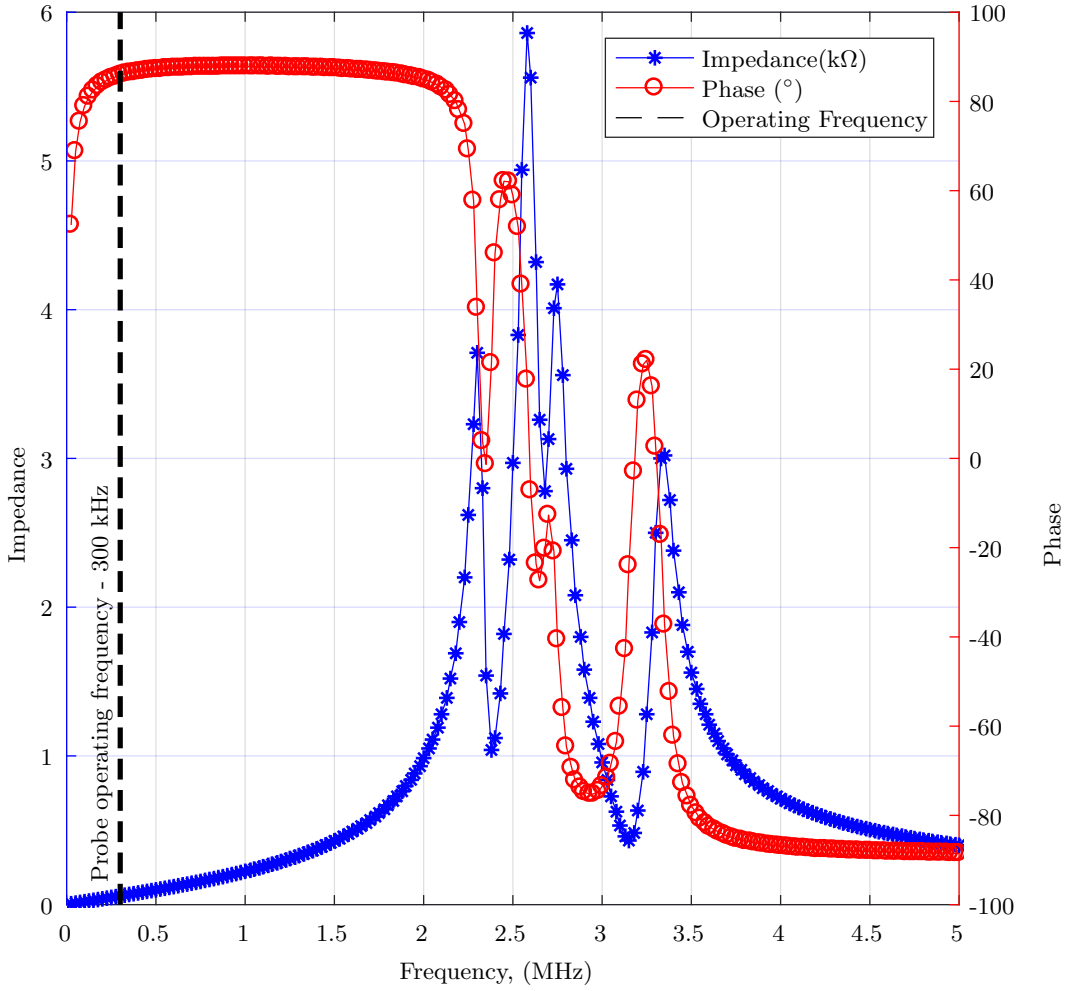

Figure 6.20: Impedance analysis of one of the array probe elements showing resonance at 2.3 MHz, 2.58 MHz, 2.75 MHz, and 3.35 MHz. These resonance frequencies are contributed by the other coils due to the magnetic flux coupling between them. The dashed line corresponds to the operating frequency of the probe.

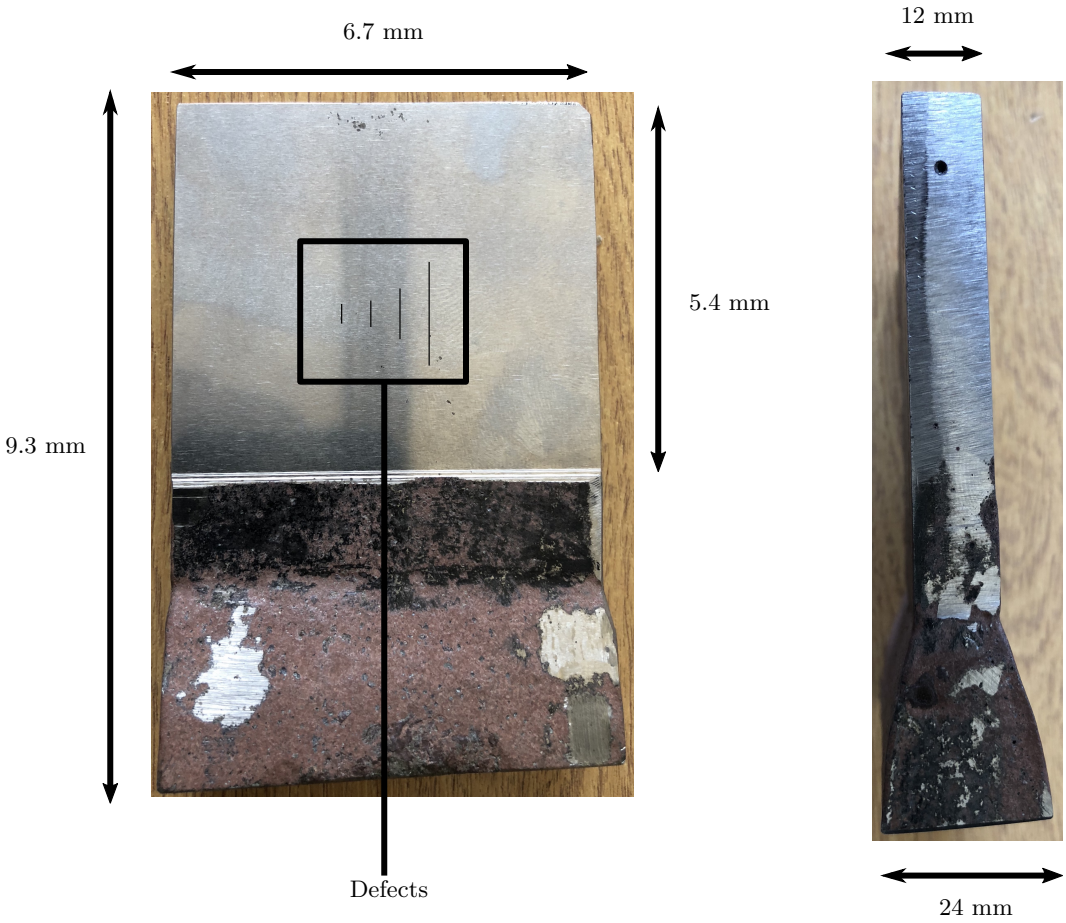

Figure 6.21: Picture of the titanium aluminide sample showing its dimensions. Four defects with dimensions presented in table 6.4 have been laser micro-machined onto its surface. The sample was corroded, and had to be ground to get the smooth surface.

performed at 300 kHz.

The sinusoidal wave voltage across the receive coil is measured, and resolved to its X and Y components before transmission from the EmbedEC. These values are then used in evaluating the magnitude, and phase values for the C-scan images. Magnitude values are calculated using eq. (6.1), and phase values are calculated using eq. (6.2). The signal to noise ratio (SNR) of the images are evaluated using the method discussed in chapter 4. The threshold for SNR calculation is defined as a cluster of pixels with intensities higher than 5 times the standard deviation of the image.

$$\text{Magnitude} = \sqrt{a^2 + b^2} \tag{6.1}$$

$$\text{Phase} = \tan^{-1} \frac{b}{a} \tag{6.2}$$

2mm long defect

A 10 mm $\times$ 10 mm area around the 2 mm long defect was scanned using two adjacent coils within the ECA probe and the EmbedEC. The scan step size is 0.1 mm, which results in a 100 pixel x 100 pixel grid. The resolved magnitude, and phase data using the values from the board without post processing is presented in fig. 6.22. Due to the way it was used, random noise spikes were present in the data measured from the adapted EmbedEC system. These noise spikes have extremely high values, and suppress the pixel intensities in areas of interest. The defect indication is invisible in the magnitude image fig. 6.22 (a), and barely visible in the phase image fig. 6.22 (b). The values from these spikes completely overshadow the actual eddy current measurement data, and thus the utility of an applied median filter is demonstrated in fig. 6.23.

The application of a median filter gets rid of the random noise spikes, and increases the visibility of the 2 mm long defect in both the magnitude image fig. 6.23 (a), and phase image fig. 6.23 (b).

The size of this defect relative to the size of the coils results in a higher intensity for the defect indication compared to smaller defects. This means that variational trends in the data due to the unevenness of the sample are less visible. However, these trends are present, and de-trending the data only improves it. It is also important to de-trend the data if the images are to be combined, so that the combined images have the same baseline. Figure 6.24 presents the images from fig. 6.23, but with the trends removed.

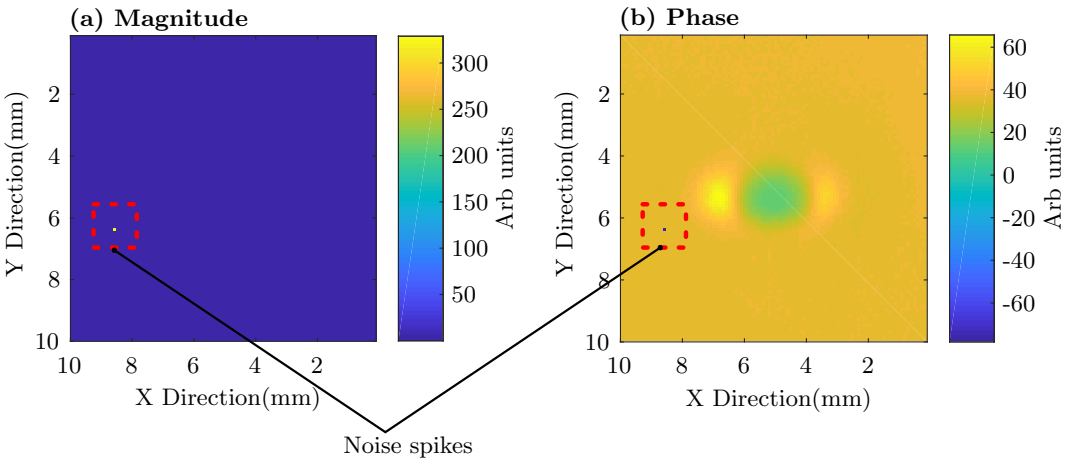

Figure 6.22: C-scans of a 2 mm long defect in a titanium aluminide test piece. These images are created with data from the EmbedEC without any post processing. The EmbedEC transmits real, and imaginary components of voltage, which are then resolved to create the (a) magnitude C-scan image, and (b) phase C-scan image.

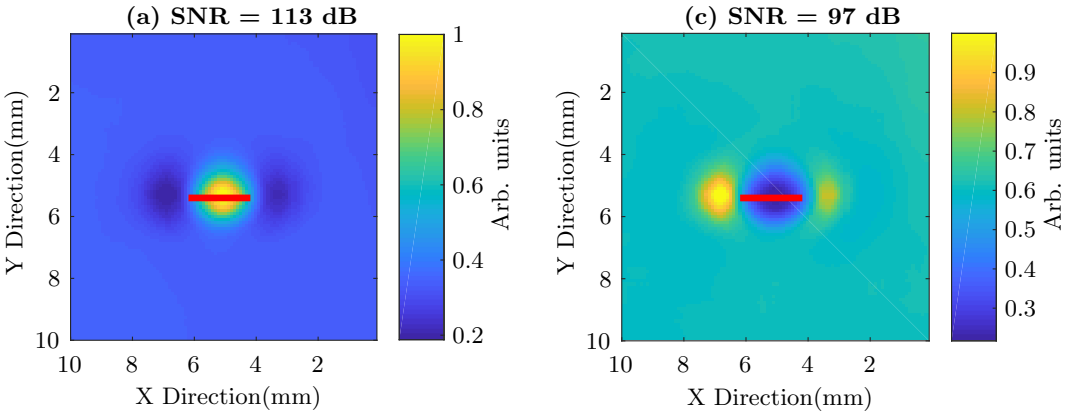

Figure 6.23: Median filtered C-scans of a 2 mm long defect in the titanium aluminide sample. The median filter removes the noise spikes, thus revealing the defect indication. (a) The magnitude C-scan, and (b) the phase C-scan. The red bars represent the size, and location of the 2 mm long defect.

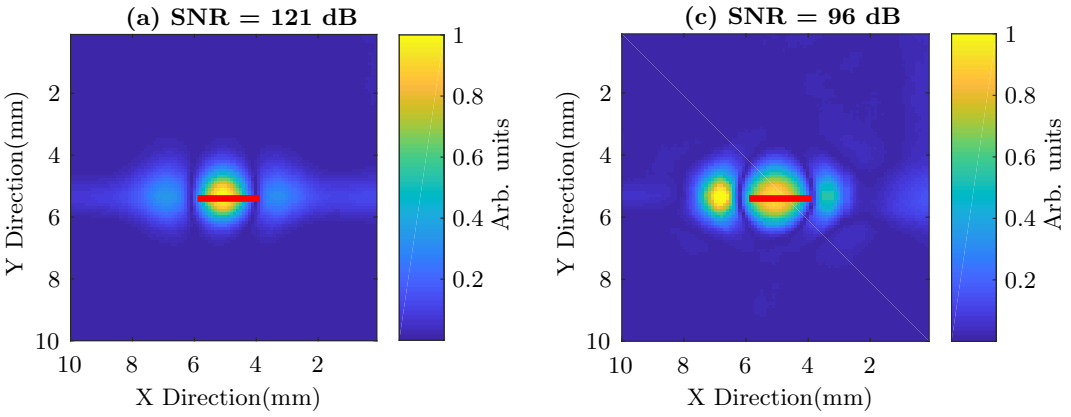

Figure 6.24: De-trended C-scans of the 2 mm long defect in the titanium aluminide test piece. Removing the trends improves the visibility of the defect indication, and enables the combination of the magnitude image (a), with the phase image (b). The red bars correspond to the size, and location of the 2 mm long defect.

With the trends removed, the SNR in the magnitude data (fig. 6.24 (a)) is improved, while that in the phase data (fig. 6.24 (b)) is unchanged. The artefacts resulting from the trend removal is present in both images. However, both images have a common baseline, and can be combined to produce a single image with a considerably higher SNR which also suppresses the background noise and the artefacts from the trend removal process. Figure 6.25 resents the resulting image from combining the magnitude image, with the phase image fig. 6.24 (a x b). This image has a significantly higher SNR compared to the individual de-trended images, and the high intensity of the defect indication almost entirely suppresses the de-trending artefacts.

1 mm long defect

A scan of a 1 mm long defect in the titanium aluminide sample produced the images presented in fig. 6.26. A median filter has been applied to these images to eliminate the random noise spikes. It can observed that the SNRs for both the magnitude data fig. 6.26 (a), and the phase data fig. 6.26 (b) are less, compared to the images for the 2 mm long defect. The lower signal intensity for this defect due to its size, results in the variational trends being more pronounced in the images. These trends are there due to the sample surface being uneven and not flat. The trends however, do not affect the actual defect signal, and thus have no influence on the evaluated initial SNR values.

Removing the trends in fig. 6.26 results in an improved image, albeit with

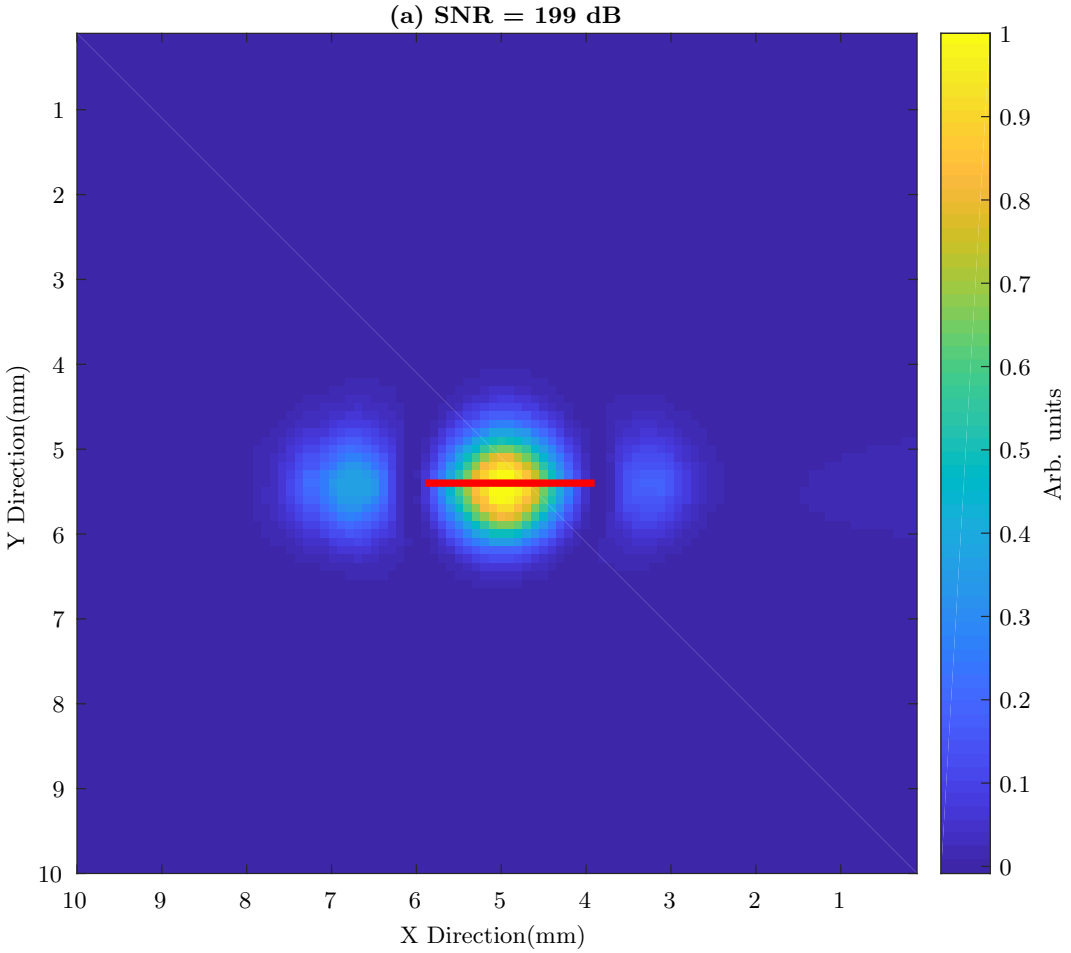

Figure 6.25: Image resulting from combining magnitude data with phase data. This image has a significantly improved signal to noise ratio, and defect indications that are high enough to suppress the artefacts introduced into the data during de-trending. The red bar highlights the size, and location of the 2 mm long defect on the titanium aluminide test piece.

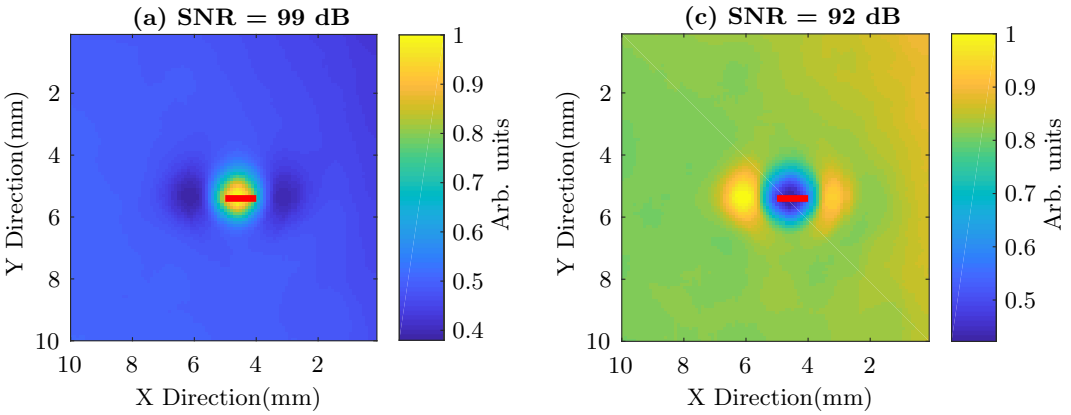

Figure 6.26: Median filtered C-scans of a 1 mm long defect in the titanium aluminide sample. The calculated SNR values are lower compared to the larger 2mm long defect, and the lower intensity of the defect indication allows for the visibility of the trends present in the background data due to the unevenness of the sample. The red bars represent the size, and location of the 1 mm long defect.

artefacts introduced, as shown in fig. 6.27. These images have improved SNRs, and some variation in the actual background data of the sample are visible. Combining magnitude with phase (fig. 6.27 (a × b)) results in the image presented in fig. 6.28. Here the SNR is significantly improved, and the de-trending artefacts are suppressed.

0.5 mm long defect

Performing the scans of a 0.5 mm long defect in the sample results in the images presented in fig. 6.29. The signal intensity for this defect is lower, hence the trends in the data are more pronounced. The trends are more visible in the phase image, fig. 6.29 (b) than the magnitude image fig. 6.29 (a).

Removing these trends however, results in a considerably improved image with higher SNR as shown in fig. 6.30. Combining the magnitude image with the phase image fig. 6.30 (a x b) results in a single image with significantly improved SNR as shown in fig. 6.31.

0.25 mm long defect

The 0.25 mm long defect was the smallest defect scanned, and the initial magnitude, and phase images with median filters applied are presented in fig. 6.32. The defect signal intensity is relatively low, and thus it does not reach the required threshold for SNR calculation in the magnitude image fig. 6.32 (a). The low defect signal intensity also allows for more visible trending variations in the background data.

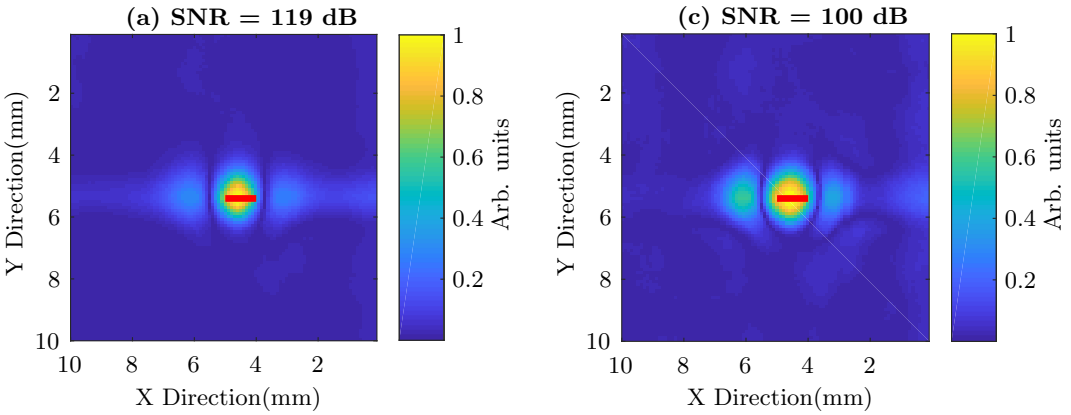

Figure 6.27: De-trended C-scans of a 1 mm long defect in the titanium aluminide test piece. These images have improved SNRs compared to the originals, and are in a format that enables them to be combined. The red bars represent the size, and location of the 1 mm long defect.

Defect Length	2 mm	1 mm	0.5 mm	0.25 mm
Magnitude	121	119	108	79
Phase	96	100	98	85
Combined M&P	199	198	186	145

Table 6.5: Comparison of the SNRs in dB for the C-scan images of the defects tested in titanium aluminide. The SNR decreases as the defect gets smaller.

These trends have been present in all the data presented thus far, however, data with relatively high defect signal intensities tend to hide the trends.

Removing the trends from the images in fig. 6.32 produces the images in fig. 6.33. Here the background noise is decreased in the magnitude image enabling it to meet the specified threshold for the SNR calculation. As expected, the SNR for the image is low, relative to the larger defect sizes, however, the defect indication is clear and visible. The calculated SNR for the phase image fig. 6.33 (b) is lower than the original, and this is because of the high intensity pixel values in the background due to the trends in the data.

Combining magnitude data with phase data fig. 6.33 (a $\times$ b), the single image generated has a much higher SNR compared with the originals, and the de-trending artefacts are suppressed as shown in fig. 6.34. A comparison for the calculated SNR values for all the defects sizes scanned in the titanium aluminide sample is presented in table 6.4. The SNR values for the defect images are high, but decrease as the defect becomes smaller.

The titanium aluminide experiments were performed with a different probe

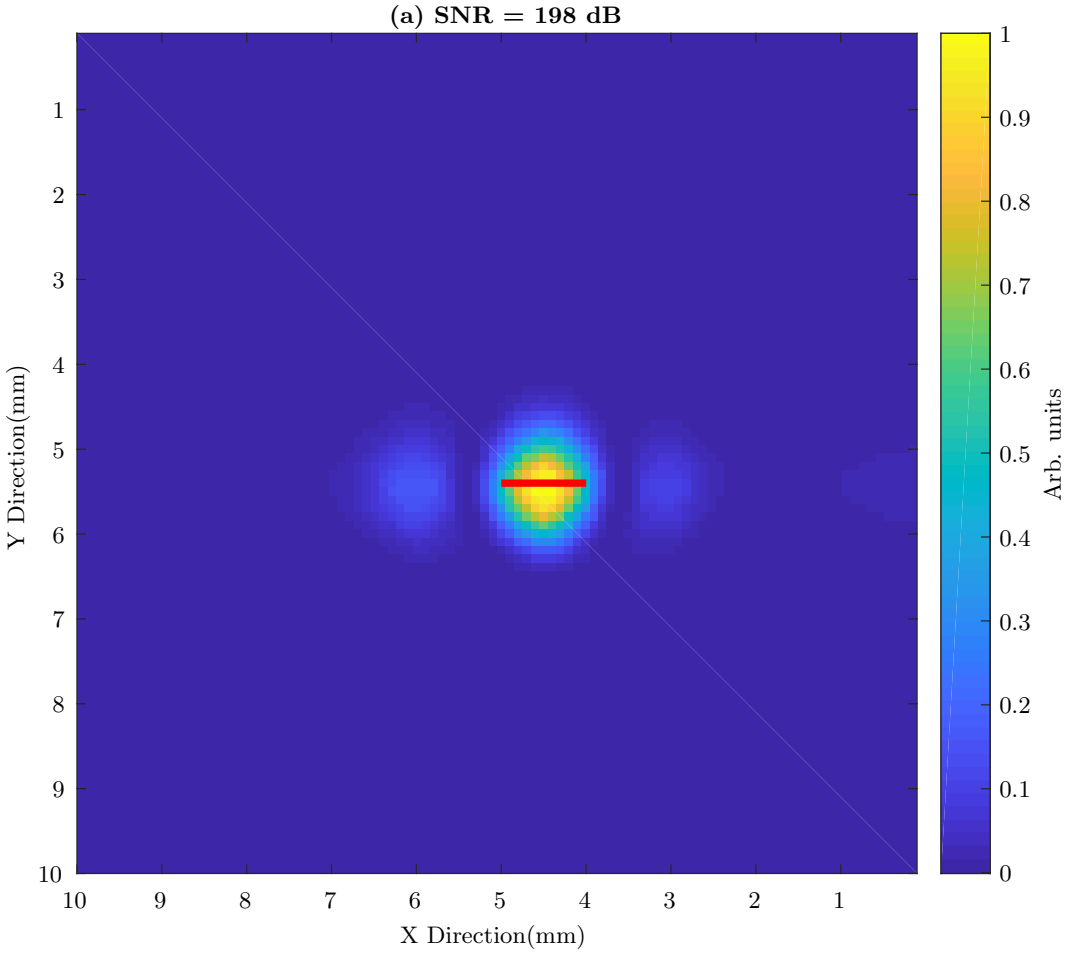

Figure 6.28: Single image resulting from the multiplication of the magnitude C-scan with the phase C-scan of a 1 mm long defect in the titanium aluminide sample. The image has a significantly improved SNR, and high pixel intensities for the defect indication. The red bar corresponds to the size, and location of the 1 mm long defect.

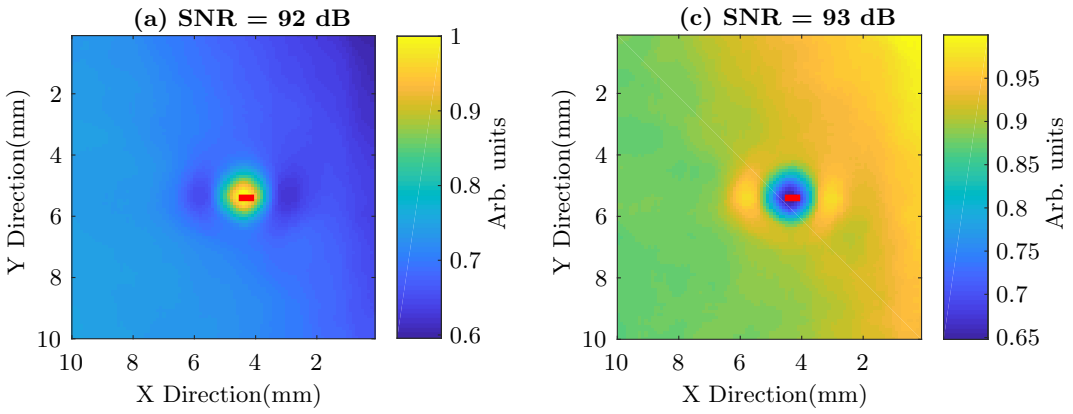

Figure 6.29: C-scans of a 0.5 mm long defect in the titanium aluminide sample. The trends in the data are more visible due to the lower intensities of the pixels representing the defect indication. The red bars correspond to the size, and location of the 0.5 mm long defect.

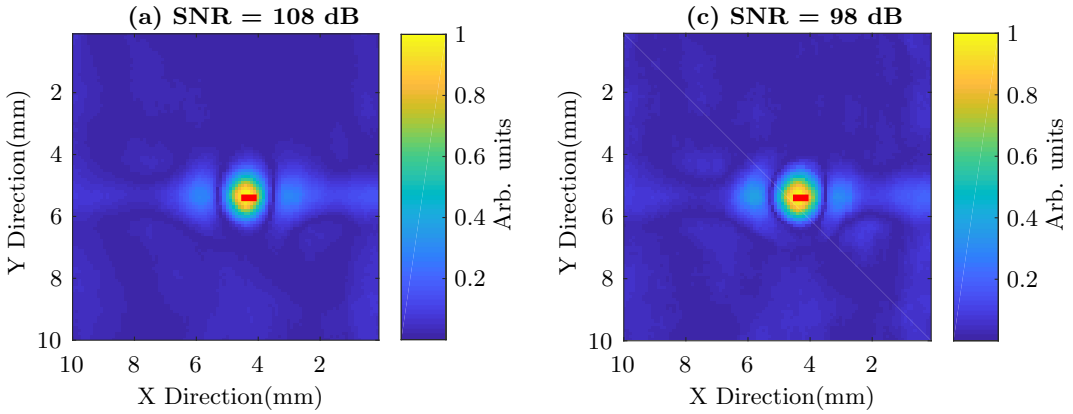

Figure 6.30: C-scans of a 0.5 mm long defect in the titanium aluminide sample with the trends removed. The red bars correspond to the size, and location of the 0.5 mm long defect.

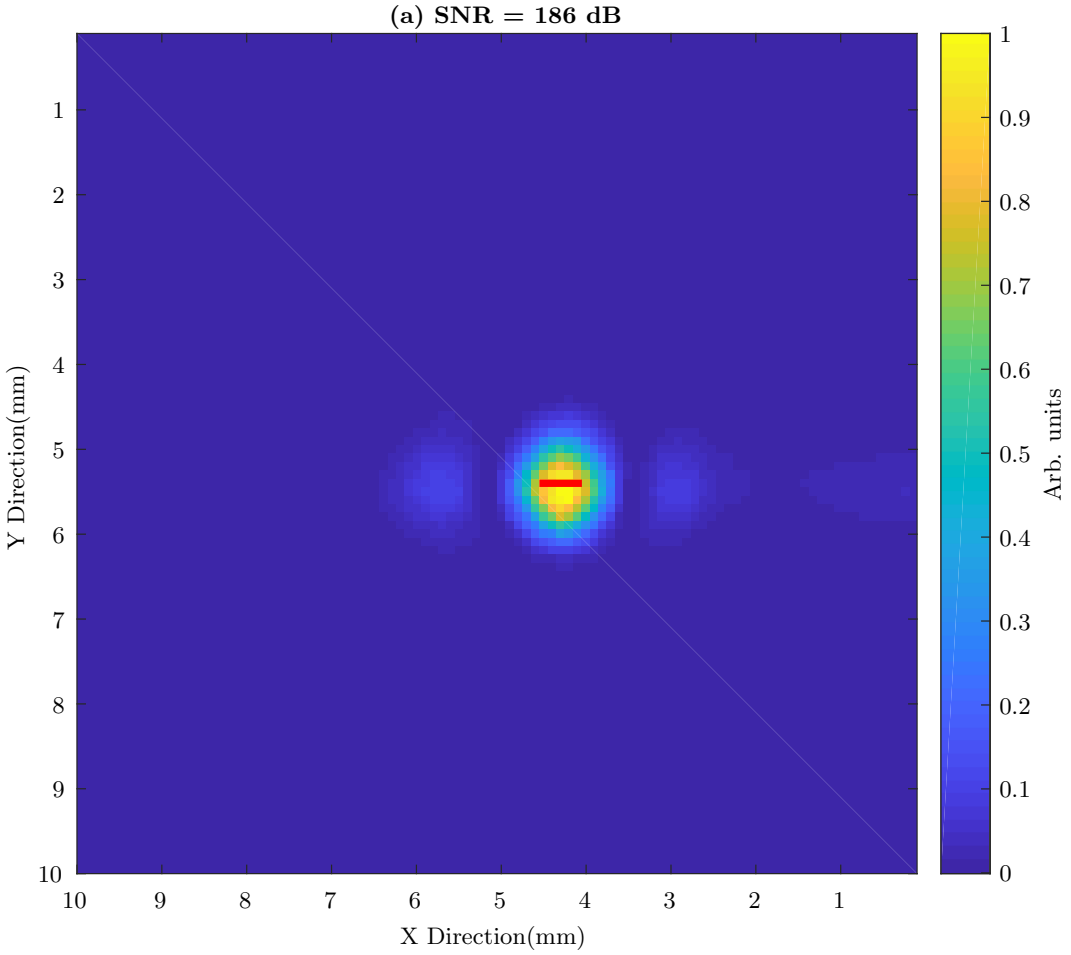

Figure 6.31: The resulting image from multiplying the magnitude C-scan with the phase C-scan of the 0.5 mm long defect in the titanium aluminide sample. The red bar represents the size, and location of the 0.5 mm long defect.

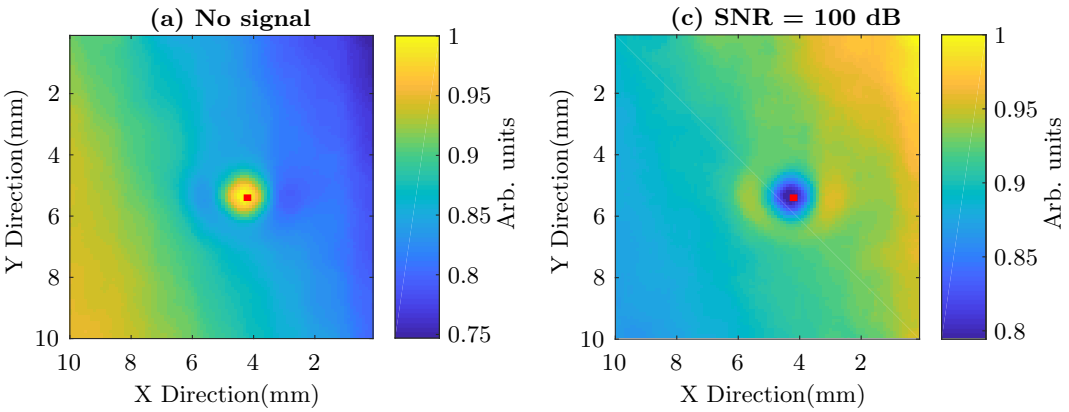

Figure 6.32: C-scan of a 0.25 mm long defect on the titanium aluminide test piece. The trends due to the uneven sample surface are much more visible now, and the pixel intensities for the defect indication in the magnitude image (a) is lower than 5 times the image standard deviation. Thus the SNR is not calculated in this instance. The SNR calculated in the phase image (b) is also inaccurate due to the program identifying parts of the trends as clusters of high intensity pixels. The red bars correspond to the size, and location of the 0.25 mm long defect.

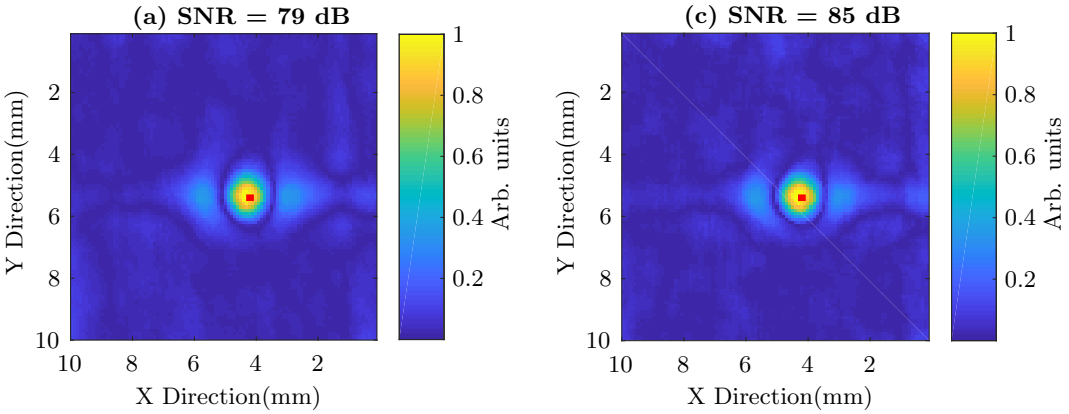

Figure 6.33: The C-scans of a 0.25 mm long defect in a titanium aluminide sample after background trends have been removed. The defect indication is more visible in both images, however the calculated SNRs are low compared to the those for the larger defects. The red bars correspond to the size, and location of the 0.25 mm long defect.

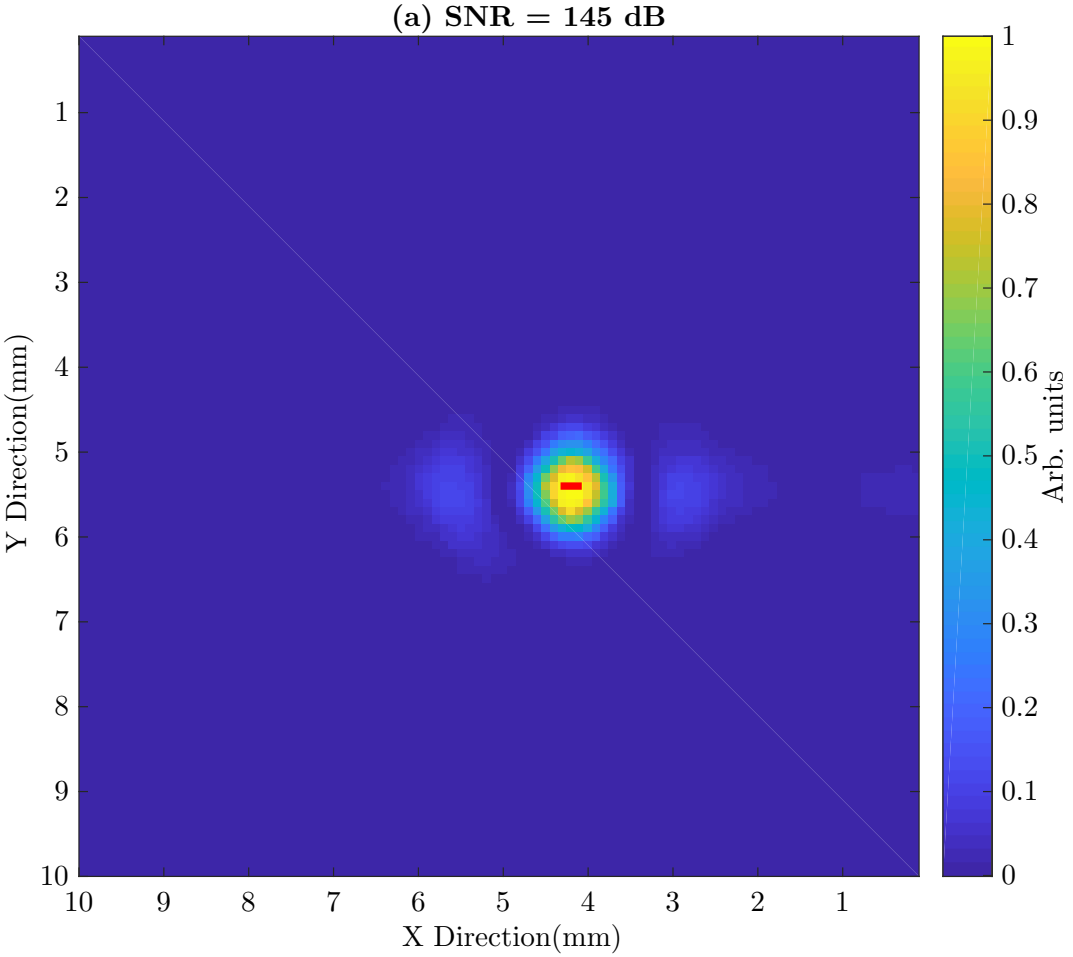

Figure 6.34: Image resulting from the combination of the magnitude, and phase C-scans of the 0.25 mm long defect on the titanium aluminide test piece. The SNR is much higher than the individual C-scans, and the defect signal pixel intensities are high enough to suppress the artefacts introduced to the C-scans during the detrending process. The red bar represents the size, and location of the 0.25 mm long defect.

Material	SS - 0.25 mm	Ti - 0.25 mm	TiAl - 0.25 mm
Magnitude	77	98	79
Phase	82	92	85
Combined M&P	153	182	145

Table 6.6: Comparison of the SNRs in dB for the 0.25 mm long defect scans on stainless steel, titanium, and titanium aluminide, for transmit-receive data. The SNRs are highest in the titanium sample, with the stainless steel, and titanium aluminide samples performing similarly.

Material	SS - 0.5 mm	Ti - 0.5 mm	TiAl - 0.5 mm
Magnitude	82	96	108
Phase	92	96	98
Combined M&P	158	174	186

Table 6.7: Comparison of the SNRs in dB for the 0.5 mm long defect measurements in stainless steel, titanium, and titanium aluminide. Only transmit-receive mode data is compared, and here the SNR in titanium aluminide is highest, while that in stainless steel is lowest.

from that used for the experiments on stainless steel and titanium. Comparing the SNR values for the defect measurements in the three materials tested, titanium aluminide performed similarly to stainless steel for the 0.25 mm long defect, and they both performed worse than titanium as shown in table 6.6. For the 0.5 mm long defect, the SNR was highest for the titanium aluminide sample, and lowest in the stainless steel sample as shown in table 6.7.

6.3 Summary

This chapter presents the work done in detecting sub-millimetre defects using a sub-MHz excitation current. The two-coil experimental set-up was used to scan 0.25 mm long, and 0.5 mm long defects in stainless steel and titanium. Both of these materials have low conductivities, hence the depth of penetration of eddy currents into the material is higher than for high conductivity materials at a given frequency.

High frequency excitation currents are often used for the detection of sub-millimetre defects, but it is shown in this chapter that with some image processing, defects as small as 0.25 mm long can be detected in stainless steel, titanium, and titanium aluminide. Sizing the defect is dependent on the coil footprint relative to the defect size, and as these coils have diameters larger than the defects tested, they can be used to accurately detect, and locate the small defects, but not reliably size them. The experiments showed that, while they have similar conductivities, the

SNR for the C-scans in titanium were consistently higher than those for stainless steel for both defect sizes tested.

The design of a eddy current array system based on an EmbedEC board manufactured by EtherNDE was presented. The ECA system consists of the EmbedEC board controlled by a computer, and connected to two multiplexers, which switch between the coils in a four element array probe. Tests done with this system were unsuccessful due to issues with the multiplexers getting burned by sudden spikes in the rate of change of alternating current.

Two adjacent coils in the ECA probe were connected directly to the EmbedEC board to perform tests on a titanium aluminide sample in transit-receive mode. The titanium aluminide sample has an irregular shape, and was corroded. One side of the sample had to be ground to get a smooth enough surface for defects to be laser micro-machined onto the sample. Tests were done on defects that are 2 mm long, 1mm long, 0.5 mm long, and 0.25 mm long. The tests showed that the SNR of the C-scans decreased as the defects got shorter. The unevenness of the ground sample was also apparent in the data in the form of trending variations in the background, but showed more influence in the C-scans for the shorter defects. Removing those trends improved the SNR of all the C-scans, and enabled the combination of magnitude data with phase data to generate images with a significantly improved SNR. The de-trending process introduces artefacts into the background of the C-scans, and it was shown that data combination increased the defect indication pixel intensity enough to suppress the artefacts introduced in the background.

Comparisons were made between the SNRs for the sub-millimetre defect C-scans in the titanium, stainless steel, and titanium aluminide samples. It was observed that the SNRs were consistently lowest in the stainless steel sample for both defect sizes tested. For the 0.25 mm long defect, the titanium sample performed best, while for the 0.5 mm long defect the titanium aluminide sample performed best.

It should be noted that the experiments conducted in this chapter, and chapter 4 considered defects, which were oriented parallel to the axis of separation of the coils. The coil response is different when the defect is oriented perpendicular to the axis of separation of the coils as discusses in chapter 5. Further work should be conducted to investigate the effect of this orientation on the coil responses.

Chapter 7

Conclusion & Future Work

This thesis investigated the potential for using eddy current inspection for the detection of sub-millimetre defects in low conductivity materials including; titanium, stainless steel, and titanium aluminide. The eddy current probes were excited at a high enough frequency that provided a sufficiently small skin depth, but low enough to not be strongly affected by the electrical properties of the cables connected. Surface inspections on these materials can be problematic for ECT measurements in part due to their low conductivities, and thus much higher frequency current excitation is more often applied to the inspection of these materials in industry. This thesis therefore explored the interaction of eddy current probe coils with these materials, in a bid to improve the sensitivity of eddy current imaging of defects in these materials, and with the ultimate aim of improving the reliability of eddy current arrays.

7.1 Thesis Review

The critical findings in this thesis are summarised below.

7.1.1 Eddy Current Modelling

Before attempting to investigate methods of improving eddy current probe sensitivity, it was important to understand the fundamental operation of eddy current probe coils. Finite element models were created to enable the visualisation of magnetic field interactions between probe coils, and the specimen. Initial models are presented, which compared the finite element modelling technique used with the tried and tested equations derived by Dodd and Deeds, modelled analytically using MATLAB. Agreement between the analytical and FE models, and the experiments

validated the technique.

The fundamental composition of an eddy current array is a pair of coils, thus extensive models of a coil pair scanning various materials, with different defect sizes were created. The modelled coils were similar to the coils used for the experiments, and operating at the same modes, so that the data retrieved from the modelling could be used in both understanding, and validating the experimental data.

The models showed that when the coil is driven in absolute mode, the defect indications in the scans corresponded to the edges of the defect, hence absolute mode data could be used to size defects bigger than the sensing coil diameter. The coil driven in transmit-receive mode always showed an indication that was symmetric along the length of the defect, which was interpreted to mean that the peak of defect indications in transmit-receive mode always determined the centre location of the defect, for the range of defects tested in this thesis.

The models also showed that when the coil voltage was measured, the parametric measurements of amplitude, and phase of the sinusoidal coil voltage were both affected by the presence of the defects, but in different ways. This means that amplitude data can be combined with phase data to improve the SNR in s C-scan, and increase PoD.

Absolute mode data was observed to have a constant spatial shift with respect to transmit-receive data. This means that for an array probe with multiple elements operated in both absolute, and transmit-receive modes, the shift in data could be compensated for, and the data combined to further improve the overall signal to noise ratio.

Coil models with air cores were compared to those with ferrite cores, and it was shown from the models, that the ferrite core significantly improved coil sensitivity. However, the presence of a core in the receive coil also changed the shape of absolute mode data, showing a higher amplitude when the edge of the transmit coil closest to the cored receive coil was at the edge of a defect.

The orientation of the defect with respect to the axial separation of the coils was shown to have an effect on the coil voltage responses. It was shown that the voltage magnitude, and phase across the receive coil was the same, irrespective of which coil was scanning over the surface of the defect. The implication of this is that the coil pair can not only detect, and size the defect, but can also provide insight into the surface orientation of the defect. From the models, it was shown that defects smaller than the coil diameter could be detected, however sizing them is difficult.

7.1.2 Improving the Signal to Noise Ratio of Eddy Current C-scans

Experiments were conducted using a pair of coils to generate C-scan images of a surface breaking defect in a stainless steel sample. The defect considered in this experiment is 2 mm long, 1 mm deep, and 0.06 mm wide. The magnitude, and phase of the voltage across the coils were measured, and used to generate the C-scan images. The images showed consistently better SNR in transmit-receive mode data when compared to absolute mode data also highlighting the higher susceptibility of absolute mode measurements to lift-off variations.

The experiments were conducted using an excitation frequency of 300 kHz. At this frequency, the impedance of the coils used was 49.4 Ω, which matched them to the 50 Ω impedance of the other components within the experimental set-up. At this frequency, the data was less affected by destructive factors such as parasitic capacitance between the coil turns, and coil resonance. This is also much less than the frequency used conventionally in eddy current measurements of low conductivity material, and the detection of defects in these materials at this frequency is a significant improvement to eddy current testing.

A constant current source was utilised in the experiments. This device enabled the use of a constant amplitude sinusoidal wave drive current in the transmit coil. With this current, the voltage across the coil is changes linearly with the impedance of the coil, and enabling easier analysis, and comparison to the finite element models.

It was shown, that combining the magnitude images with the phase images by multiplication always led to a significant improvement in SNR compared with the individual images. Using the parameters for calculating the shift between transmit, and receive coil voltages derived from the models, the shift in the experimental data images were compensated for, and the images combined by multiplication.

The resulting image consistently had a considerably improved SNR. The initial SNR in the experiments was high, and thus analysis was performed by adding varying levels of artificial Gaussian noise to the images, combining them, and attempting to recover them. This analysis gave insight to the limits of initial SNR, to which a defect indication could be reliably recovered.

This method of data processing is novel, and has not been presented anywhere else. It shows the potential for improving defect signal to noise ratio, using a combination of magnitude and phase data, and absolute and transmit-receive data.

7.1.3 Detecting Sub-Millimetre Defects Using Low Frequency Eddy Currents

The conductivity of the material being tested is an important parameter when determining the frequency at which sub-millimetre defect inspections are performed. The frequency of excitation determines the depth to which eddy currents will penetrate, and by extension the sensitivity of the sensing coils to the induced eddy currents. High frequency measurements are not without their challenges however, as the coils used tend to have air cores, and fewer turns, which decreases their effective inductances, and consequently their sensitivity. In addition, at higher frequencies, the electrical properties of the connected cables begin to have more pronounced effects on the coil inductance.

These experiments were to be performed using a four element eddy current array probe built to work with the EmbedEC system manufactured by EtherNDE. However, due to technical difficulties, the probe could not be used as an array with the EmbedEC, due to the way it was adapted. The probe was instead connected directly to the EmbedEC, using two adjacent coils operated in transmit-receive mode - a subset of the array probe. Measurements of sub-millimetre defects in stainless steel, titanium, and titanium aluminide were performed using this set-up. The defects have the following dimensions:

Titanium aluminide

- 2 mm long, 1 mm deep, 0.1 mm wide
- 1 mm long, 0.5 mm deep, 0.1 mm wide

Stainless steel, titanium, and titanium aluminide

- 0.5 mm long, 0.25 mm deep, 0.1 mm wide
- 0.25 mm long, 0.125 mm deep, 0.1 mm wide

The measurements in stainless steel, and titanium were performed using the same coil pair probe used in chapter 4, while the experiments on the titanium aluminide sample were performed using the EmbedEC, and the two adjacent coils in the array probe. For the sub-millimetre defects in stainless steel, and titanium, the defects were consistently invisible in initial C-scans for absolute mode data, and just barely visible in transmit receive data. Data processing by applying a median filter, and de-trending before combining the images as presented, consistently revealed all the defects, bringing the conclusion that defects as small as 0.25 mm long can be reliably detected at this frequency, using this method.

The experiments on titanium aluminide using the EmbedEC system always revealed the defects when a median filter is applied to the data straight from the system. It was observed that the variational trends in background data became more visible as the defect got smaller, which was attributed to the defect signal getting less intense with the decreasing defect size. In every case, de-trending the data, and combining, significantly improved the visibility of the defects, and SNR of the images across the range, even down to the 0.25 mm long defect. It was concluded that defects as small as 0.25 mm long were also detectable in titanium aluminide, using this method at this frequency.

The performance of the various materials was compared by comparing the calculated SNRs from the C-scan images. The conclusion derived from this is that, while the defects were all detected, stainless steel performed the worst for both sub-millimetre defects, with titanium performing the best for the detection of the 0.25 long mm defect, and titanium aluminide performing the best for the 0.5 mm long defect.

The ability to detect such small defects in low conductivity materials such as these using an excitation frequency as low as 300 kHz is a major improvement in eddy current testing. Conventionally eddy current measurements of low conductivity materials are performed using frequencies higher than 1 MHz, however, these instruments require more complex electronics to function properly. Array systems are generally not used for the inspection of low conductivity materials as the electronics required for this are complex. Incorporating the methods discussed in this thesis will vastly optimise any eddy current array system, and enable to the inspection, and imaging of sub-millimetre defects in low conductivity materials using eddy current arrays.

7.1.4 Future Work

There were many intriguing and thought provoking developments documented in this thesis, that warrant further investigation. This research predominantly analysed the effectiveness, and limitations of the main modes of operation of eddy current coils in an eddy current array for the detection of sub-millimetre defects in low conductivity materials. Eddy current array data is mainly presented in the form of images, and the work done has shown the appearance and initial analysis of the data that can be retrieved from an array with the coils operated in either absolute, or transmit receive mode. It has also been shown that the reliability of the data can be significantly improved by combining the images to increase the SNR.

Data collection using the experimental set-up presented in chapter 4 was a

very slow process using Labview, and a slightly faster process when Matlab was used. It was fastest when the EmbedEC system was used due to the system's ability to take thousands of measurements per second. When testing for defects smaller than the coil diameter, it is important that the resolution of the scan is small enough so that the defect is not missed (at least one third of the smallest defect size is suggested). The speed of the scans is mentioned here in order to stress that while array measurements will cover the same area in less time than the coil pair probe, the time taken to cover the areas presented in this thesis are still very long, and in line with the transfer of research technology to industry, the incorporation of the work done into practical techniques should be the first order of focus for future work.

The first stage of future work should be rectifying the compatibility issues of the EmbedEC with multiplexers, and using it to drive an array probe. The EmbedEC has been shown to accurately measure both magnitude, and phase at this frequency, hence array probe C-scans will only require the stitching of the images to create an even wider scan in less time.

The probes used in these experiments were not weighted, or spring loaded onto the test sample to prevent scraping. This caused variations in the flatness of the test sample to to appear more pronounced in form of lift-off trends as shown in the C-scan data. A probe mount can be designed to be spring loaded onto the test sample, with less friction so it does not scrape along the test sample surface.

The experiments presented in this thesis were with the defects oriented parallel to the axis of separation of the coils. Analysis of defects in other orientations should be done to study their effects on the measured coil data.

The raw data from the probes have been presented, however flaw reconstruction using the high SNR data will be the next stage of data processing enabling better visualisation, and understanding for NDT technicians. A limiting factor in measuring phase data using an oscilloscope is the resolution of time jitter, and while the phase measurements were accurate with the EmbedEC, tests were not performed at frequencies higher than 300 kHz as the EmbedEC is limited to a 460 kHz excitation frequency. The work done has shown transmit-receive mode measurements to be much more sensitive, and less prone to errors due to lift-off variation when compared to absolute mode measurements. Hence if only a single choice is available, the probe should be driven in transmit-receive mode, however the maximum utility will be achieved if the probe is multiplexed in both modes.

The next step for future work would be to design array probes capable of taking high frequency measurements. If the resulting effective inductance decrease

in coils designed for high frequency measurements is mitigated, a high frequency array probe with the data processed as presented in this thesis might offer even better sensitivity, and defect detection reliability.

Bibliography

[1] M. G. Silk, A. M. Stoneham, and J. A. G. Temple, *The reliability of non-destructive inspection: assessing the assessment of structures under stress*. Bristol: Hilger, 1987.

[2] U. A. F. NTSB, "232 McDonnell Douglas DC-10-10 Sioux Gateway Airport," *Sioux City, Iowa. July*, vol. 19, 1989.

[3] A. Airlines, "Flight 243, Boeing 737-200, N73711, near Maui Hawaii, April 28, 1988," tech. rep., NSTB/AAR-89/03, National Transportation Safety Board, Washington, DC 20594, 1989.

[4] B. KACZOR, "2 Killed as Engine Parts Pierce Cabin of Delta Jet," *Los Angeles Times*, July 1996.

[5] H. Ranter, "ASN Aircraft accident de Havilland DH-114 Heron N82d Santa Cruz-Viru Viru International Airport (VVI)."

[6] L. Cartz, *Nondestructive Testing: Radiography, Ultrasonics, Liquid Penetrant, Magnetic Particle, Eddy Current*. Materials Park, OH: ASM International, Sept. 1995.

[7] R. A. Adamesku, L. P. Andreeva, P. V. Gel'd, E. A. Mityushov, and N. D. Reimer, "Anisotropy of elastic properties of titanium base alpha-alloys," *Strength of Materials*, vol. 14, no. 9, pp. 1284–1287, 1982.

[8] F. C. Schoenig Jr, J. A. Soules, H. Chang, and J. J. DiCillo, "Eddy current measurement of residual stresses induced by shot peening in titanium Ti-6al-4v," *Materials Evaluation;(United States)*, vol. 53, no. 1, 1995.

[9] A. P. Mouritz, *Introduction to aerospace materials*. Elsevier, 2012.

[10] G. Welsch, R. Boyer, and E. W. Collings, *Materials properties handbook: titanium alloys*. ASM international, 1993.

[11] D. E. Bray and D. McBride, eds., *Nondestructive testing techniques*. New dimensions in engineering, New York ; Chichester: Wiley, 1992.

[12] R. Halmshaw, "Non-destructive testing.," *Edward Arnold, Mill Rd, Dunton Green, Sevenoaks, Kent TN 13 2 YA, UK, 1991. 323*, 1991.

[13] Y. Y. Hung and H. P. Ho, "Shearography: An optical measurement technique and applications," *Materials Science and Engineering: R: Reports*, vol. 49, pp. 61–87, Apr. 2005.

[14] Y. Y. Hung, "Shearography: A New Optical Method For Strain Measurement And Nondestructive Testing," *Optical Engineering*, vol. 21, p. 213391, June 1982.

[15] K. F. Bainton, "Characterizing defects by determining magnetic leakage fields," *NDT International*, vol. 10, no. 5, pp. 253–257, 1977.

[16] U. Ewert, U. Zscherpel, K. Heyne, M. Jechow, and K. Bavendiek, "Image Quality in Digital Industrial Radiography," *Materials Evaluation*, vol. 70, Aug. 2012.

[17] J. Krautkrämer and H. Krautkrämer, *Ultrasonic Testing of Materials*. Springer Science & Business Media, Apr. 2013. Google-Books-ID: GwDvCAAAQBAJ.

[18] B. W. Drinkwater and P. D. Wilcox, "Ultrasonic arrays for non-destructive evaluation: A review," *Ndt & E International*, vol. 39, no. 7, pp. 525–541, 2006.

[19] J. Blitz and G. Simpson, *Ultrasonic Methods of Non-destructive Testing*. Springer Science & Business Media, 1996.

[20] M. Hirao and H. Ogi, *EMATs for science and industry: noncontacting ultrasonic measurements*. Springer Science & Business Media, 2013.

[21] L. C. Lynnworth, *Ultrasonic Measurements for Process Control: Theory, Techniques, Applications*. Academic Press, 1989.

[22] X. Jian, S. Dixon, K. T. V. Grattan, and R. S. Edwards, "A model for pulsed Rayleigh wave and optimal EMAT design," *Sensors and Actuators A: Physical*, vol. 128, no. 2, pp. 296–304, 2006.

[23] P. Shull, *Nondestructive Evaluation: Theory, Techniques, and Applications*, vol. 142 of *Dekker Mechanical Engineering*. CRC Press, May 2002.

[24] C. B. Scruby and L. E. Drain, *Laser Ultrasonics Techniques and Applications*. CRC Press, Jan. 1990.

[25] J.-P. Monchalin, "Progress Towards the Application of Laser-Ultrasonics in Industry," in *Review of Progress in Quantitative Nondestructive Evaluation: Volumes 12A and 12B* (D. O. Thompson and D. E. Chimenti, eds.), pp. 495–506, Boston, MA: Springer US, 1993.

[26] T. Kundu, *Ultrasonic and Electromagnetic NDE for Structure and Material Characterization: Engineering and Biomedical Applications*. CRC Press, June 2012.

[27] G. M. Free, *Eddy-Current Characterization of Materials and Structures*. ASTM International, 1981. Google-Books-ID: Xm7QUkm_E9QC.

[28] G. Y. Tian and A. Sophian, "Reduction of lift-off effects for pulsed eddy current NDT," *NDT & E International*, vol. 38, pp. 319–324, June 2005.

[29] Y. Le Bihan, "Lift-off and tilt effects on eddy current sensor measurements: a 3-D finite element study," *The European Physical Journal-Applied Physics*, vol. 17, no. 1, pp. 25–28, 2002.

[30] S. Giguère, B. A. Lepine, and J. M. S. Dubois, "Pulsed Eddy Current Technology: Characterizing Material Loss with Gap and Lift-off Variations," *Research in Nondestructive Evaluation*, vol. 13, pp. 119–129, Sept. 2001.

[31] R. Grimberg, A. Savin, E. Radu, and O. Mihalache, "Nondestructive evaluation of the severity of discontinuities in flat conductive materials by an eddy-current transducer with orthogonal coils," *IEEE Transactions on Magnetics*, vol. 36, pp. 299–307, Jan. 2000.

[32] J. García-Martín, J. Gómez-Gil, and E. Vázquez-Sánchez, "Non-Destructive Techniques Based on Eddy Current Testing," vol. 11, pp. 2525–2565, Feb. 2011.

[33] N. Ida, *Engineering electromagnetics*. New York: Springer, 2014.

[34] I. S. Grant and W. R. Phillips, *Electromagnetism*. John Wiley & Sons, June 2013.

[35] D. J. Griffiths, *Introduction to electrodynamics*. Pearson custom library, Harlow, Essex, England: Pearson, fourth edition ed., 2014. OCLC: 858091229.

[36] J. F. White, *High Frequency Techniques: An Introduction to RF and Microwave Design and Computer Simulation*. John Wiley & Sons, Jan. 2004.

[37] J. D. Jackson, *Classical electrodynamics*. New York ; London (etc.): Wiley, 2nd ed ed., 1975.

[38] P. A. Rizzi, *Microwave engineering: passive circuits*. Prentice Hall, 1988.

[39] H. Wheeler, "Formulas for the Skin Effect," vol. 30, pp. 412–424, Sept. 1942.

[40] S. Profile, H.-y. Wei, and A. J. Wilkinson, *Design of a Sensor Coil and Measurement Electronics for Magnetic Induction Tomography*.

[41] B. I. Bleaney, B. I. Bleaney, and B. Bleaney, *Electricity and Magnetism, Volume 2*, vol. 2. Oxford University Press, 2013.

[42] C. Owston, "A high frequency eddy-current, non-destructive testing apparatus with automatic probe positioning suitable for scanning applications," *Journal of Physics E: Scientific Instruments*, vol. 3, no. 10, pp. 814–818, 1970.

[43] R. Hughes, Y. Fan, and S. Dixon, "Near electrical resonance signal enhancement (NERSE) in eddy-current crack detection," *NDT & E International*, vol. 66, pp. 82–89, Sept. 2014.

[44] D. Vyroubal, "Impedance of the eddy-current displacement probe: the transformer model," *IEEE Transactions on Instrumentation and Measurement*, vol. 53, pp. 384–391, Apr. 2004.

[45] D. M. Pozar, *Microwave engineering*. John Wiley & Sons, 2009.

[46] R. Bartiromo and M. D. Vincenzi, "The Transmission Line," in *Electrical Measurements in the Laboratory Practice*, Undergraduate Lecture Notes in Physics, pp. 231–250, Springer, Cham, 2016.

[47] W. E. Gardner, ed., *Improving the effectiveness and reliability of non- destructive testing*. International series on materials evaluation and non- destructive testing, Oxford: Pergamon Press, 1992.

[48] T. Theodoulidis, "Analytical model for tilted coils in eddy-current nondestructive inspection," *IEEE Transactions on Magnetics*, vol. 41, pp. 2447–2454, Sept. 2005.

[49] D. H. Hur, M. S. Choi, H.-S. Shim, D. H. Lee, and O. Yoo, "INFLUENCE OF SIGNAL-TO-NOISE RATIO ON EDDY CURRENT SIGNALS OF CRACKS IN STEAM GENERATOR TUBES," *Nuclear Engineering and Technology*, vol. 46, pp. 883–888, Dec. 2014.

[50] S. W. Ra, K. H. Im, S. G. Lee, H. J. Kim, S. J. Song, S. K. Kim, Y. T. Cho, Y. D. Woo, and J. A. Jung, "Simulation and design of ECT differential bobbin probes for the inspection of cracks in bolts," *IOP Conference Series: Materials Science and Engineering*, vol. 103, no. 1, p. 012040, 2015.

[51] J. Blitz, *Electrical and Magnetic Methods of Non-destructive Testing*. Springer Science & Business Media, Nov. 1997.

[52] R. Grimberg, L. Udpa, A. Savin, R. Steigmann, V. Palihovici, and S. S. Udpa, "2d Eddy current sensor array," vol. 39, pp. 264–271, June 2006.

[53] T. P. Theodoulidis and E. E. Kriezis, "Impedance evaluation of rectangular coils for eddy current testing of planar media," *NDT & E International*, vol. 35, pp. 407–414, Sept. 2002.

[54] J. O. Fava, L. Lanzani, and M. C. Ruch, "Multilayer planar rectangular coils for eddy current testing: Design considerations," *NDT & E International*, vol. 42, pp. 713–720, Dec. 2009.

[55] R. J. Ditchburn and S. K. Burke, "Planar rectangular spiral coils in eddy-current non-destructive inspection," *NDT & E International*, vol. 38, pp. 690–700, Dec. 2005.

[56] X. Jian and S. Dixon, "Enhancement of EMAT and eddy current using a ferrite back-plate," *Sensors and Actuators A: Physical*, vol. 136, pp. 132–136, May 2007.

[57] H.-Y. Mun and C.-E. Kim, "Comparison of ECT Probes in Diagnosis of Defects," *Journal of Electrical Engineering and Technology*, vol. 9, no. 1, pp. 190–196, 2014.

[58] H. Huang, N. Sakurai, T. Takagi, and T. Uchimoto, "Design of an eddy-current array probe for crack sizing in steam generator tubes," *NDT & E International*, vol. 36, pp. 515–522, Oct. 2003.

[59] F. Hughes, R. Day, N. Tung, and S. Dixon, "High-frequency eddy current measurements using sensor-mounted electronics," Nov. 2016.

[60] G. Mook, F. Michel, and J. Simonin, "Electromagnetic Imaging Using Probe Arrays," *Strojniški vestnik – Journal of Mechanical Engineering*, vol. 2011, pp. 227–236, Mar. 2011.

[61] V. Zilberstein, D. Grundy, V. Weiss, N. Goldfine, E. Abramovici, J. Newman, and T. Yentzer, "Early detection and monitoring of fatigue in high strength steels with MWM-Arrays," *International Journal of Fatigue*, vol. 27, pp. 1644–1652, Oct. 2005.

[62] X. Chen and T. Ding, "Flexible eddy current sensor array for proximity sensing," *Sensors and Actuators A: Physical*, vol. 135, pp. 126–130, Mar. 2007.

[63] T. Chen, Y. He, and J. Du, "A High-Sensitivity Flexible Eddy Current Array Sensor for Crack Monitoring of Welded Structures under Varying Environment," *Sensors*, vol. 18, p. 1780, June 2018. WOS:000436774300114.

[64] M. A. Machado, L. Rosado, N. Pedrosa, A. Vostner, R. M. Miranda, M. Piedade, and T. G. Santos, "Novel eddy current probes for pipes: Application in austenitic round-in-square profiles of ITER," *NDT & E International*, vol. 87, pp. 111–118, Apr. 2017.

[65] C. Gilles-pascaud, B. Lorecki, and M. Pierantoni, *Eddy Current Array Probe Development for Nondestructive Testing.*

[66] T. Dogaru and S. T. Smith, "Giant magnetoresistance-based eddy-current sensor," *IEEE Transactions on Magnetics*, vol. 37, pp. 3831–3838, Sept. 2001.

[67] P. Ripka, M. Tondra, J. Stokes, and R. Beech, "AC-driven AMR and GMR magnetoresistors," *Sensors and Actuators A: Physical*, vol. 76, pp. 225–230, Aug. 1999.

[68] N. Novkovski, "Progress and limitations in magnetic field measurements," in *Geomagnetics for Aeronautical Safety*, pp. 201–212, Springer, 2006.

[69] K. Chomsuwan, T. Somsak, C. P. Gooneratne, and S. Yamada, "High-Spatial Resolution Giant Magnetoresistive Sensors-Part I: Application in Non-Destructive Evaluation," in *Giant Magnetoresistance (GMR) Sensors*, pp. 211–241, Springer, 2013.

[70] C. H. Smith, "GMR Magnetic Sensor Arrays for NDE Eddy-Current Testing," in *AIP Conference Proceedings*, vol. 657, (Bellingham, Washington (USA)), pp. 419–426, AIP, 2003.

[71] M. Pelkner, R. Stegemann, N. Sonntag, R. Pohl, and M. Kreutzbruck, "Benefits of GMR sensors for high spatial resolution NDT applications," (Provo, Utah, USA), p. 040001, 2018.

[72] Y. He, M. Pan, F. Luo, and G. Tian, "Pulsed eddy current imaging and frequency spectrum analysis for hidden defect nondestructive testing and evaluation," *NDT & E International*, vol. 44, pp. 344–352, July 2011.

[73] J. Paasi, T. Kalliohaka, A. Korpela, L. Soderlund, P. F. Hermann, J. Kvitkovic, and M. Majoros, "Homogeneity studies of multifilamentary BSCCO tapes by three-axis Hall sensor magnetometry," *IEEE Transactions on Applied Superconductivity*, vol. 9, pp. 1598–1601, June 1999.

[74] M. Fan, B. Cao, A. I. Sunny, W. Li, G. Tian, and B. Ye, "Pulsed eddy current thickness measurement using phase features immune to liftoff effect," *NDT & E International*, vol. 86, pp. 123–131, Mar. 2017.

[75] J. R. Hook and H. E. Hall, *Solid State Physics*. New York, UNITED KINGDOM: John Wiley & Sons, Incorporated, 2013.

[76] M. Muck, M. Korn, C. Welzel, S. Grawunder, and F. Scholz, "Nondestructive evaluation of various materials using a SQUID-based eddy-current system," *IEEE Transactions on Applied Superconductivity*, vol. 15, pp. 733–736, June 2005.

[77] H.-J. Krause and G. Donaldson, "Nondestructive Evaluation of Materials and Structures using SQUIDs," in *The SQUID Handbook*, pp. 441–479, Wiley-Blackwell, Dec. 2006.

[78] K. Allweins, G. Gierelt, H. Krause, and M. Kreutzbruck, "Defect detection in thick aircraft samples based on HTS SQUID-magnetometry and pattern recognition," *IEEE Transactions on Applied Superconductivity*, vol. 13, pp. 250–253, June 2003.

[79] A. Tsukamoto, T. Hato, S. Adachi, Y. Oshikubo, K. Tsukada, and K. Tanabe, "Development of Eddy Current Testing System Using HTS-SQUID on a Hand Cart for Detection of Fatigue Cracks of Steel Plate Used in Expressways," *IEEE Transactions on Applied Superconductivity*, vol. 28, pp. 1–5, June 2018.

[80] R. S. Sharpe, "Research techniques in nondestructive testing. Volume III," 1977.

[81] Z. Liu, K. Tsukada, K. Hanasaki, and M. Kurisu, "Two-Dimensional Eddy Current Signal Enhancement via Multifrequency Data Fusion," *Research in Nondestructive Evaluation*, vol. 11, pp. 165–177, Jan. 1999.

[82] K. A. Bartels and J. L. Fisher, "Multifrequency eddy current image processing techniques for nondestructive evaluation," in *Proceedings., International Conference on Image Processing*, vol. 1, pp. 486–489 vol.1, Oct. 1995.

[83] Z. Q. Lang, A. Agurto, G. Y. Tian, and A. Sophian, "A system identification based approach for pulsed eddy current non-destructive evaluation," *Measurement Science and Technology*, vol. 18, no. 7, p. 2083, 2007.

[84] V. Arjun, B. Sasi, B. P. C. Rao, C. K. Mukhopadhyay, and T. Jayakumar, "Optimisation of pulsed eddy current probe for detection of sub-surface defects in stainless steel plates," *Sensors and Actuators A: Physical*, vol. 226, pp. 69–75, May 2015.

[85] B. Yang, Y. Zhao, and W. Zhang, "Quantification of crack defect using a new pulsed eddy current probe," *Nondestructive Testing and Evaluation*, vol. 26, pp. 155–168, June 2011.

[86] G. Y. Tian, Y. Li, and C. Mandache, "Study of Lift-Off Invariance for Pulsed Eddy-Current Signals," *IEEE Transactions on Magnetics*, vol. 45, pp. 184–191, Jan. 2009.

[87] A. Sophian, G. Y. Tian, D. Taylor, and J. Rudlin, "Design of a pulsed eddy current sensor for detection of defects in aircraft lap-joints," *Sensors and Actuators A Physical*, vol. 101, pp. 92–98, 2002.

[88] K. Sambasiva Rao, S. Mahadevan, B. Purna Chandra Rao, and S. Thirunavukkarasu, "A new approach to increase the subsurface flaw detection capability of pulsed eddy current technique," *Measurement*, vol. 128, pp. 516–526, Nov. 2018.

[89] R. R. Boyer, "An overview on the use of titanium in the aerospace industry," *Materials Science and Engineering: A*, vol. 213, pp. 103–114, Aug. 1996.

[90] J. T. Milck, "Electrical Resistivity Data and Bibliography on Titanium and Titanium Alloys:," tech. rep., Defense Technical Information Center, Fort Belvoir, VA, Mar. 1970.

[91] Y. Ho and T. K. Chu, "Electrical Resistivity and Thermal Conductivity of Nine Selected AISI stainless Steels," p. 53.

[92] I. Egry, R. Brooks, D. Holland-Moritz, R. Novakovic, T. Matsushita, E. Ricci, S. Seetharaman, R. Wunderlich, and D. Jarvis, "Thermophysical Properties of gamma-Titanium Aluminide: The European IMPRESS Project," *International Journal of Thermophysics*, vol. 28, pp. 1026–1036, Sept. 2007.

[93] F. Appel, J. D. H. Paul, and M. Oehring, *Gamma titanium aluminide alloys: science and technology*. John Wiley & Sons, 2011.

[94] J. Anudev and I. J. Raglend, "Analytical study of howland current source model," in *2012 International Conference on Computing, Electronics and Electrical Technologies (ICCEET)*, pp. 314–318, Mar. 2012.

[95] Fairrite, "67 Material Data Sheet," Mar. 2018.

[96] "Sum of Sines Models - MATLAB & Simulink - MathWorks United Kingdom."

[97] M. Frigo and S. Johnson, "FFTW: an adaptive software architecture for the FFT," vol. 3, pp. 1381–1384, IEEE, 1998.

[98] A. J. McCann, A. Workman, and C. McGrath, "A quick and robust method for measurement of signal-to-noise ratio in MRI," *Physics in Medicine and Biology*, vol. 58, pp. 3775–3790, June 2013.

[99] E. J. Breen and R. Jones, "Attribute Openings, Thinnings, and Granulometries," *Computer Vision and Image Understanding*, vol. 64, pp. 377–389, Nov. 1996.

[100] D. G. Lowe, "Object recognition from local scale-invariant features," in *Proceedings of the Seventh IEEE International Conference on Computer Vision*, vol. 2, pp. 1150–1157 vol.2, Sept. 1999.

[101] P. Soille, *Morphological Image Analysis: Principles and Applications*. Berlin Heidelberg: Springer-Verlag, 2 ed., 2004.

[102] O. Yli-Harja, J. Astola, and Y. Neuvo, "Analysis of the properties of median and weighted median filters using threshold logic and stack filter representation," *IEEE Transactions on Signal Processing*, vol. 39, pp. 395–410, Feb. 1991.

[103] Z. Wang and D. Zhang, "Progressive switching median filter for the removal of impulse noise from highly corrupted images," *IEEE Transactions on Circuits and Systems II: Analog and Digital Signal Processing*, vol. 46, pp. 78–80, Jan. 1999.

[104] S. Ko and Y. H. Lee, "Center weighted median filters and their applications to image enhancement," *IEEE Transactions on Circuits and Systems*, vol. 38, pp. 984–993, Sept. 1991.

[105] B. Münch, P. Trtik, F. Marone, and M. Stampanoni, "Stripe and ring artifact removal with combined wavelet — Fourier filtering," *Optics Express*, vol. 17, pp. 8567–8591, May 2009.

[106] D. Wilken, P. Feldens, T. Wunderlich, and C. Heinrich, "Application of 2d Fourier filtering for elimination of stripe noise in side-scan sonar mosaics," *Geo-Marine Letters*, vol. 32, pp. 337–347, Aug. 2012.

[107] J.-S. Lee, "Digital image smoothing and the sigma filter," *Computer vision, graphics, and image processing*, vol. 24, no. 2, pp. 255–269, 1983.

[108] Y. Zhuang, L. Chen, X. S. Wang, and J. Lian, "A Weighted Moving Average-based Approach for Cleaning Sensor Data," in *27th International Conference on Distributed Computing Systems (ICDCS '07)*, pp. 38–38, June 2007.

[109] I. T. Young and L. J. Van Vliet, "Recursive implementation of the Gaussian filter," *Signal processing*, vol. 44, no. 2, pp. 139–151, 1995.

[110] G. Deng and L. W. Cahill, "An adaptive Gaussian filter for noise reduction and edge detection," in *1993 IEEE Conference Record Nuclear Science Symposium and Medical Imaging Conference*, pp. 1615–1619 vol.3, Oct. 1993.

[111] Y. Le Diraison, P.-Y. Joubert, and D. Placko, "Characterization of subsurface defects in aeronautical riveted lap-joints using multi-frequency eddy current imaging," *NDT & E International*, vol. 42, pp. 133–140, Mar. 2009.

[112] L. Shu, H. Songling, Z. Wei, and Y. Peng, "Study of pulse eddy current probes detecting cracks extending in all directions," *Sensors and Actuators A: Physical*, vol. 141, pp. 13–19, Jan. 2008.

[113] P. Y. Joubert, E. Vourc'h, and V. Thomas, "Experimental validation of an eddy current probe dedicated to the multi-frequency imaging of bore holes," *Sensors and Actuators A: Physical*, vol. 185, pp. 132–138, Oct. 2012.

[114] L. T. Cung, T. D. Dao, P. C. Nguyen, and T. D. Bui, "A model-based approach for estimation of the crack depth on a massive metal structure," *Measurement and Control*, vol. 51, pp. 182–191, June 2018.

[115] J. Cheng, J. Qiu, H. Ji, E. Wang, T. Takagi, and T. Uchimoto, "Application of low frequency ECT method in noncontact detection and visualization of CFRP material," *Composites Part B: Engineering*, vol. 110, pp. 141–152, Feb. 2017.

[116] A. Rosell and G. Persson, "Modelling of a Differential Sensor in Eddy Current Non- Destructive Evaluation," *Proceedings of the 2011 COMSOL Conference in Stuttgart*, p. 7, Aug. 2011.

[117] M. R. Rawashdeh, A. Rosell, L. Udpa, S. R. H. Hoole, and Y. Deng, "Optimized Solutions for Defect Characterization in 2-D Inverse Eddy Current Testing Problems Using Subregion Finite Element Method," *IEEE Transactions on Magnetics*, vol. 54, pp. 1–15, Aug. 2018.

[118] L. Le Gratiet, B. Iooss, G. Blatman, T. Browne, S. Cordeiro, and B. Goursaud, "Model Assisted Probability of Detection Curves: New Statistical Tools and Progressive Methodology," *Journal of Nondestructive Evaluation*, vol. 36, p. 8, Dec. 2016.

[119] S. Singh, D. Greving, A. Kinney, F. Vensel, J. Ohm, and M. Peeler, "Eddy current measurement system evaluation for corrosion depth determination on cast aluminum aircraft structure," *AIP Conference Proceedings*, vol. 1511, pp. 1278–1285, Jan. 2013.

[120] A. Brown and C. Eviston, "Model Development and Validation of Geometrically Complex Eddy Current Coils Using Finite Element Methods," in *43rd Review of Progress in Quantitative Nondestructive Evaluation*, vol. 1806, pp. UNSP 110015–1, Melville: Amer Inst Physics, 2017. WOS:000403042900152.

[121] Z. Su, A. Efremov, M. Safdarnejad, A. Tamburrino, L. Udpa, and S. S. Udpa, "Optimization of coil design for near uniform interrogating field generation," *AIP Conference Proceedings*, vol. 1650, pp. 405–413, Mar. 2015.

[122] C. V. Dodd and W. E. Deeds, "Analytical Solutions to Eddy-Current Probe-Coil Problems," *Journal of Applied Physics*, vol. 39, pp. 2829–2838, May 1968.

[123] B. A. Auld and J. C. Moulder, "Review of Advances in Quantitative Eddy Current Nondestructive Evaluation," *Journal of Nondestructive Evaluation*, vol. 18, pp. 3–36, Mar. 1999.

[124] S. K. Burke and M. E. Ibrahim, "Mutual impedance of air-cored coils above a conducting plate," *J. Phys. D: Appl. Phys.*, vol. 37, no. 13, p. 1857, 2004.

[125] T. Rylander, P. Ingelström, and A. Bondeson, "Computational Electromagnetics," in *Computational Electromagnetics*, Texts in Applied Mathematics, pp. 11–18, Springer, New York, NY, 2013.

[126] J. R. Cardoso, *Electromagnetics through the Finite Element Method : A Simplified Approach Using Maxwell's Equations*. CRC Press, Oct. 2016.

[127] C. Lacombe and C. Bédard, "Interpolation function of a general triangular mid-edge finite element," *Computers & Mathematics with Applications*, vol. 12, pp. 363–373, Mar. 1986.

[128] O. Biro and K. Preis, "On the use of the magnetic vector potential in the finite-element analysis of three-dimensional eddy currents," *IEEE Transactions on Magnetics*, vol. 25, pp. 3145–3159, July 1989.

[129] N. Ida and J. P. A. Bastos, *Electromagnetics and Calculation of Fields*. New York: Springer-Verlag, 2 ed., 1997.

[130] A. Chama, S. Gerber, and R. Wang, "Newton–Raphson Solver for Finite Element Methods Featuring Nonlinear Hysteresis Models," *IEEE Transactions on Magnetics*, vol. 54, pp. 1–8, Jan. 2018.

[131] Y. Choua, L. Santandrea, Y. L. Bihan, and C. Marchand, "Mesh Refinement in Eddy Current Testing With Separated T-R Probes," *IEEE Transactions on Magnetics*, vol. 46, pp. 2795–2798, Aug. 2010.

[132] P. J. Arrazola, A. Garay, L. M. Iriarte, M. Armendia, S. Marya, and F. Le Maître, "Machinability of titanium alloys (Ti6al4v and Ti555.3)," *Journal of Materials Processing Technology*, vol. 209, pp. 2223–2230, Mar. 2009.

[133] H. J. Rack and J. I. Qazi, "Titanium alloys for biomedical applications," *Materials Science and Engineering: C*, vol. 26, pp. 1269–1277, Sept. 2006.

[134] J. Sharan, S. Lale, V. Koul, M. Mishra, and D. Kharbanda, "An overview of surface modifications of titanium and its alloys for biomedical applications," *Trends in Biomaterials and Artificial Organs*, vol. 29, pp. 176–187, Jan. 2015.

[135] W. S. Yip and S. To, "Ductile and brittle transition behavior of titanium alloys in ultra-precision machining," *Scientific Reports*, vol. 8, p. 3934, Mar. 2018.

[136] F. Franco, F. A. Cardoso, L. S. Rosado, R. Ferreira, S. Cardoso, M. Piedade, and P. P. Freitas, "Advanced NDT Inspection Tools for Titanium Surfaces

Based on High-Performance Magnetoresistive Sensors," *IEEE Transactions on Magnetics*, vol. 53, pp. 1–5, Apr. 2017.

[137] R. A. Wincheski, "Procedure for Automated Eddy Current Crack Detection in Thin Titanium Plates," p. 15, 2012.

[138] R. T. Ko and S. J. Pipenberg, "Automated Eddy Current Detection of Flaws in Shot-Peened Titanium Materials," in *Review of Progress in Quantitative Nondestructive Evaluation* (D. O. Thompson and D. E. Chimenti, eds.), pp. 755–761, Boston, MA: Springer US, 1995.

[139] C. N. Owston, "Eddy-current testing at microwave frequencies," *Non-Destructive Testing*, vol. 2, pp. 193–196, Aug. 1969.

[140] L. Solymar, D. Walsh, and R. R. A. Syms, *Electrical Properties of Materials*. Oxford: Oxford University Press, 9 edition ed., May 2014.

[141] L.-K. Wu, W.-Y. Wu, J.-L. Song, G.-Y. Hou, H.-Z. Cao, Y.-P. Tang, and G.-Q. Zheng, "Enhanced high temperature oxidation resistance for gamma-TiAl alloy with electrodeposited SiO2 film," *Corrosion Science*, vol. 140, pp. 388–401, Aug. 2018.

[142] E. Rau, J. Bamberg, J. Burchards, P. Berwig, and W. Voelkl, "High resolution crack detection on turbine blade roots by the use of eddy current and ultrasonic Rayleigh waves," p. 8.

[143] Y.-W. Kim, W. Smarsly, J. Lin, D. Dimiduk, and F. Appel, *Gamma Titanium Aluminide Alloys 2014*. New York, UNITED STATES: John Wiley & Sons, Incorporated, 2014.

[144] G. Hénaff and A.-L. Gloanec, "Fatigue properties of TiAl alloys," *Intermetallics*, vol. 13, no. 5, pp. 543–558, 2005.

[145] "Analog Devices Inc. ADG1607 Series Multiplexer Switch ICs | Mouser United Kingdom."